Thermal and Melt Wear Characterization of Materials in Sliding Contact at High Speed

THESIS

Christopher J. Alban, Captain, USAF

AFIT-ENY-14-M-04

DEPARTMENT OF THE AIR FORCE

AIR UNIVERSITY

AIR FORCE INSTITUTE OF TECHNOLOGY

Wright-Patterson Air Force Base, Ohio

AFIT-ENY-14-M-04

Thermal and Melt Wear Characterization of Materials in Sliding Contact at High Speed

THESIS

Presented to the Faculty
Department of Aeronautics and Astronautics
Graduate School of Engineering and Management
Air Force Institute of Technology
Air University
Air Education and Training Command
In Partial Fulfillment of the
Requirements for the Degree of
Master of Science in Aeronautical Engineering

Christopher J. Alban, BS
Captain, USAF

March 2014

AFIT-ENY-14-M-04

THERMAL AND MELT WEAR CHARACTERIZATION OF MATERIALS IN SLIDING CONTACT AT HIGH SPEED

Christopher J. Alban, BS
Captain, USAF

Approved:

//signed//	3 Mar 2014
Anthony N. Palazotto, PhD (Chair)	Date
//signed//	3 Mar 2014
William P. Baker, PhD (Member)	Date
//signed//	3 Mar 2014
Maj James L. Rutledge (Member)	Date

AFIT-ENY-14-M-04

Abstract

The Holloman High Speed Test Track is used to evaluate hypersonic aircraft materiel in a near-operational environment. The four-stage pusher rocket sled is capable of accelerating a test apparatus to hypersonic speeds in a matter of seconds. The sled must contend with tremendous thermal, mechanical, and aerodynamic loading during each run.

The effects of the combination of forces acting on the sled are most acute at the interface between the rail and the wraparound slipper that holds the sled to the rail. Frictional heating due to sliding contact between the slipper and the rail coupled with mechanical wear can lead to significant material degradation in the slipper. Aerodynamic heating can exacerbate deleterious wear effects.

This work considers the application of thermal and aerodynamic loading on the slipper. Two computational models are employed to depict temperature distribution and estimate melt wear over the course of a test run. The thermal load cases considered in this research allow a new perspective on the slipper wear phenomena and should serve as a building block in future research endeavors.

Acknowledgements

Special thanks to Dr. Anthony Palazotto, without his enthusiasm and his patience this work would not have been possible.

Thanks to Dr. William Baker for helping me to better understand the mathematics involved in characterizing slipper wear and for showing me the finer points of the finite difference code.

Thanks to Major James Rutledge for helping me to comprehend the complexities of air flow dynamics and heat transfer principles as they are applied to this research endeavor.

Contents

List of Figures

List of Tables

Nomenclature

$()_{,i}$	Directional Derivative in the i-direction
$()_1$	Condition in Front of Shock
$()_2$	Condition Behind Shock
$()_\infty$	Freestream Condition
$()_{\text{gap}}$	Condition in Gap Between Slipper and Rail
$()_{\text{liq}}$	Liquid Condition
$()_{\text{perf}}$	Calorically Perfect Gas
$()_{\text{sol}}$	Solid Condition
$()_{\text{s}}$	Condition at a Surface
$()_e$	Condition at Boundary Layer Edge
$()_i$	Component in the i-direction
C_f	Aerodynamic Friction Coefficient
F	Force Between Slipper and Rail (N)
Fr	Frössling Number
H	Slipper Height (m)
L	Slipper Length (m)
M	Mach Number
N	Melt Time Evaluation Term
Nu	Nusslet Number

P	Contact Pressure (N/m^2)
Pr	Prandtl Number
Q	Elemental Source Heat Flux (W/m^2)
R	Specific Gas Constant (J/kg-K)
Re	Reynolds Number
S	Surface of Integration
T	Temperature (K)
T_{T}	Total Temperature (K)
T_{aw}	Adiabatic Wall Temperature (K)
V	Volume of Integration
$[\boldsymbol{B}]$	Finite Element Shape Function Derivative
$[\boldsymbol{C}]$	Global Specific Heat Matrix (J/kg-K)
$[\boldsymbol{S}]$	Elemental Geometry Matrix
$[\boldsymbol{c_p}]$	Elemental Specific Heat Matrix (J/kg-K)
$[\boldsymbol{h}]$	Elemental Convection Coefficient Matrix (W/m^2-K)
$[\boldsymbol{k}]$	Elemental Conductivity Matrix (W/m-K)
$\bar{a}$	Single Finite Element Horizontal Dimension (m)
$\bar{b}$	Single Finite Element Vertical Dimension (m)
$\bar{h}$	Enthalpy (J)
$\bar{u}$	Internal Energy (J)
$\bar{v}$	Specific Volume (kg/m^3)

$\dot{T}$	Temperature, Time Rate of Change (K/s)
$\{\boldsymbol{F}_B\}$	Global Conduction Heat Flux Vector (W/m^2)
$\{\boldsymbol{F}_T\}$	Global Heat Flux Vector, Total (W/m^2)
$\{\boldsymbol{F}_h\}$	Global Boundary Convection Vector (W/m^2)
$\{\boldsymbol{T}_e\}$	Elemental Temperature (T)
$\{\dot{\boldsymbol{T}}_{\boldsymbol{e}}\}$	Elemental Temperature, Time Rate of Change (K/s)
$\{\boldsymbol{f}_B\}$	Elemental Conduction Heat Flux Vector (W/m^2)
$\{\boldsymbol{f}_h\}$	Elemental Boundary Convection Vector (W/m^2)
$\lfloor \boldsymbol{N} \rfloor$	Finite Element Shape Function
a	Speed of Sound (m/s)
a_0	Constant Acceleration (m/s^2)
c_p	Specific Heat at Constant Pressure (J/kg-K)
c_v	Specific Heat at Constant Volume (J/kg-K)
h	Heat Transfer Coefficient (W/m^2-K)
k	Thermal Conductivity (W/m-K)
l	Latent Heat (J/kg)
m	Switch Function
p	Air Pressure (N/m^2)
q	Elemental Internal Heat Flux (W/m^2)
q''	Heat Flux (W/m^2)
r	Melt Time Evaluation Term

s	Entropy (J/K)
t	Time (s)
t_{m}	Time to Slipper Melt (s)
u	Air Speed (m/s)
u_c	Couette Flow Speed (m/s)
v	Sled Velocity (m/s)
v_0	Constant Velocity (m/s)
x	Distance from Slipper Leading Edge (m)
y^*	Diffusivity Depth (m)
Π	Finite Element Functional
α	Heat Flux Partition
α'	Finite Element Formulation Constant
α_0	Heat Flux Partition, Initial
α_{m}	Heat Flux Partition, Melt
$\bar{\alpha}$, $\bar{\beta}$	Finite Element Geometric Ratios
$\bar{\mu}$	Coefficient of Friction
β	Melt Time Evaluation Term
δ	Boundary Layer Thickness (m)
γ	Ratio of Specific Heats
κ	Thermal Diffusivity (m^2/s)
λ	Melt Time Evaluation Term

μ	Dynamic Viscosity (kg/m-s)
ν	Kinematic Viscosity (m^2/s)
ψ	Finite Element Geometric Weighting Function
ρ	Mass Density (kg/m^3)
σ	Melt Depth (m)
τ	Shear Stress (N/m^2)
Θ	Specific Heat Formula Thermal Constant (K)
θ	Sutherland Formula Thermal Constant (K)
ξ, η	Finite Element Coordinates

1 Introduction

1.1 General Issue

The Holloman High Speed Test Track (HHSTT) is used to test materiel, flight instrumentation, and components of hypersonic aircraft in near operational conditions. Flight testing of systems used in hypersonic aircraft is dangerous and expensive. Further, data collection is difficult. The HHSTT environment allows for controlled, repeatable test conditions.

Figure 1: Four Stage Rocket Sled Apparatus. [37]

A four stage pusher rocket train (Fig. 1) quickly accelerates test articles to hypersonic speeds. The test vehicle travels on a 10 mile straight rail track located at Holloman Air Force Base (AFB) in New Mexico. An aerial view of the track is shown in Fig. 2. The train completes traversal of the 10 mile track in a matter of few seconds.

Figure 2: Holloman High Speed Test Track, Aerial View.

During each test run, a tremendous amount of frictional heating is generated due to the steel-on-steel sliding interaction between the rail and slipper.

Figure 3: Sled. [18]

Figure 3 shows an image of the forebody of a rocket sled with rails and slippers indicated. Aerodynamic loads are generated by the high speed motion of the rocket sled. The wraparound slipper restrains the sled from flying off the rails as a result of aerodynamic lifting on the body. Figure 4 shows a representative VascoMax 300 slipper used in an HHSTT test run.

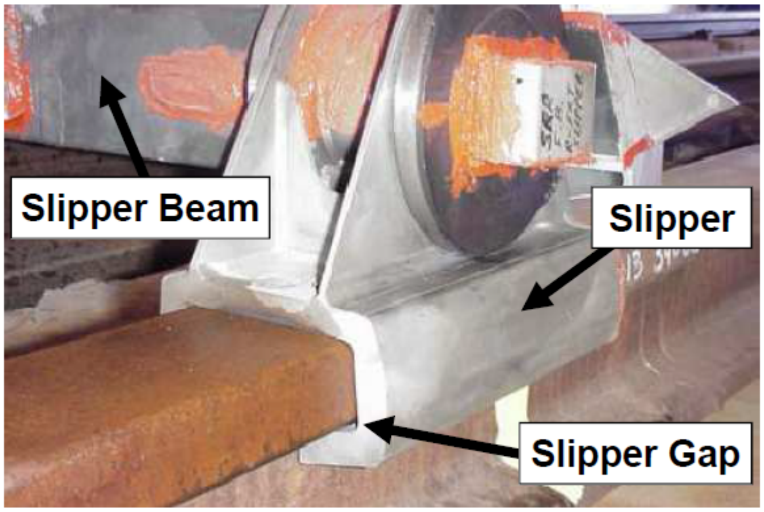

Figure 4: VascoMax 300 Slipper. [18]

The frictional heating resulting from the sliding interaction between the slipper and the rail causes the temperature in the slipper to increase to the point that mechanical wear is encouraged due to softening of the slipper material and may even induce melt. The strength of the heat flux generated is dependent on the speed of the sled, the downward force on the slipper due to the weight of the sled, and the relative roughness of the two steels (1080 steel of the rail and VascoMax 300 of the slipper).

1.2 Problem Statement

During a test run, the slippers wear to a point that makes slipper reuse impossible. Slipper wear may be mechanical or thermal in nature. Wear modes seen in previously examined slippers include mechanical gouging, asperity collision, and melt. In the case of gouging, the slipper digs into the rail and causes material to be removed from either or both materials. Asperity collision describes the case when the slipper collides with a surface imperfection on the rail causing degradation or removal of slipper material. The possibility of either of these wear modes occurring is increased at elevated temperatures.

Inspection of used slippers also indicates melt as a likely failure mode. Frictional heating can raise the temperature in the slipper to the point of melt. When the temperature of the heat slipper reaches the melting point, small amounts of the slipper are removed.

The occurrence of any one of these failure modes does not preclude the occurrence of the others. Unfavorable conditions may lead to compound wear. Enough wear in a slipper can lead to macro scale deterioration of the material and ultimately catastrophic failure.

In addition to frictional heating, aerodynamic loads have considerable effect on the rocket sled apparatus. Pressure loads generated on the underside of the sled will lift the slipper from the contact surface. The wraparound slipper prevents the lifting motion and pulls the sled back down to the rail. For much of a test run, the aerodynamic lifting force is greater than the weight of the sled. The opposing forces induce a bouncing effect as the slipper is repeatedly lifted from, then returned to the rail. Figure 5 is a simplified representation of the motion.

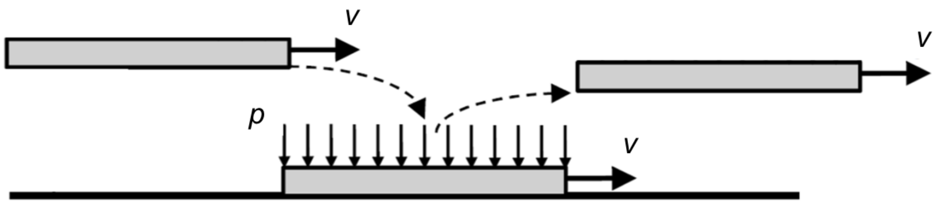

Figure 5: Bounce.

In Fig. 5, P represents the distributed pressure due to the downward dynamic force of the sled acting between the slipper and the rail. The amount of heating seen by the slipper at any time depends on the magnitude of the pressure. The v in Fig. 5 represents velocity and the arrow indicates the direction of slipper travel.

When the slipper surface is lifted from the rail (bouncing), a gap forms between the slipper and the rail (Fig. 6). When the slipper is bouncing, air flows between the slipper and the rail at high speeds. The high speed air flow will have a convective heating effect on the slipper. If the slipper were in constant contact with the rail and did not bounce the only heat flux seen by the bottom surface would be due to frictional heating and would lead to significantly higher slipper temperatures and greater melt wear. The convective effects permitted by the air flow through the gap serve to both heat (when the stagnation temperature of the air is warmer) and cool the slipper (when the stagnation temperature is cooler).

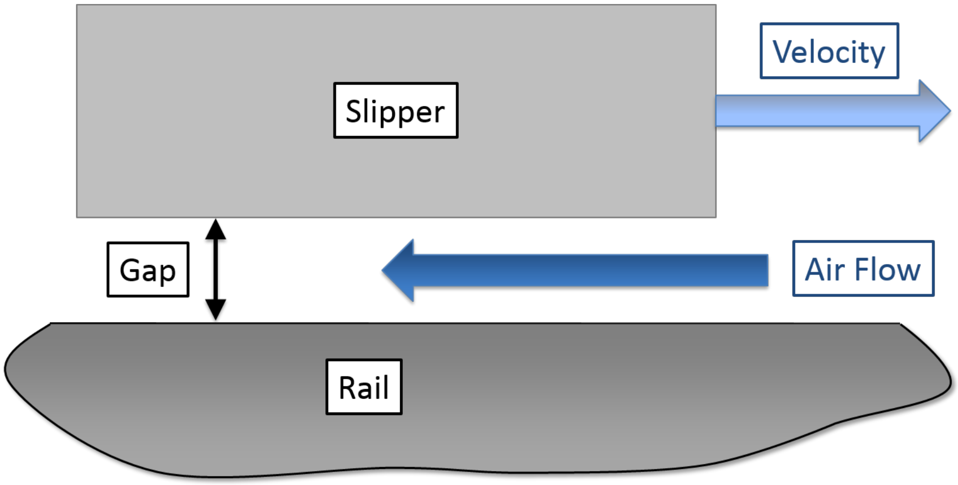

Figure 6: Gap Between Slipper and Rail.

Forced convection resulting from the high speed air flow also occurs on the top and front faces of the slipper. The cumulative effects of conductive frictional and convective aerodynamic heating are seen in the temperature distributions and melt wear estimations presented in Chapter 5.

1.3 Research Objectives

Reduction or elimination of wear is of paramount interest. This research seeks to advance the understanding of the influence of heat loading on the slipper and its influence on melt wear. This study was accomplished through the development of appropriate models to predict two-dimensional temperature distributions in a cross section of the slipper and estimate melt wear due steel-on-steel sliding contact and aerodynamic loading at supersonic velocity.

1.4 Research Focus

Discussed in detail in Chapter 2, the study of wear of materials in sliding contact in general and wear of the HHSTT slipper specifically has been ongoing for some time. The primary focus of most of these studies has been mechanical wear. Some investigations have included melt wear and thermal loading as a secondary influence to overall wear. The current research attempts to explore a new path in characterization of the slipper wear by focusing attention on the development of the thermal profile in the slipper resulting from the heating by conduction and the heating and cooling aerodynamic effects.

Data from the Dynamic Analysis and Design System (DADS) used in the current research was generated prior to a test run conducted in January 2008 to predict dynamic behavior of the rocket sled system during the actual test run.

The left rear slipper from the third stage car (second car from the front of the train in Fig. 7) of the January 2008 test run was provided to AFIT for analysis and has been the subject of past AFIT research projects. Melt wear results generated in the current research are compared to the actual wear seen in the slipper.

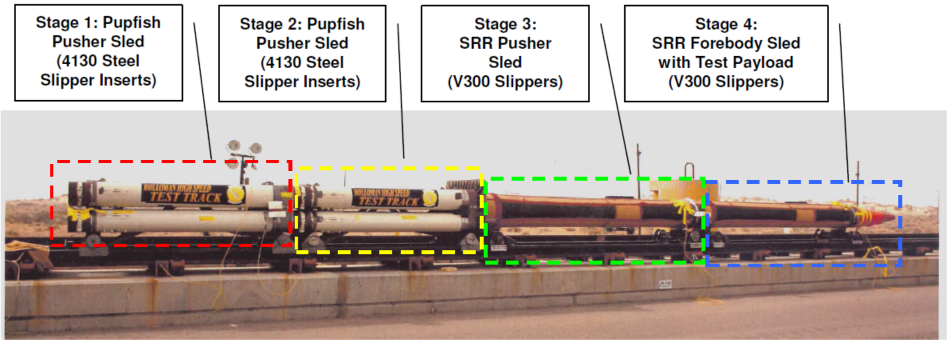

Figure 7: Four Stage Train.

The current research analyzes the DADS data and slipper from the January 2008 test run through application of mathematical models developed to predict melt wear resulting from the high speed slipper / rail interaction. Aerodynamic heating and cooling are also considered.

1.5 Investigative Questions

Although most examinations of the HHSTT slipper wear problem have focused on mechanical wear, a few have considered melt wear of the slipper. Le's [26] research, in particular, focused specifically on characterization of the melt depth into the slipper. Le used a one-dimensional finite difference algorithm to characterize slipper melt. Le applied multiple heat flux partitioning functions to the slipper / rail interface to determine which function best approximated actual melt wear.

The present research seeks to improve upon Le's analysis by refining the one-dimensional finite difference model. Additionally, a two-dimensional finite element model was developed to estimate melt wear.

Specific questions this research will address:

- To what degree does aerodynamic heating and cooling affect the temperature distribution and influence melt?
- How will refining the inputs to the models from simplified assumptions affect the temperature and melt wear results?

1.6 Methodology

Figure 8 shows the modeling process employed in the generation thermal distributions and melt wear estimations. The numbers in parenthesis indicate the corresponding section of this thesis where each topic is discussed.

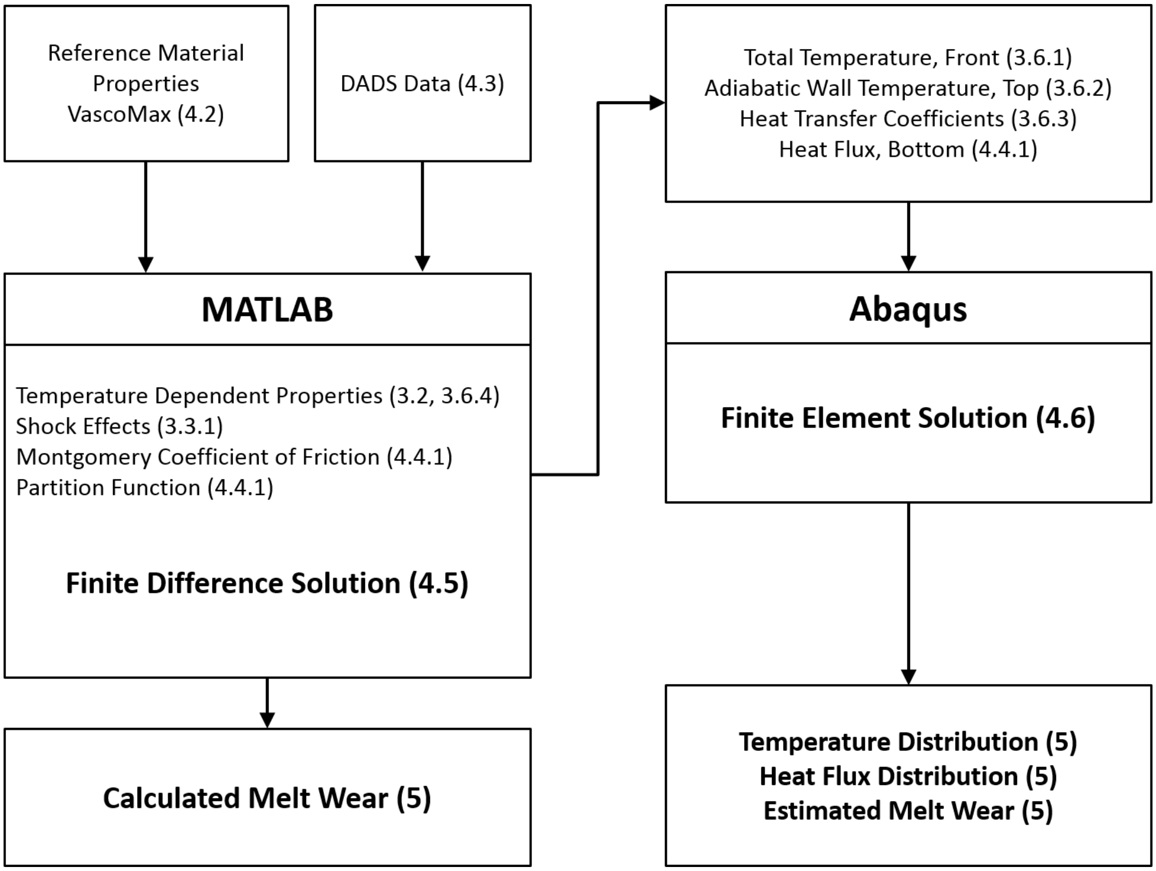

Figure 8: Modeling Process.

The first step in the process is handled in MATLAB. Initial material properties (for air and VascoMax) are assigned and DADS data is read in. The MATLAB code calculates air properties due to temperature variations and shock effects, friction coefficients, the partition function, and heat flux loads. Each of these is calculated for 40,700 time steps, at 0.2 ms increments to simulate the first 8.14 seconds of the test run. These values are used as inputs to the finite difference scheme which calculates melt wear in the slipper due to the applied heat flux load.

The MATLAB code also calculates the inputs to the Abaqus finite element model. The heat flux applied to the bottom of the slipper in the finite difference model is the same heat flux load applied to the bottom of the finite element model. Additionally, the finite element model has loads applied to the front and top surfaces as convective film conditions. The temporal discretization is the same for this model.

Melt wear results generated in each model are compared against one another and to actual melt wear from the January 2008 test run.

A benefit to using the Abaqus commercial finite element package is that model output is easily read and understood. Two-dimensional heat flux vector plots and temperature contour distributions through the slipper are produced over the course of the test run.

A fundamental difference between the two models is how each handles material melt. The finite difference code uses a element removal and a shifting coordinate system to address the non-linear effects of the melt phenomenon. The finite element model does not permit melt removal but incorporates the effects of latent heat as rapidly changing material properties over a small region of the model.

1.7 Assumptions/Limitations

A test run of the rocket sled apparatus at HHSTT is a complex system of mechanical and aerodynamic loads. Capturing and describing the effects of multiple wear modes in a single model is a significant challenge. Therefore, reducing the system to simplified cases (isolation of mechanical gouging or melt due to heating, for example) is required to address unique phenomena related to conditions arising as a result of each of the specific cases. Ultimately, the goal of ongoing research is a combination of the disparate models to a single, unified model that will encompass the results and methodology employed in previous research to fully describe slipper wear effects.

The focus of the current research is characterization of the temperature distribution within the slipper from to mechanical heating due to friction between the slipper and the rail and aerodynamic heating of the slipper resulting from high speed, frictional heating between the slipper and the surrounding air.

Characterizing material wear at high speeds is a complex problem. Wear can generally be classified into two categories, thermal and mechanical. For the purposes of this research, the effects of mechanical wear are ignored. This is an obvious oversimplification. Mechanical wear in the slipper has been considered often in previous research as discussed in Chapter 2. The goal of the current research is to isolate the thermal response of the system so the effects of temperature increase can be studied and applied to future research.

When the velocity of the test apparatus exceeds the speed of sound, a single normal shock is assumed to develop in front of the slipper. Again, this is an oversimplification of the problem. There are numerous shocks created by every surface of the sled apparatus with a projected area perpendicular to the air flow as the sled travels along the rail at supersonic speeds. The shocks will interact and interfere with one another in ways that cannot be reliably predicted without the collection of experimental fluid dynamics data or a detailed computational fluid dynamics model. Further, the slipper under consideration is the actual slipper of the third stage of the rocket sled, so the supersonic air flow will be disturbed by the slipper ahead of it on the third stage sled and by the fourth stage sled (the foremost sled in the train, called the forebody) in the train prior to reaching this slipper. Nevertheless, the assumption of development of a single normal shock in front of the slipper is made for ease of modeling and to give a somewhat conservative evaluation of the shock effect.

The section of the rail interacting with the slipper at any given time throughout the test run is assumed to be at constant temperature and will not impart or remove heat via conduction in addition to the frictional heating. In reality, three slippers will precede the rear, third stage slipper over the rail. Each of these slippers may impart heat to the rail and serve to raise the rail temperature. Additionally, the slipper under analysis will impart some heat to the rail that will propagate forward of the slipper and would affect the heating of the slipper. The increase in magnitude of rail temperature due to frictional heating from slipper contact is not well understood at this time and will therefore be neglected.

In order to simplify modeling of the slipper, the slipper material is assumed to be homogeneous and isotropic. Real-world material is not homogeneous. Impurities and inclusions in the slipper would affect heat distributions such that they would not be the smooth contours seen in Chapter 5 (Results and Analysis). The extent of slipper material inhomogeneity is not known so the slipper material is assumed to be uniform.

The slipper and the rail are not in contact for the entire course of the test run. When the two are in contact, friction between the two surfaces will generate heat flux that will be partitioned between the slipper and the rail. The heat flux will raise temperatures of both the slipper and the rail. For modeling purposes, during the portions of the run that the slipper and the rail are in contact, entire surface of slipper is assumed to be in contact with the rail. In reality, the slipper will undergo rolling, pitching, and yawing motions due to three dimensional loading on the sled apparatus. As a result of these motions, the actual slipper-rail contact area is less than the total area of the slipper face. The actual percentage of interfacial contact at any time is unknown. Assuming the entire area is affected the same amount is done for modeling simplification purposes.

Similarly, the top and bottom surfaces of the slipper are assumed to be parallel to the airflow. The real world rotations would lead to unpredictable, widely varying slipper surface orientations. There is no existing data describing the slipper orientation at a given time. To simplify analysis, the air flow over the top surface is treated as flow over a flat plate and the flow between the slipper and the rail is treated as flow between flat plates. Air flow will be considered in detail in the Aerodynamics section of Chapter 4.

Heat transfer coefficients are assumed to be constant across sections of the top and bottom faces of the slipper (as described in Section 4.4.2 - Convection). The convective heat transfer coefficient would decrease from a maximum value at the front of the slipper to a minimum heat convection coefficient magnitude at the rear of the slipper. The top and bottom surfaces would naturally see higher convection close to the leading edge of the slipper. To simplify modeling, the heat transfer coefficient is assumed to be the mean convection coefficient value for sections of the length of the slipper on the top and bottom faces.

In order to simplify convective heat transfer modeling on the leading edge (front) of the slipper, the film temperature and heat transfer coefficients are both assumed to be constant across the face. Development of heat flux, surface temperatures, and convection coefficients as functions of time is described below in the Aerodynamics and Heat Transfer sections of Chapter 3.

Convective heating of the air due to the temperature difference between the slipper and the air in the gap below will have the effect of changing the temperature of the air in the gap. As the air moves through the gap, the temperature of the air would increase and would, in reality, not be constant. The heating would lead to increased air temperature, smaller temperature difference between the slipper and the air, and therefore less heating of the air from the surface at the rear of the slipper. Additionally, the air is moving through the gap at high speed. The speed at which the air is moving through the gap, and the time intervals studied here insure that most of the heated air from the previous time step has been removed from the gap. As a result, at each time step, most (if not all) of the air between the slipper and the rail is unheated air that was in front of the slipper at the previous time increment. The effects of temperature change and turbulent fluid motion of the air in the gap is difficult to predict and would be an excellent subject of future research analysis, but is beyond the scope of the current research.

The gap height between the slipper and rail when the surfaces are not in contact is assumed to be the maximum allowable gap height ($D = 3.175$ mm). During an actual run, the slipper bounces up and down from the rail and the gap height is constantly varying. The assumption of uniform, constant gap height allows for simplification of modeling the air flow in the gap. As described in the Aerodynamics section of Chapter 3, there are three sections of the airflow along the length of the gap: boundary layer formation at gap entry, boundary layer mergence, and Couette flow between the slipper and the rail at the rear of the gap. The transition points between these three regions is highly dependent on the height of the gap. When the gap is narrow, the boundary layers will merge close to the leading edge of the gap. However, when the gap is at its widest, the mergence point and Couette flow transition will occur further along the gap. The assumption of maximum gap height is made for ease of modeling and to clearly define and observe the effects of convective heating in uniformly defined regions over the course of a modeled run.

The speed of the air in the gap is assumed to be unchanged by the convective heating or by friction between the air and the surfaces of the slipper and the rail. In reality, both heating and friction along the surfaces would change speed of the airflow through the gap. The air is flowing in the gap at close to the speed of sound and the effects of heating, cooling, and friction will have the effect of increasing or decreasing the speed of the flow. [4] For the purposes of modeling simplification, these effects are ignored.

Air flow about the slipper is treated as two-dimensional flow. This is another over-simplification of the system. In reality, the air will flow around the slipper plane cross section in highly unpredictable flows. Further, the slipper is not a slab of infinite depth. Heat would flow across the plane under examination to cooler regions of the slipper. Regions of the wraparound slipper will never come into contact with the rail and will never see direct conductive heating. Heat from the plane studied in this research would naturally flow to those cooler regions. For ease of modeling and to study the region of the slipper most affected by interaction with the rail, the two-dimensional slipper plane is assumed to be a section of the flat plate of the slipper that sits on top of the rail.

Although a number of assumptions have been made prior to model generation and each assumption serves to reduce the realism and scope of the analysis, the temperature contour and melt results obtained are realistic based on comparison to measured results. These results and analysis accomplished here may be confidently applied to future HHSTT wear research endeavors.

1.8 Preview

Having described the slipper-rail interaction problem and the focus of the current analysis here in Chapter 1, the balance of this thesis will describe in detail the research that has been accomplished. Chapter 2 will discuss past research that has been performed, both in wear analysis in general and research into the slipper-rail interaction problem addressed in the present research. Chapter 3 describes fundamental engineering principles that have been applied to the study of heating and melt wear. Chapter 4 describes the application of the engineering principles described in Chapter 3 to the one-dimensional finite difference and two-dimensional finite element models. Chapter 5 presents results obtained from the simulations and analysis of the results. Chapter 6 discusses the significance of the research conducted and the results obtained as well as how the results observed and modeling methods employed may be applied to future wear research analysis.

2 Literature Review

2.1 Chapter Overview

The following sections describe some past research that was conducted in the investigation of both wear, in general, and slipper wear at HHSTT, specifically. The research subjects include: wear due to metal-on-metal sliding contact, consideration of the air flow in the gap between the slipper and the rail, and slipper heating and melt. The chapter is divided into two sections, work conducted outside the Air Force Institute of Technology (AFIT) and research carried out at AFIT. The direct bearing of each case on the high speed, sliding contact slipper wear interaction is discussed.

2.2 Non-AFIT Research

The following is a selection of some historical research that applies directly to the current slipper wear study.

2.2.1 Montgomery

Montgomery [29] performed early research in wear of materials in sliding contact at high speeds. The research was brought about by a US Army need to reduce cannon muzzle wear. Montgomery used experimental data collected by the Army from 1946 to 1956. At the time, cannon muzzle velocities reached speeds in excess of 1,500 m/s. (The maximum velocity reached by the sled in the current study was 1,529 m/s.) The results of the Army study were not released due to classification restrictions.

The Army collected wear data using pin-on-disk experimentation methods. A pin consisting of the material under examination (projectile material) was held in contact with a disk (which consisted of cannon muzzle steel). The disk was rotated at high speeds to generate sliding contact. The experiments were performed using copper, iron, and steel test materials. Disk rotations were conducted for speeds up to 550 m/s.

Montgomery analyzed the data collected by the Army and developed a functional relation for the friction coefficient acting between the metals based on the load pressure and the velocity of sliding contact.

Montgomery's conclusion regarding wear mode is of note, "These data indicate that the mechanism of wear at high sliding speeds is surface melting followed by subsequent removal of a portion of the melted surface layer." [29] A mathematical relationship between Montgomery's data and contact pressure and velocity (developed by Hale [18]) is used in this research to establish the friction coefficient between the slipper and the rail. The relationship and its application to the slipper / rail interaction is discussed in the Load Generation section of Chapter 4.

2.2.2 Wolfson

In 1960, Wolfson [36] completed an investigation of slipper wear rates at HHSTT. Melt had been previously identified as the the primary wear mechanism. Wolfson stated that, "A tremendous heat flux, on the order of 2,500 cal/cm^2-s [1.05×10^8 W/m^2], exists at the slipper-rail interface. This heat flux causes and maintains melting of the slipper bearing material, which is the major wear mechanism." [36] Heat flux magnitudes on the same order are derived from the supplied data and applied to the models run in the present research.

Wolfson attempted to evaluate various coating materials which were applied to sections of the track to reduce of slipper melt wear. The coating would act as a lubricant to reduce the amount of friction and frictional heating between the surfaces. Wolfson determined coatings reduced wear. Coatings are not considered in the current research, but are useful tool in reducing melt ware. Consideration of coatings in future research is advised.

2.2.3 Korkegi and Briggs

Korkegi and Briggs [24] examined the aerodynamic effects of hypersonic ($M_\infty > 5.0$) air flow on the HHSTT sled. Their research focused on the flow field between the slipper and the rail. Their relationships between the freestream air conditions and the air flow conditions in the gap are used in the current research to calculate heat transfer rates and coefficients used to estimate convective heating and cooling effects on the bottom of the slipper when it is not in contact with the rail.

As previous AFIT research, conducted by Laird [25] and Cinnamon[13], noted, Korkegi and Briggs developed a relationship between the freestream, static air pressure (ahead of the shock) and the static air pressure in the gap as a function of distance from the leading edge of the gap $p(x)$ [24],

$$\frac{p(x)}{p_\infty} = \left(\frac{(\gamma+1)M_\infty^2}{2+(\gamma-1)M(x)^2}\right)^{\frac{\gamma}{\gamma-1}} \left(\frac{\gamma+1}{2\gamma M_\infty^2-(\gamma-1)}\right)^{\frac{1}{\gamma-1}} \tag{1}$$

where p_∞ is the freestream air pressure, γ is the ratio of specific heats of air (discussed in the Thermodynamics section of Chapter 3), and M is the Mach number of the flow (defined in the Aerodynamics section of Chapter 3). Equation 1 shows an increase in static pressure across the shock and into the gap. The increased air pressure underneath the slippers (and the entire sled apparatus) is strong enough to overcome the weight of the sled and lift the slipper off of the rail. As noted earlier, the wraparound slipper is designed to hold the sled to the rail when aerodynamic lifting loads overcome the weight of the sled. Variations in aerodynamic lifting over the sled cause significant variation and unpredictability in aerodynamic loading at any location on the sled system at any point in time.

Specific application of Korkegi and Briggs' work to convective heat transfer in the current research is discussed in detail in the Aerodynamics section of Chapter 3. Among the stated conclusions of the their article is the observation that, "Aerodynamic heat rates to the inner surface of the slipper are as high as those at the leading edge and are as high as any encountered on actual re-entry vehicles." The current research attempts to quantify the aerodynamic loads for application to the mathematical models of the slipper over the duration of a test run.

2.2.4 Ashby and Lim

Ashby and Lim [5] discussed multiple wear mechanisms and developed wear maps used to characterize wear due to a sliding interaction. Figure 9 is a representative wear map for steel-on-steel sliding contact. The dominant wear mode in each region of the pressure-velocity distribution is noted.

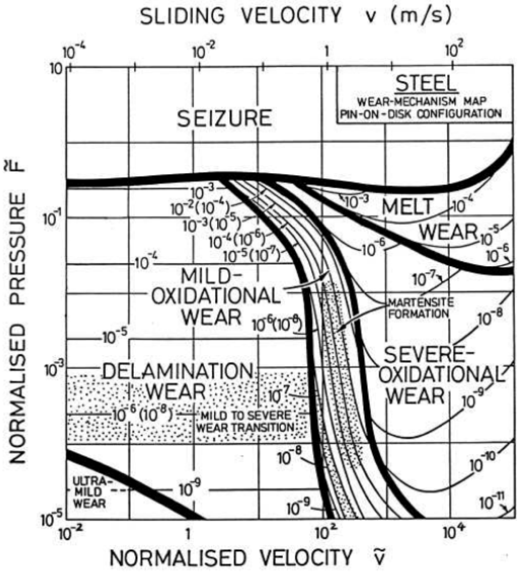

Figure 9: Wear Map. [5]

The high speeds and bearing pressures of the slipper rail interaction fall in the "Melt Wear" region of the map. Ashby and Lim describe melt wear as, "When the bulk temperature exceeds the melting temperature T_m, the lower melting surface is ablated rapidly by melt wear, involving the ejection of liquid droplets or sparks." [5]

2.3 AFIT Research

Students at the Air Force Institute of Technology (AFIT) have been performing slipper wear research for over a decade. The following sections are a selection of results and observations made in the studies.

2.3.1 Laird

Laird [25] perceived the slipper / rail interaction problem as one of hypervelocity gouging. The primary focus of Laird's research was on the mechanical effects of the high speed sliding interaction. A component of Laird's research included a simplified finite difference scheme with constant, equivalent heat sources on the front and bottom surfaces of the slipper. Figure 10 shows the temperature distribution in the slipper after 5 seconds.

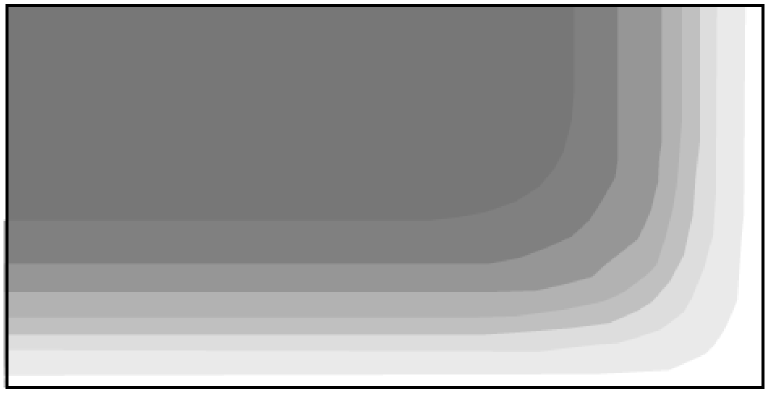

Figure 10: Slipper Temperature Profile. [25]

Laird does not present temperature values for the finite difference solution. The distribution is shown for qualitative purposes only. The finite element model employed in the current research is similar, but expands on Laird's model considerably.

Laird concluded, "Successful modeling of gouging should include modeling the temperature environment, as the slipper temperature has proven to have a significant effect on the material yield stress and its resistance to gouging."

2.3.2 Lofthouse

Where the current research focus is on characterization the temperature distribution in a cross section of a single slipper, Lofthouse [27] studied the rocket sled problem through a wider lens. Lofthouse performed a computational fluid dynamics analysis of the over the front region of the lead car in the sled. The analysis looked at shock formation, shock interaction, and shock effects around the test apparatus for sled Mach numbers up to

$M = 3.0$. Lofthouse concluded, “The thermodynamic properties of the flow around the hypervelocity sled are strongly affected by discontinuities of the flow, such as shock waves, expansions and their interactions.” The current research applies shock effects to the aerodynamic heating of the slipper on the front, top, and bottom surface, to include air flow analysis in the gap between the slipper and the rail. Lofthouse’s model did not consider the flow between the slipper and the rail.

2.3.3 Cinnamon

Cinnamon [13] performed a thorough examination of hypervelocity gouging, but, for the most part, did not consider thermal effects. Cinnamon used Chi to the Three Halves Eulerian Shock Wave Physics Code (CTH) to simulate gouging. Though temperature increases occurred during gouge simulations, all but one of the simulations were initiated at room temperature. Cinnamon conducted one simulation at an elevated initial temperature of 1,200 K. A “slight” increase in gouge depth was noted. Cinnamon observed, “While this is certainly not an exhaustive study on the topic, it is interesting to note the small amount of contribution the heated shoe had to the overall results.” [13]

2.3.4 Hale

Although primarily focused on mechanical wear, Hale’s [18] consideration of slipper melt wear was more detailed than prior AFIT research had been. Hale used an older version of the finite difference scheme used in the current research to determine slipper temperatures and estimate melt. At the time, the code did not account for slipper bounce with corresponding convective heat loss and did not directly calculate slipper melt. Further, equally distributed heat flux partitioning (50% to the slipper and 50% to the rail) was assumed constant for the duration of the test run.

Hale’s research did attempt to include the effects of flash temperature (an instantaneous increase in surface temperature upon collision) on melt. Flash temperature is not considered in the current research.

Hale’s predicted a total melt wear volume of 54 mm^3 and total mechanical wear volume of 3,706 mm^3, for a combined wear prediction of 3,760 mm^3. This is 35.7% of the total experimentally measured wear volume of 10,516 mm^3 experimentally measured in slipper from the January 2008 test run. Thus, while the estimation is low, the total wear volume results are on the order of those seen in the actual slipper. Hale concluded the estimations are acceptable based on the number of underlying assumptions involved in model development and experimental methodology.

2.3.5 Le

Le's wear research [26] focused on the determination of a function to describe the partitioning of heat flux between the slipper and the rail (Fig. 11). In the diagram, q'' is the heat flux, α is the partition function, and v is the velocity of the slipper / sled.

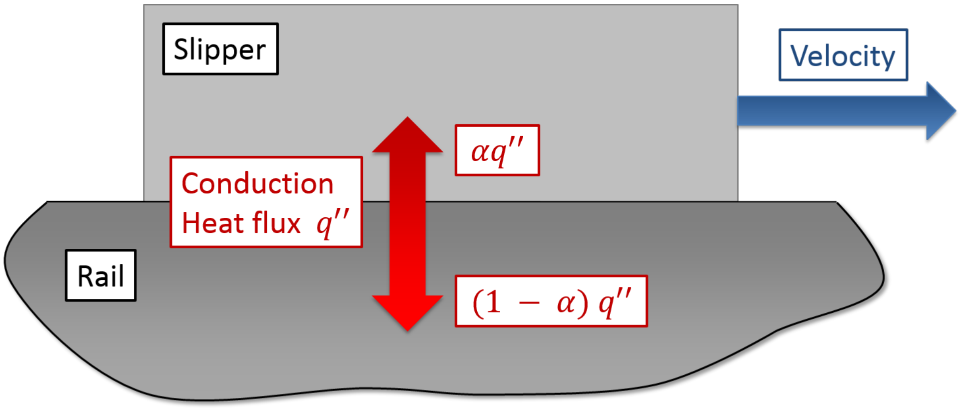

Figure 11: Heat Flux Partitioning.

Le assumed that, at the start of each test run, total frictional heating is imparted to the slipper and the rail in equal portions. As the run progresses, less heat is transferred into the slipper and more heat is transferred into the rail. This phenomena occurs for two reasons. First, at test initiation, the slipper and the rail are assumed to be at the same temperature (293 K). As frictional heating due to sliding occurs in the slipper, the temperature in the slipper increases and the slipper becomes less able to take on additional heat. So as the slipper moves down the track at high speed, the temperature continues to increase in the slipper but more and more slowly. The second reason for this phenomenon is, from the perspective of the slipper, the temperature of the rail remains constant. The temperature of the rail is assumed to be constant at 293 K.

Le's work with heat flux partitioning is discussed in greater detail in Section 4.4.1.

2.3.6 Buentello

Buentello [10] investigated mechanical wear in the slipper through implementation of a 3-dimensional finite element model. Buentello modeled the slipper / rail interaction with focus mechanical wear due to collisions between the moving slipper and raised asperities on the surface of the rail. The model employed Johnson-Cook failure criteria to identify failure and remove failed elements. The slipper melt temperature is included in the Johnson-Cook failure criteria and Buentello did incorporate temperatures corresponding to sled velocity as determined in Le's research, but no thermal loads were applied to the model and melt was not a factor in the analysis.

Buentello [10] and Cinnamon [13] both observed that, as the sled travels down the rail, the acceleration of the sled will naturally cause a forward rotation (or rolling motion) of the slippers about their central axis. The slipper forward rotation may be seen in both images in Fig. 12. Although these photos were not taken during the January 2008 test run, similar rolling motion is assumed to have occurred.

(a) 80X-G1 Test Mission, April 2003, V = 2,853 m/s.

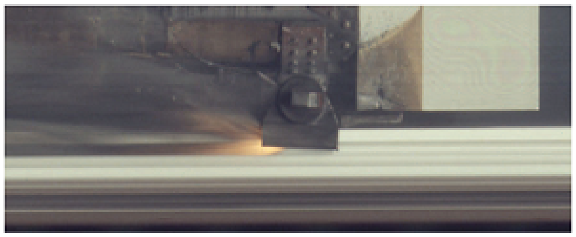

(b) 80X-G1 Test Mission, April 2003, V = 2,861 m/s.

Figure 12: Slipper Rotation. [10]

According to Buentello [10], the rolling motion in the slipper leads to asymmetric wear along the bottom slipper surface, as seen in Fig. 13. The sled begins a run with zero initial velocity. When the first rocket engages, the entire apparatus begins to accelerate down the track. The acceleration causes the slipper to roll forward onto its front edge. The slipper front edge feels the pressure load from the weight of the sled. This pressure load causes friction which leads to wear on the leading edge of the slipper. At the end of the first stage, the front edge of the slipper will have worn 140 mm, as seen in Table 1. The wear process repeats in the same manner during both the second and third stages.

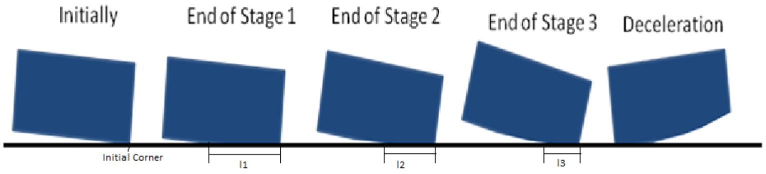

Figure 13: Slipper Contact. [10]

When the third stage has expended its fuel, the third stage sled is decoupled from the fourth and, lacking the forward propulsive force from the rocket, begins to skid to a halt. Buentello asserts that the deceleration wears on the rear of the slipper surface. Table 1 lists wear length for the four segments of the test run.

Table 1: Slipper Wear Length. [10]

Mission Phase	Start Time (s)	End Time (s)	Worn Length (mm)
Stage 1	0	1.9	140
Stage 2	1.9	3.8	70
Stage 3	3.8	5	45
Deceleration	5	8.14	70

In the current research, the finite element model treats the entire surface of the slipper as though it is in contact with the rail at all points in the run that the slipper is not bouncing. The finite difference code is used to study the effects of loading at a single point. So the point may be changed to examine effects of loading conditions at different locations. Finite difference results are presented in Section 5.2.

2.4 Summary

Past studies of slipper wear due to the sliding iteration with the rail have generally focused on mechanical wear. Some work has incorporated aspects of heating, examined a single test case at elevated temperature, or, at least, acknowledged that heating effects and elevated temperature should be taken into account.

The current research focuses on the thermal aspect of slipper wear and does not consider mechanical wear. Application of this, more thorough, examination of slipper heating and melt wear may be applied to thermomechanical slipper wear models in future research efforts.

3 Theory

3.1 Chapter Overview

Before discussing the modeling techniques employed in this research, it is necessary to discuss engineering principles of material (solid and fluid) behavior. Temperature change due to friction generated heat flux and aerodynamic heating and cooling will change the material behavior of the slipper and the surrounding air. Fundamental thermodynamics of material heating and phase change must be understood. The sled travels at supersonic speeds which requires the employment of high speed, incompressible aerodynamics principles. Finally, a discussion of fundamental heat transfer mechanisms is necessary to understand how large amounts of heat are transferred between the air and the slipper and how heat propagates within the slipper itself. The theory described in this chapter will lead to the development and application of the slipper loads described in the following chapters.

For clarity, all of the theory involved in developing loading of the model applies to the finite element model. The only loading on the finite difference model is applied to the bottom surface. Discussion pertaining to the front and top surfaces only pertains to the finite element model.

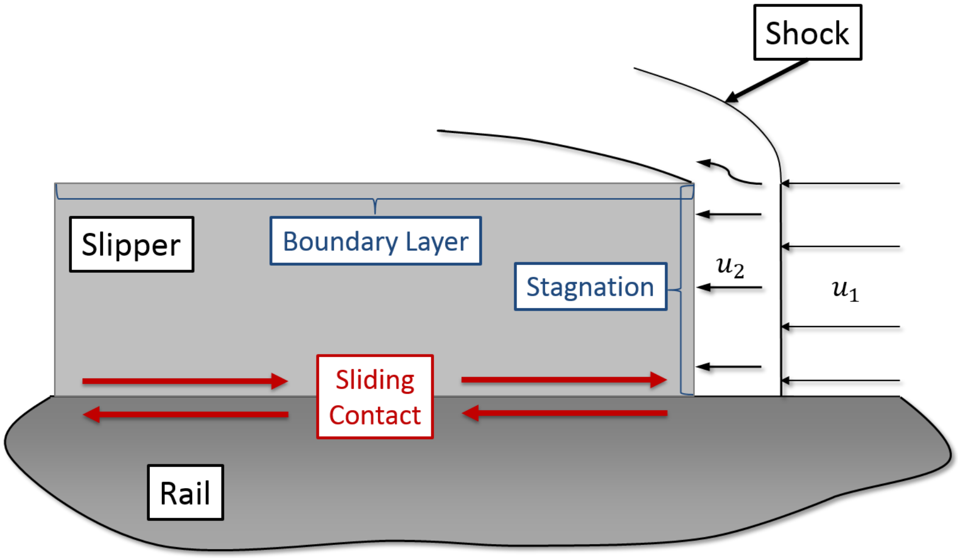

Figure 14: Contact.

The principles discussed are applied to loading in the following two cases: slipper in contact with the rail (Fig. 14) and the slipper bouncing above the rail (Fig. 15). These two figures represent the modeled physical behavior of the slipper under consideration. The slipper height $H = 14.7$ mm and length $L = 203.2$ mm.

In Fig. 14, the trans-shock property relationships (the ratio between the air speed in front of the shock u_1 and the air speed behind the shock u_2, for example) are dealt with in Section 3.3.1. Boundary layers are discussed in Section 3.3.2 and stagnation / total temperature is covered in Section 3.6.1. Convective heating generated by the sliding contact between the slipper and the rail is discussed in Section 4.4.2.

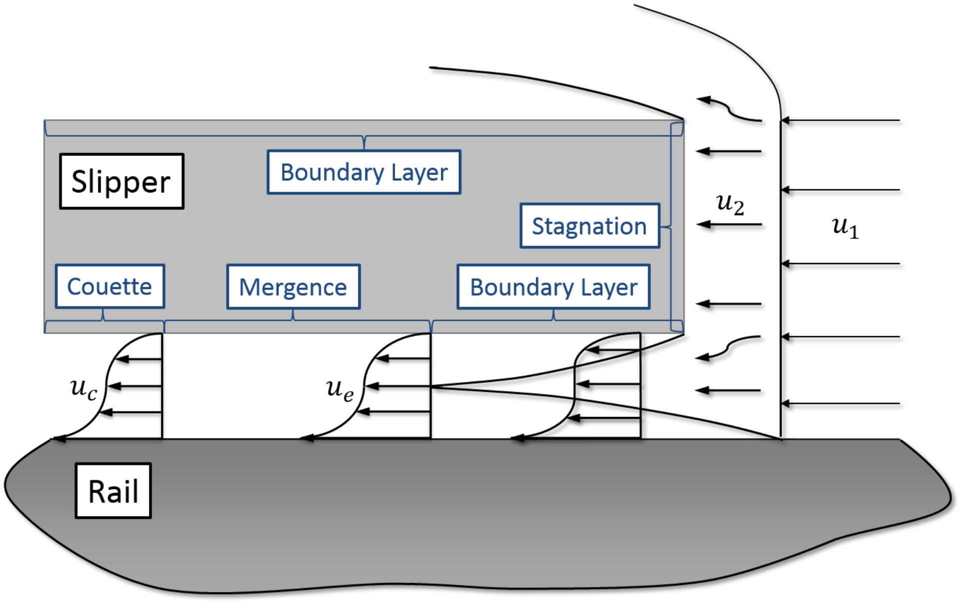

Figure 15: Bounce.

For Fig. 15, additional concepts relate to the flow in the gap between the slipper and the rail. Gap air flow is covered generally in Section 3.4 and Couette Flow is handled specifically in Section 3.5. The speed of the air flow at the edge of the boundary layer and at the midpoint of the mergence flow height is u_e, where the subscript e is used to indicate "edge" of the boundary layer. The flow speed in the center of Couette flow is u_c.

3.2 Thermodynamics

3.2.1 Air Properties

When analyzing low velocity, low temperature fluid flows a few assumptions are typically made. [34] First, the following equation of state holds for a perfect gas,

$$p = \rho R T \tag{2}$$

where p is air pressure, ρ is air density, R is the specific gas constant (287 J/kg-K for air), and T is temperature. Equation 2 is the ideal gas law.

The second assumption is that the specific heats (c_p and c_v) are constant. The specific heat at constant pressure c_p defined as,

$$c_p = \left.\frac{\partial \bar{h}}{\partial T}\right|_p \tag{3}$$

The second is the specific heat at constant volume,

$$c_v = \left.\frac{\partial \bar{u}}{\partial T}\right|_v \tag{4}$$

where $\bar{h}$ is enthalpy and $\bar{u}$ is internal energy.

Specific heat (or heat capacity) describes a material's capacity for temperature increase when heat is added to a body consisting of the material. A material's specific heat is the amount of heat required to raise the temperature of a 1 kg mass consisting of the material by 1 K. [22] At low temperatures, specific heats may be treated as constant. At elevated temperatures, such as those seen within the slipper and the thermal boundary layer by which the slipper is surrounded, specific heat is temperature dependent. As heat is imparted to a material (solid or fluid), the material's temperature increases.

The third assumption is that the Prandtl number Pr is constant,

$$Pr = \frac{c_p \mu}{k} \propto \frac{\text{frictional dissipation}}{\text{thermal conductivity}} \tag{5}$$

where μ is the dynamic viscosity and k is the thermal conductivity of the air. From Incropera and DeWitt, "The Prandtl number provides a measure of the relative effectiveness of momentum and energy transport by diffusion in the velocity and thermal boundary layers."[17] From Anderson, "In the study of compressible, viscous flow, Prandtl number is just as important as γ, Re_∞, or M_∞."[3]

Fourth, the dynamic viscosity of the fluid μ is dependent on the temperature of the fluid. The relationship for viscosity variation is called Sutherland's formula,

$$\frac{\mu}{\mu_\mathrm{r}} = \left(\frac{T}{T_\mathrm{r}}\right)^{3/2} \frac{T_\mathrm{r} + \theta}{T + \theta} \tag{6}$$

where the r subscript indicates the reference value. For air, $\theta = 110$ K. For the purposes of the current research, the reference temperature $T_{\mathrm{r}} = 293$ K and the reference viscosity $\mu_{\mathrm{r}} = 18.185 \times 10^{-6}$ kg/(m-s). [34]

These assumptions typically hold for moderate pressures and temperatures less than 500 K. [34] The air temperatures seen in the flows behind the shock and around the slipper quickly rise to values greater than 500 K, so the assumption of constant specific heat is no longer valid.

Another important term in gas calculations is the ratio of specific heats γ,

$$\gamma = \frac{c_p}{c_v} \tag{7}$$

In the case of a calorically perfect gas, for which the four above assumptions apply, the ratio of specific heats for air is assumed to be constant $\gamma = 1.4$. For the temperature ranges seen in the current analysis, the ratio of specific heats varies from 1.4 at low temperatures to a value of approximately 1.31 at the highest temperatures.

For the purposes of this research, the value of $\gamma = 1.4$ is used for the calculation of trans-shock properties due to computational complexities involved in the variation of the ratio of specific heats across the shock. Specifically, there is no closed form solution for the temperature ratio across the shock with variation of specific heats. For the maximum Mach number seen in present study ($M_{\max} \approx 4.5$), the pressure ratio across the shock p_2/p_1 is only slightly under-predicted by the ideal gas assumption. The temperature ratio T_2/T_1 (from Eq. 20) across the shock is over-predicted by $\approx 4\%$. The 1 and 2 subscripts indicate air flow conditions ahead of and behind the shock, respectively. Additional discussion of trans-shock effects may be found in Section 3.3.1. Behind the shock, calculations are more straightforward and the ratio of specific heats varies appropriately with temperature according to Eq. 55. [8] [15]

A plot of ratio of specific heat variation with temperature may be seen in Appendix 1.

3.2.2 Latent Heat

When a material undergoes a solid-liquid phase change (melt), energy which had been stored in the material is released. How a given material reacts to energy influx at the melt boundary depends on the material's latent heat of fusion (a material property).

The Clausius-Clapeyron equation describes conditions at a phase change boundary [22]. For melt the equation is,

$$\frac{dp}{dT} = \frac{s_{\text{liq}} - s_{\text{sol}}}{\bar{v}_{\text{liq}} - \bar{v}_{\text{sol}}} \tag{8}$$

where p is pressure and T is temperature at the melt boundary, s is entropy, and $\bar{v}$ is specific volume. The subscripts liq and sol indicate liquid and solid phases, respectively. In a pressure-temperature diagram, Eq. 8 represents the slope of the boundary line between solid and liquid phases. At a constant temperature, the phase change occurs along an isobar ($p =$ constant) [22] so the Second Law of Thermodynamics,

$$Tds = d\bar{h} - \bar{v}dp \tag{9}$$

where $\bar{h}$ is enthalpy, becomes,

$$Tds = d\bar{h} \tag{10}$$

Integrating across the melt boundary yields,

$$T(s_{\text{liq}} - s_{\text{sol}}) = \bar{h}_{\text{liq}} - \bar{h}_{\text{sol}} \tag{11}$$

The latent heat of fusion for a solid-liquid phase change is defined as [22],

$$l = \bar{h}_{\text{liq}} - \bar{h}_{\text{sol}} \tag{12}$$

The magnitude of the latent heat of fusion defines the relative ease of material melt.

Chapter 4 presents a discussion of how the finite difference and finite element models each handle melting slipper material using the latent heat of fusion of VascoMax 300.

3.3 Aerodynamics

In most previous wear analyses of the slipper and rail interaction, aerodynamic heating and cooling have largely been ignored or neglected. The speed of the test apparatus for this particular run approaches 4.5 times the speed of sound. At that speed, there are significant convective effects acting on the bottom, front, and top surfaces of the slipper that need to be taken into account.

The primary source of heat flux on the bottom of the slipper is conductive heating as a result of the friction generated through the high velocity sliding interaction. Of course, conductive heating occurs only when the slipper and the rail are in contact with one another. As discussed previously, aerodynamic loads on the entire sled apparatus have the effect of lifting the sled off of the rail so that the bottom surface of the slipper and, for much of the run, the rail are not in contact. When lifting occurs, a gap forms between the slipper and the rail and high speed air flow moves through the gap. Whether the air flow heats or cools the surface of the slipper depends on the temperature difference between the air and the slipper. If the air is hotter than the slipper, the air will heat the slipper and if the air is cooler the air will have a cooling effect on the slipper. Heat flux naturally travels in the direction from a hot region to a cold region. This phenomena is described by Newton's Law of Cooling [17],

$$q'' = h(T_{\mathrm{s}} - T_\infty) \tag{13}$$

where q'' is heat flux, h is the convective heat transfer coefficient, T_{s} is the temperature at the surface, and T_∞ is the freestream temperature.

Both heating and cooling of the slipper occur during the course of the 8.14 second January 2008 test run. In this research, film temperatures are used in place of T_∞ in Eq. 13. Calculation of the total and adiabatic wall film temperatures and heat transfer determination are explained in Section 3.6.

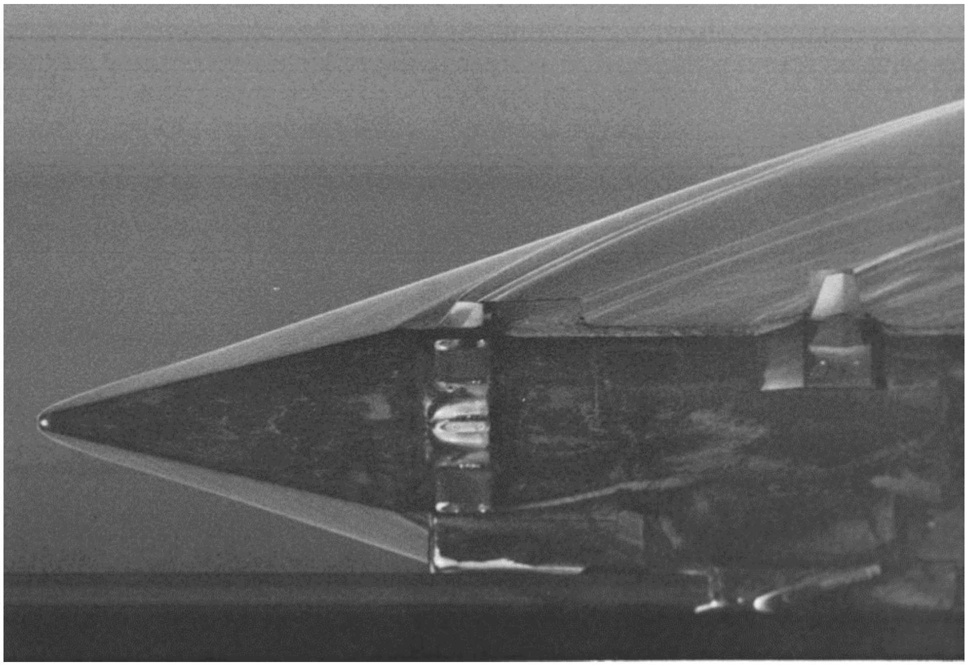

Figure 16: Shocks and Aerodynamic Heating. [25]

3.3.1 High Speed Aerodynamics

A body traveling through a fluid medium influences the fluid particles ahead of the body in the direction of the motion of the body. The fluid particles propagate away from the moving body at the speed of sound a in the given fluid,

$$a = \sqrt{\gamma R T} \tag{14}$$

where γ is the ratio of specific heats of the fluid (taken to be 1.4 for air), R is the specific gas constant (for air, $R = 287$ J/kg-K), and T is the fluid temperature. As the speed of the moving body reaches and surpasses the speed of sound of the fluid, it becomes impossible for the fluid particles to move away from the body as the fluid particles are unable to move faster than the speed of sound. Instead, the fluid particles gather in front of the body and create a sort of buffer zone between the undisturbed flow ahead of the body and the body itself. This phenomenon is known as a shock. Behind the shock, the fluid properties and flow characteristics are markedly different than they are ahead of the shock, as detailed for specific fluid properties below. Shock effects are important to consider for this study because the sled travels slower than the speed of sound for only the first 1.84 seconds of the 8.14 second run time. After 1.84 seconds, shock effects are seen for the remainder of the test run. At 8.14 seconds, the third stage sled is decelerating and is traveling at supersonic speed. DADS data does not exist past 8.14 seconds, so the final portion of the run is not considered.

Following development of the shock, the air flow conditions seen by the slipper are no longer the same as they had been prior to the shock formation. Anderson [4] derives the flow relationships across the shock beginning with the following conservative relations, Conservation of mass:

$$\rho_1 u_1 = \rho_2 u_2 \tag{15}$$

Conservation of momentum:

$$p_1 + \rho_1 u_1^2 = p_2 + \rho_2 u_2^2 \tag{16}$$

Conservation of energy:

$$\bar{h}_1 + \frac{u_1^2}{2} = \bar{h}_2 + \frac{u_2^2}{2} \tag{17}$$

where ρ is mass density, u is air speed, p is pressure, and $\bar{h}$ is the enthalpy of the air. The subscripts 1 and 2 are used to indicate the flow conditions ahead of (1) and behind (2) the normal shock. The change of properties across the shock occurs adiabatically, no heat is added or removed from the flow to change the conditions across the shock.

The Mach number is a commonly used dimensionless parameter used to describe the speed of a body in a fluid relative to the speed of sound in that fluid,

$$M = \frac{v}{a} \tag{18}$$

where v is the speed of the body and a is the speed of sound in the fluid, given by Eq. 14.

The relationship between the Mach number ahead of the shock M_1 is and the Mach number behind the shock M_2 is,

$$M_2^2 = \frac{1 + [(\gamma - 1)/2]\, M_1^2}{\gamma M_1^2 - (\gamma - 1)/2} \tag{19}$$

where, again, γ is the ratio of specific heats of air. Equation 19 shows that the Mach number behind the shock is less than the Mach number ahead of the shock. The flow is subsonic behind the shock. The gap Mach number is calculated on the edge of the boundary layer in the gap using velocity u_e in Eq. 28 of Section 3.4 and post-shock temperature T_2 in Eq. 20. For the majority of the run, the Mach number at the edge of the boundary layer is 0.9.

Figure 17 shows the Mach number as a function of time in front of and behind the shock.

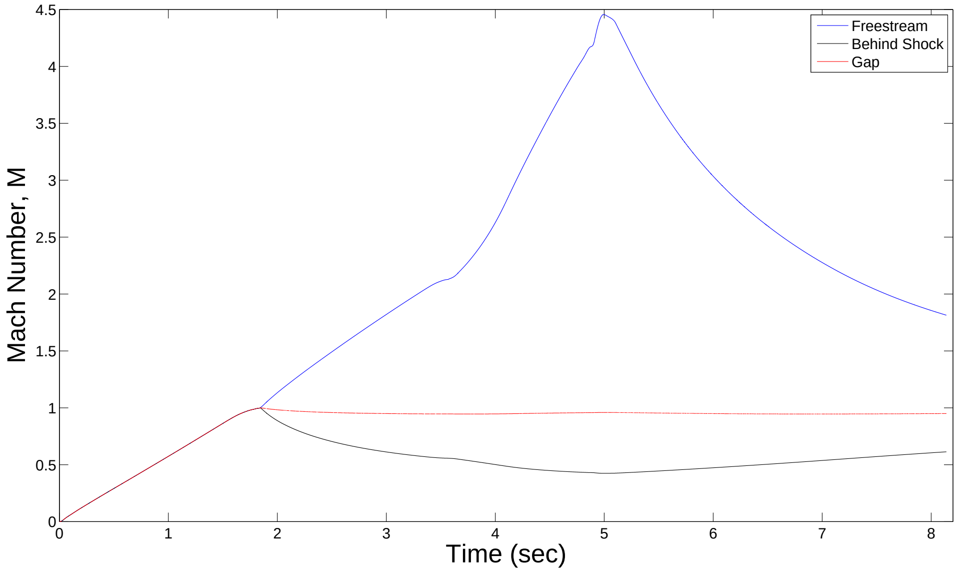

Figure 17: Mach Number vs Time.

The decrease in Mach number is due to slowing of the relative air speed (from the perspective of the slipper) and the increase in temperature of the air behind the shock. The temperature of the air behind the shock increases according to the following [4],

$$\frac{T_2}{T_1} = \left[1 + \frac{2\gamma}{\gamma+1}(M_1^2 - 1)\right]\left[\frac{1+(\gamma-1)M_1^2}{(\gamma+1)M_1^2}\right] \tag{20}$$

where T_1 is the temperature in front of the shock (assumed to be the ambient temperature, 293 K) and and T_2 is the air temperature behind the shock. The variation of the post-shock temperature (T_2) over the course of the run is shown in Fig. 95 in Appendix 1.

Flow velocity decreases and density increases across the shock at the same ratio, given by Eq. 21.

$$\frac{\rho_2}{\rho_1} = \frac{u_1}{u_2} = \frac{(\gamma-1)M_1^2}{2+(\gamma-1)M_1^2} \tag{21}$$

Trans-shock calculations are all made using the constant pre-shock value for the ratio of specific heats ($\gamma = 1.4$). The value of the ratio of specific heats will change with the temperature increase across the shock and calculation of the post-shock properties becomes cumbersome. For example, there is no closed form solution for the temperature change and the post-shock temperature calculation would require an iterative, numerical scheme at each time step. At the maximum sled Mach number (M $\approx$ 4.5), the assumption of a constant ratio of specific heats will yield temperature overprediction by less than 5%. For Mach number less than 4.5, the perfect gas assumption will provide more appropriate post-shock values. [15]

3.3.2 Boundary Layers

The discussion of boundary layers presented here leads to an understanding of the mechanism for heating the air surrounding the slipper due to high speed air flow and the transference of generated heat from the air into the slipper.

When a fluid flows past an object, the fluid particles at the surface stick to the object and have the same velocity as the object. If the object is not moving, the fluid at the surface has no velocity ($u_s = 0$). This "no-slip" condition generates a shear force τ_s on the wall of the object. The coefficient of friction C_f between the air and the surface of the object is defined as,

$$C_f \equiv \frac{\tau_s}{\rho u_\infty^2/2} \tag{22}$$

where ρ is the density and u_∞ is the freestream velocity of the fluid. The fluid near the surface is affected by the particles at the surface and do not move around the object as fast as the fluid particles in the freestream. The region of slower moving air flow is the velocity boundary layer.

Boundary layer thickness is conventionally defined as the distance above a surface where the fluid flow speed is 99% of the freestream flow speed $u = 0.99u_\infty$. [17] Turbulent boundary layer thickness δ in flow over a flat plate is given by the following expression [3],

$$\delta = \frac{0.37x}{\mathrm{Re}_x^{1/5}} \tag{23}$$

The Reynolds Number Re_x in Eq. 23 is a dimensionless parameter used to describe similarity of fluid flow conditions. The Reynolds Number is defined as the following,

$$Re_x \equiv \frac{u_\infty x}{\nu} = \frac{\rho u_\infty x}{\mu} \tag{24}$$

where u_∞ is the speed of the fluid flow x is the location on the surface (measured from the leading edge, see Fig. 19) at which the Reynolds number is evaluated, ν is the kinematic viscosity, ρ is the density, and μ is the dynamic viscosity of the fluid.

Transition from laminar flow to turbulent flow is expected to occur when $\mathrm{Re} > 10^5$. For the case of the slipper wall, the air is traveling past the slipper at high enough speed and the surface of the slipper is sufficiently rough that the flow over the top and bottom surfaces is turbulent almost immediately following first stage initiation. Figure 18 shows boundary layer thickness on the top and bottom surfaces at $x/L = 0.42$ (from the leading edge of the slipper in Fig. 19).

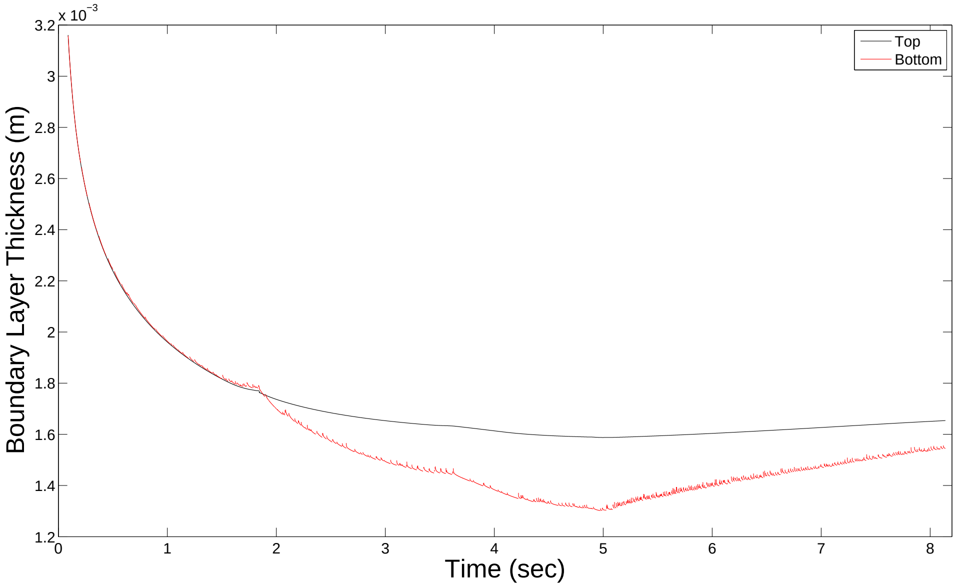

Figure 18: Turbulent Boundary Layer Thickness vs Time, $x/L = 0.42$.

The boundary layer thicknesses in Fig. 18 are only shown for $\mathrm{Re} > 10^5$. In the short period of time for which $\mathrm{Re} < 10^5$, the flow may be laminar. However, the duration of this period is ≈ 0.1 second and surface roughness may initiate turbulent flow even earlier than that. Therefore, the possibility of laminar flow is ignored and the flow is treated as turbulent for the duration of the test run. Compressible turbulent flat plate wall friction coefficient C_f is determined using the following relationship [3],

$$C_f = \frac{0.074}{(Re_c)^{1/5}} \tag{25}$$

where the c subscript in the Reynold's number term indicates the characteristic length is the length of plate, in this case the slipper length, $L = 203.2$ mm.

When there is a difference in temperature between the surface of the body and the fluid flow, a thermal boundary layer forms at the surface of the object, in addition to the velocity boundary layer. The thermal boundary layer thickness δ_{T} is defined as the distance from the surface where, $[(T_s - T)/(T_s - T_\infty)] = 0.99$. Where T_s is the temperature at the surface, T_∞ is the temperature of the fluid freestream, and T is the temperature at a point within the thermal boundary layer. The Prandtl number indicates the relative thickness of the thermal and velocity boundary layers. In the case of air, where the Prandtl number is less than one, the thermal boundary layer thickness is greater than the velocity boundary layer thickness. [3]

Since there is no fluid motion at the surface of the body, heat transfer will occur by convection only and Fourier's Law applies,

$$q_{\mathrm{s}}'' = -k \frac{\partial T}{\partial y}\bigg|_{s} \tag{26}$$

Combining Eq. 13 with Eq. 26 yields,

$$h = \frac{-k}{(T_{\mathrm{s}} - T_{\infty})} \frac{\partial T}{\partial y}\bigg|_{s} \tag{27}$$

where h is the heat transfer coefficient and k is thermal conductivity. These properties will be discussed further in the Heat Transfer section below.

3.4 Gap Air Flow

This section describes the principles employed to define the heat flux applied to the bottom of the slipper when the slipper is bouncing. The Korkegi and Briggs [24] gap flow analysis divides the gap into four heat transfer regions: (1) stagnation point, (2) boundary layer, (3) mergence, and (4) couette flow. Figure 19, adapted from Korkegi and Briggs, shows the four regions. Heat flux due to the variations in the flow are applied to the corresponding regions of the finite element model. The heat flux in the finite difference model is only applied at a single point. The average value of the heat transfer coefficient for the boundary layer region was chosen as the application location in the finite difference model, for simplicity.

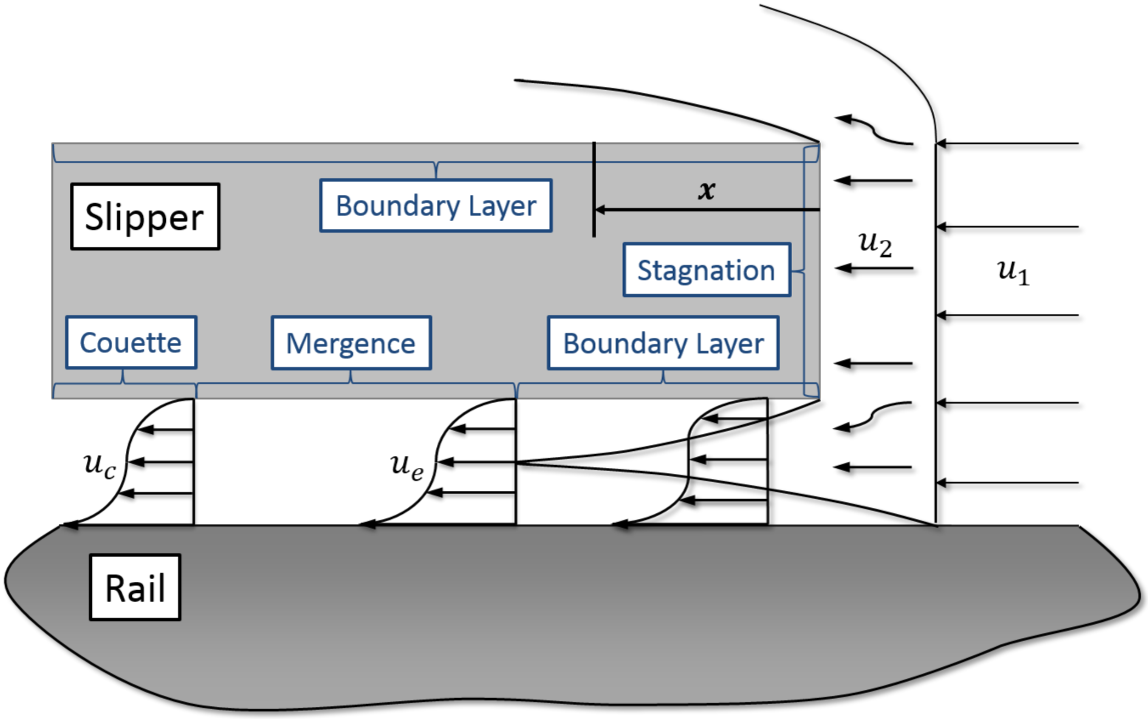

Figure 19: Air Flow Around Slipper. [24]

In the first heat transfer region, the stagnation point, the air flow comes to a stop at a point and all of the mechanical energy carried by the particles to this point becomes thermal energy and resulting temperature increase heats the slipper. Korkegi and Briggs studied a blunt-nosed slipper and, in the case of the blunt-nosed slipper, the air flow comes to a stop at a single stagnation point on the leading edge. The leading edge of the slipper in the present research is flat (face perpendicular to the flow field), so the entire front surface is treated as a "stagnation point." The total temperature concept is employed to determine heat flux on the front surface. Total temperature is discussed in detail in the Heat Transfer section of this chapter (Section 3.6).

The convective heating analysis of the bottom surface applies heat transfer principles developed for air flowing over flat plate. Analogous to the Korkegi and Briggs analysis, three heat transfer regions are considered on the bottom of the plate: boundary layer, mergence, and Couette flow.

The speed at the edge of the velocity boundary layer on the bottom of the slipper during bounce u_e is given by the following relationship [24],

$$u_\mathrm{e} = u_\infty \left(\frac{\gamma - 1}{\gamma + 1}\right)^{1/2} \left(1 + \frac{2}{\gamma - 1}\frac{1}{M_\infty^2}\right)^{1/2} \tag{28}$$

where u_∞ is the freestream velocity, γ is the ratio of specific heats, and M_∞ is the freestream Mach number. The boundary layer exists behind the shock so the ratio of specific heats will vary with temperature. The ratio of specific heats is calculated at the elevated, post-shock temperatures using Eq. 55 and are shown in Fig. 97 of Appendix 1.

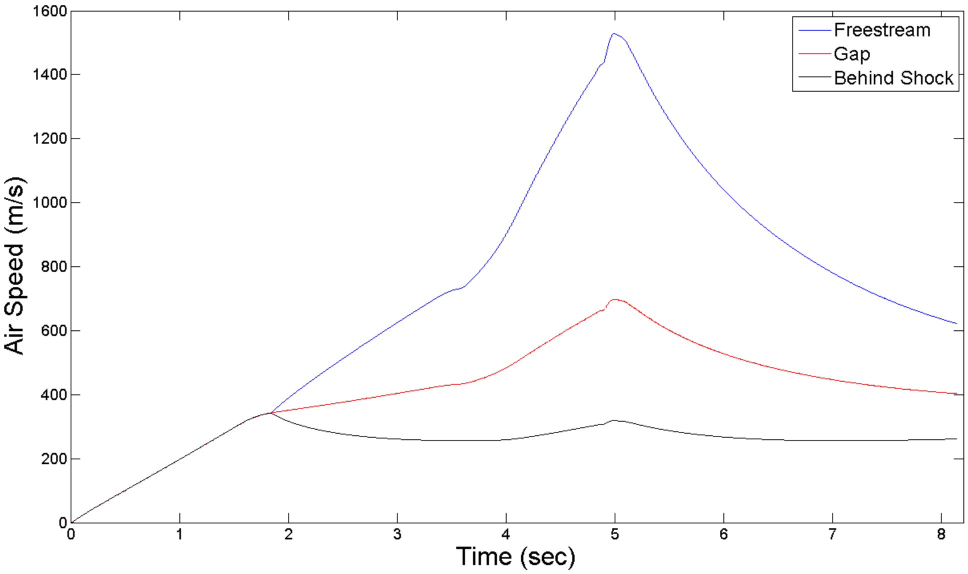

Figure 20: Air Speed.

The velocity boundary layer thickness on the underside of the slipper is calculated using Eq. 23 where the Reynolds number in Eq. 24 is found using the boundary layer edge velocity from Eq. 28, the post-shock density from Eq. 21, and viscosity calculated using Sutherland's Formula (Eq. 6) using the post-shock temperature.

In the boundary layer region, convective heating and cooling occurs through viscous heating in the thermal boundary layer. In the boundary layer regions on the upper and lower surfaces of the sliper, the adiabatic wall concept is employed to determine convective heat flux.

In addition to the boundary layer on the underside of the slipper, a second gap boundary layer on the rail develops. The rail boundary layer is initiated by the shock. The thickness of the rail boundary layer is given by Eq. 23, but the rail Reynolds number Re_r expression is

$$\mathrm{Re}_r = \frac{\rho_e(u_\infty - u_e)}{\mu_e} \tag{29}$$

where ρ_e is the density at the boundary layer edge, u_∞ and u_e are the freestream and boundary layer edge air speed, respectively, and μ_e is the boundary layer viscosity. For this research the density and viscosity at the boundary layer edge are taken to be the post-shock density and viscosity calculated at the post-shock temperature using Sutherland's Formula (Eq. 6).

As the flow progresses through the gap, the velocity boundary layer thickness of both the boundary layer on the slipper and the boundary layer on the rail increase. At some point in the gap, the boundary layers will merge to form a full shear layer tending toward Couette Flow (as described in Section 3.5). The point where two boundary layers come together is what Korkegi and Briggs [24] term the "mergence point". This happens when the cumulative height of the two boundary layers is equal to the height of gap between the slipper and the rail. The boundary layer heights and their sum are shown for the duration of the test run in Fig. 21 at $x/L = 0.525$ from the front of the gap. Again, the gap height is always assumed to be the maximum possible gap height, $D = 3.175$ mm. (The maximum gap height is shown as a horizontal line in Fig. 21). So, at $x/L = 0.525$ from the front, the boundary layers are merged for the entire run of the rocket sled test.

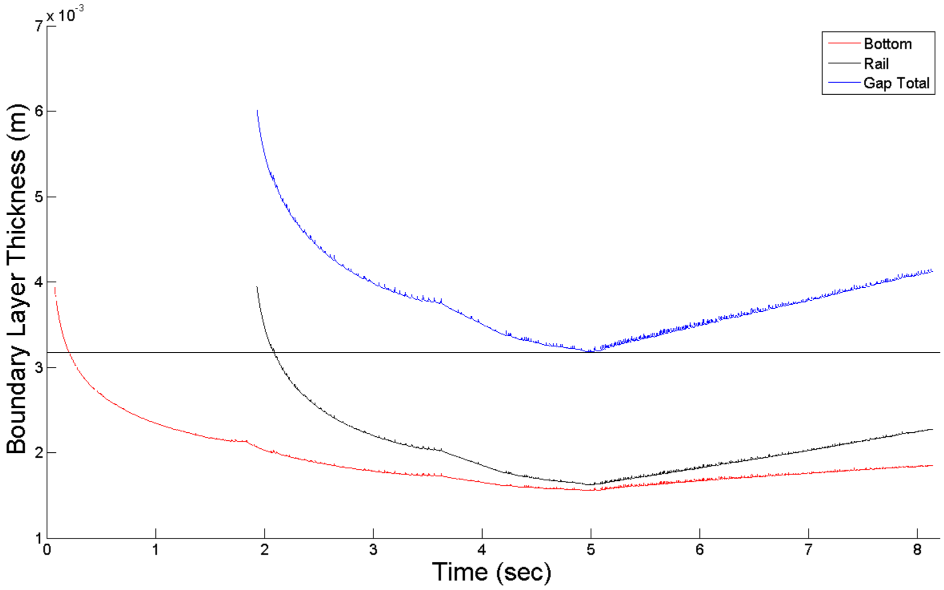

Figure 21: Boundary Layer Mergence vs Time, $x/L = 0.525$.

At the mergence point, the velocity boundary layer velocity u_e is the velocity in the middle of the gap. As the flow continues through the gap, it will tend toward Couette Flow (described in the following section). [24] As the velocity profile evolves from the mergence point to full Couette flow, the velocity in the middle of the gap evolves from u_e at the mergence point to the Couette flow velocity, $u_c = u_\infty/2$, shown in Fig. 22.

Heat transfer variation in the transition region from the mergence point to the Couette flow region is assumed to be a linear variation from the boundary layer heat flux values at the slipper mid-length to the Couette heat flux values on the rear-most section of the slipper length.

3.5 Couette Flow

This section describes Couette flow and heat flux generation at the slipper wall in this region.

The flow field at the rear of the gap is considered as Couette flow. Couette flow occurs between two plates with one plate moving at a velocity relative to the other. The no-slip condition is enforced at both the surface and the rail, so, from the perspective of the slipper, the velocity of the air flow at the slipper is zero and the rail is moving at the velocity of the sled / freestream, pre-shock air. The shear force exerted by the moving slipper drives the behavior in the flow. [3]

Figure 22 shows a representation of the compressible Couette flow occurring at the rear of the gap. From the perspective of the slipper, the air speed at the slipper wall u_s is zero and the air speed at the rail is the relative, freestream airspeed u_∞, which is the same as the sled velocity. At the gap mid-height, the average airspeed is $u_\infty/2$. The velocity lines represent average velocities, as the flow in the gap is highly turbulent in reality. The heat fluxes in the mergence and Couette regions are only applied to the finite element model.

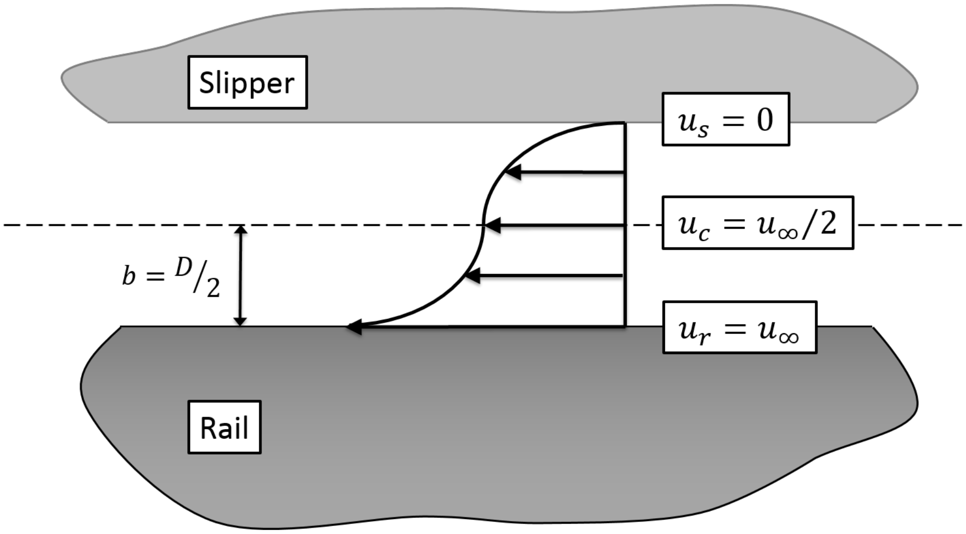

Figure 22: Couette Flow Velocity Profile.

For Couette flow, the Navier-Stokes equations (which describe unsteady, compressible, three-dimensional fluid flow) can be reduced by applying the following, [3]

$$u_y = u_z = 0 \tag{30}$$

where u_y is the vertical component of the velocity and u_z is the component of the velocity perpendicular to the of the plane of Fig. 22. The horizontal component of the flow u in the plane of Fig. 22 does not have a subscript. Couette Flow is two-dimensional ($u_z = 0$) and the average velocity of the fluid particles is zero in the vertical direction ($u_y = 0$).

The average flow velocity is moving in the horizontal direction only,

$$\frac{\partial u}{\partial x} = \frac{\partial T}{\partial x} = \frac{\partial p}{\partial x} = 0 \tag{31}$$

So, the horizontal velocity u, temperature T, and pressure p do not change in the along the Couette section of the gap at a given height. Also, Couette flow is steady, so derivatives with respect to time are equal to zero. With these in mind, Navier-Stokes equations are significantly reduced to the following,

$$\frac{\partial}{\partial y}\left(\mu \frac{\partial u}{\partial y}\right) = 0 \tag{32}$$

$$\frac{\partial p}{\partial y} = 0 \tag{33}$$

$$\frac{\partial}{\partial y}\left(k \frac{\partial T}{\partial y}\right) + \frac{\partial}{\partial y}\left(\mu u \frac{\partial u}{\partial y}\right) = 0 \tag{34}$$

Equations 32 - 34 are the governing equations for Couette Flow and apply to both incompressible and compressible cases. [3] In these equations, μ is dynamic viscosity, u is horizontal velocity, p is pressure, and k is thermal conductivity.

Again, the flow between the slipper and the rail is high speed, high temperature, compressible flow so the properties of the air are temperature dependent and, therefore, are not constant across the flow.

From Eq. 32,

$$\frac{\partial}{\partial y}\left(\mu \frac{\partial u}{\partial y}\right) = \frac{\partial \tau}{\partial y} = 0 \tag{35}$$

So, $\tau =$ constant (shear stress is constant) throughout the flow and Eq. 34 becomes,

$$\frac{\partial}{\partial y}\left(k \frac{\partial T}{\partial y}\right) + \tau \frac{\partial u}{\partial y} = 0 \tag{36}$$

Equation 36 is a non-linear differential equation and requires a numerical solution. The solution for the aerodynamic friction coefficient C_f used to determine heat flux in the

Couette flow section of the gap q_s'' has been determined by Korkegi and Briggs. [23]

$$q_s'' = C_f \rho_s u_c(\bar{h}_s - \bar{h}_b) \tag{37}$$

where ρ_s is the air density at the surface of the slipper and assumed to be the post-shock density ρ_2. The Couette velocity u_c is assumed to be 1/2 of the sled velocity because the slipper is moving at the sled velocity relative to the stationary rail and the midpoint flow will have velocity midway between the relative speeds of the slipper and the rail. The enthalpies h_s and h_b are taken at the surface of the slipper and at the midpoint of the flow, respectively. Enthalpy at the surface is found using,

$$\bar{h}_s = (c_p)_s T_s \tag{38}$$

Enthalpy at the midpoint ($b = D/2$) is,

$$\bar{h}_b = (c_p)_b T_b = (c_p)_b \frac{T_s + T_{1|2}}{2} \tag{39}$$

The specific heats c_p are evaluated using Eq 54 at the respective local temperatures: T_s is the surface temperature of the bottom surface of the slipper (calculated using the finite difference code) and $T_{1|2}$ is the temperature of the air in the gap flow away from the slipper. The 1|2 subscript indicates dependence on the existence of a shock in front of the slipper: prior to shock initiation $T_{1|2} = T_1$ and after the shock has formed $T_{1|2} = T_2$. So Eq. 37 becomes,

$$q_s'' = C_f \rho_s \frac{u_\infty}{2} \left[(c_p)_s T_s - (c_p)_b \frac{T_s + T_{1|2}}{2} \right] \tag{40}$$

where u_∞ is the relative freestream airflow speed (from the perspective of the slipper). Again, the Couette heat flux is applied to the finite element model only. The heat flux in Eq. 40 is calculated for all time steps when the slipper is not in contact with the rail and is applied to the rear-most section (away from the leading edge) of the bottom of the slipper. The Korkegi and Briggs [23] result for the wall friction coefficient is presented in Section 4.4.2.

3.6 Heat Transfer

The one-dimensional finite difference model used in previous research produced reasonable melt wear results, but opportunities existed for improvement in the implementation of the code. The simplifying assumptions that had been made regarding flow conditions were not reasonable. Specifically, during bounce, convective heat loss was assumed from the slipper bottom surface into the high-speed air traveling in the channel between the slipper and the rail. This assumption is only correct when the temperature of the air is less than the temperature of the bottom surface of the slipper. When the temperature of the air is greater than that of the bottom of the slipper, convectional heat flux will be added to the slipper, not removed. The gap temperature had been assigned a constant value of 293 K. This is the temperature of quiescent desert air and the temperature of the rail, but not of the air in the gap. Gap temperature variation is dependent on the speed of the air in the gap and the temperature of the bottom surface of the slipper.

The temperatures on the front and top of the slipper is also not constant. Determination of the film temperatures in the air surrounding the slipper is described in the following sections.

3.6.1 Total Temperature

Total temperature is used in the finite element formulation as the film temperature on the front surface of the slipper.

The energy composition of any air flow consists of both thermal and mechanical energy. If an air flow is brought to rest adiabatically, all of the mechanical energy in the flow is transformed into thermal energy and the temperature of the air increases. This new, elevated temperature is the total (or stagnation) temperature T_{T} and is defined as [4],

$$T_{\mathrm{T}} = T_{1|2}\left(1 + \frac{\gamma - 1}{2} M_{1|2}^{2}\right) \tag{41}$$

From the perspective of the slipper, the airflow is moving at the speed of the sled prior to shock initiation (Mach number < 1) and at post-shock speed (u_2 in Eq. 21) and Mach number (M_2 in Eq. 19) after the shock forms. The front face of the slipper is always perpendicular to the air flow. Air particles in the slipper path will impact the slipper face and the impact region will see a total temperature increase as Eq. 41. The total temperature and heat transfer coefficient h (determination of which is described in Section 3.6.3) are employed to apply a Robin boundary condition (film condition) on the front face of the finite element model of the slipper.

$$q'' = h(T_{\mathrm{T}} - T_{\mathrm{s}}) = -k_{\mathrm{VM}} \frac{\partial T}{\partial x}\bigg|_{\mathrm{s}} \tag{42}$$

where T_s is the temperature at the surface of the slipper, k is the thermal conductivity of the slipper (indicated by the VM subscript), and x is the horizontal direction into the slipper from the front surface.

3.6.2 Adiabatic Wall

For the heat transfer evaluation of the upper and lower surfaces of the slipper, a similar concept to that of the total temperature is employed. From Kays and Crawford, "If the free-stream velocity is large, there will be large velocity gradients within the boundary layer and a substantial conversion of mechanical energy to thermal energy by viscous shear within the boundary layer." [21] Even if the body is insulated ($q''_s = 0$), viscous heating will generate a thermal boundary layer. The film temperature under these conditions is the adiabatic wall temperature. For high-speed, turbulent flow, the adiabatic wall temperature T_{aw} is defined as [21],

$$T_{\mathrm{aw}} = T_{1|2}\left(1 + \frac{\gamma - 1}{2} Pr^{1/3} M_{1|2}^2\right) \tag{43}$$

The Prandtl number is a dimensionless parameter defined as the ratio of a material's kinematic viscosity ν and its thermal diffusivity α or $Pr \equiv \nu/\alpha$. For air, the Prandtl number is approximately 0.7 and has been assumed to be constant for this research.

The adiabatic wall temperature and heat transfer coefficient h (determination of which is described in 3.6.3) are employed to apply a Robin boundary condition (film condition) on the top face of the finite element model of the slipper and are used to determine convective heat flux in the boundary layer section of the lower surface of the slipper. Heat flux q'' in these regions is described by the following relation,

$$q'' = h(T_{\mathrm{aw}} - T_{\mathrm{s}}) = -k_{\mathrm{VM}} \frac{\partial T}{\partial y}\bigg|_{\mathrm{s}} \tag{44}$$

where y is the vertical direction into the slipper from the horizontal surface (top or bottom), as appropriate. Equation 44 describes the convective heat transfer effects seen in the boundary layer region of the bottom of surface of the slipper when the slipper is not in contact with the rail and on the top surface of the slipper for the duration of the run.

Figure 95 shows temperature variation over the course of the sled's run. Film temperatures at the slipper surfaces (total and adiabatic wall) are higher than the freestream / post-shock temperature due to the kinetic to thermal energy conversion described above in Eq. 41 and Eq. 43. The total and adiabatic temperatures differ slightly due to the $Pr^{1/3}$ term in Eq. 43. The total temperature is slightly greater than the adiabatic wall temperature at each point in time. Again, the ambient air temperature is assumed constant, $T_1 = 293$ K. Variation of post-shock temperature T_2, total temperature, and adiabatic wall temperature over the course of the run is shown in Fig. 95 in Appendix 1.

3.6.3 Heat Transfer Coefficients

This section describes the rationale and methodology used to determine appropriate heat transfer coefficients.

Heat is either imparted to or removed from the slipper depending on the temperature difference between of the air flow and the slipper and the magnitude of the heat transfer coefficient (as in Eq. 13). The convective heat transfer coefficient h describes the rate at which heat moves from surface to a fluid. From Welty, Wicks, and Wilson, "The determination of the coefficient h is, however, not at all a simple undertaking. It is related to the mechanism of the fluid flow, the properties of the fluid, and the geometry of the specific system of interest."[35] In order to characterize convective heat flux along the surfaces of the slipper, appropriate values for the convection coefficient must be determined.

The Nusselt number Nu is the dimensionless temperature gradient at the surface (Eq. 45). [17] Defining the Nusselt number for a given interaction provides a relationship between the heat transfer coefficient and the thermal conductivity k of the fluid.

$$\mathrm{Nu} \equiv \frac{hL}{k} \tag{45}$$

where L is the length of the interaction between the surface and the flow.

For the establishment of heat transfer coefficients, the top and bottom surfaces of the slipper are viewed as flat plates in high speed flow. The local Nusselt number for flow over a flat plate is given by,

$$Nu_x = 0.0296 Re_x^{4/5} Pr^{1/3} \tag{46}$$

where the subscript x is used to indicate a horizontal location on the surface. Combining Eq. 45 and Eq. 46 leads to the following expression for the local, convective heat transfer coefficient,

$$h_x = \frac{0.0296 k Re_x^{4/5} Pr^{1/3}}{x} \tag{47}$$

The local heat transfer coefficient varies from a maximum value at the front of the slipper to a minimum value at the rear as a function of $x^{-1/5}$, due to the x dependence in the $Re^{4/5}$ term in the numerator and the x term in the denominator. To simplify calculations, the mean value of the heat transfer coefficient is calculated. The mean value of $x^{-1/5}$ occurs at a location approximately $x/L = 0.42$ of the slipper length from the leading edge of the slipper. The mean value for the calculated heat transfer coefficient is then scaled and applied to segments of the top and bottom surfaces in the finite element model. Segmental variation of the heat transfer coefficient and application to the models is described further in Section 4.4.3.

The front of the slipper is approximated as cylinder in cross-flow. The Frössling number Fr is introduced to relate heat flux properties to flow field conditions through the following relationship,

$$Fr \equiv \frac{Nu_D}{\sqrt{Re_H}} \tag{48}$$

For a circular cylinder in cross flow, the Frössling number is [33],

$$Fr = 1.15 Pr^{0.4} \tag{49}$$

For air with $Pr = 0.7$, the Frössiling number is approximately 1. So the Nusselt number is approximately equal to the square root of the Reynolds number. For the calculation of the Reynolds number about a cylinder, the characteristic length is the diameter of the cylinder. When the slipper is bouncing, the flow goes over both the top and bottom of the slipper and the "cylinder" diameter is the height of the slipper. When the slipper is on the rail, the air flow is approximated as flow over one half of the "cylinder" so the characteristic length is twice the height of the slipper. When the slipper is bouncing, the heat transfer coefficient is,

$$h = k\sqrt{\frac{\rho u_{1|2}}{H\mu}} \tag{50}$$

When the slipper is on the rail,

$$h = k\sqrt{\frac{\rho u_{1|2}}{2H\mu}} \tag{51}$$

The heat transfer coefficients in Eq. 50 and 51 differ by a factor of $1/\sqrt{2}$. Less heat is transferred from the front surface of the slipper when it is on the rail as there are fewer routes of escape from the region in the front of the slipper.

Convection from the rear surface of the slipper is essentially neglected. For completeness, the rear surface film is modeled at ambient temperature ($T = 293$ K) with a heat transfer coefficient of 100 W/m^2-K.

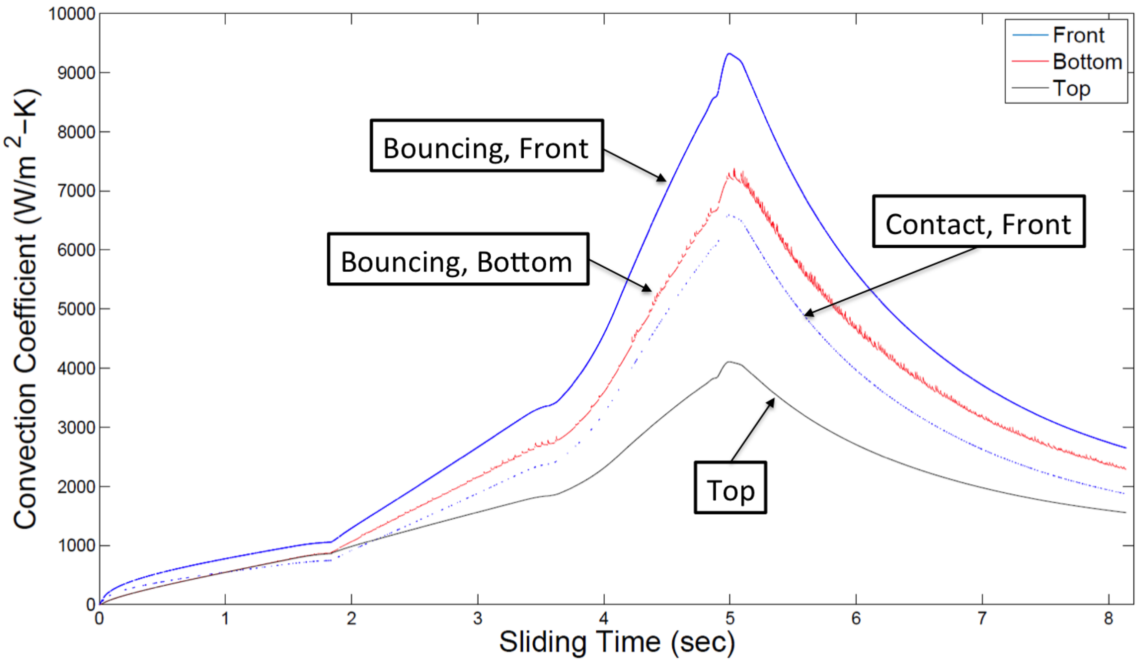

Figure 23: Convection Heat Flux Coefficients, $x/L = 0.42$.

Figure 23 shows variation of the convective heat transfer coefficients over the course of the test run. The heat transfer coefficient was calculated on the front surface using Eq. 50 and Eq. 51. The bottom and top coefficient were each calculated using Eq. 47 but the values of the heat transfer coefficient are not the same on the two surfaces due to the fact that as the bottom of the slipper slides, its temperature increases and the film temperature of the boundary layer in the gap increases. The temperature increase serves to decrease the viscosity of the air in the thermal boundary layer (as in Eq. 6). The decrease in viscosity increases the Reynolds number and thereby increases the heat transfer coefficient. The oscillations in the bottom heat transfer coefficient are due to the combination of heating and cooling of the bottom surface of the slipper. Each time the gap forms during bounce, the slipper has just been heated. During the bounce, the slipper cools and there is a corresponding increase in film layer viscosity and decrease in heat transfer coefficient. When the bottom surface is in contact with the rail, no gap exists so there is no convective heat transfer or heat transfer coefficient.

Variations also occur in the front face heat transfer coefficient and are due to the difference between the coefficient when the slipper is in contact with the rail and when it is not. The upper curve shows heat transfer coefficient at points in time where the slipper is bouncing, and the points on the lower curve are heat transfer coefficient for when the slipper is in contact with the rail.

The bottom (gap) heat transfer coefficient varies less dramatically over a small range of time steps than the front face coefficient. Local variation on the bottom is due to the temperature change of the surface due to heating of the slipper when it is in contact with the rail followed by immediate cooling of the slipper when it is bouncing.

3.6.4 Temperature Dependent Air Properties

When air temperature increases, specific heat capacity, viscosity, and thermal conductivity increase while the density and ratio of specific heats decrease. Significant temperature variation in a test run necessitates determination of air properties at each time step.

In the bottom surface boundary layer, air properties are determined at the reference temperature [21],

$$T_R = T_e + 0.05(T_s - T_e) + 0.22(T_{\text{aw}} - T_e) \tag{52}$$

In this case, T_e is the temperature at the edge of the boundary layer. So, when there is no shock, T_e is the freestream temperature ($T_e = 293K$). Following shock initiation, T_e is the post-shock temperature (T_2 in Eq. 20). Figure 24 shows the values used in Eq. 52. The adiabatic wall temperature is calculated using Eq. 43, the surface temperature is evaluated using the finite difference code described in Chapter 4.

On the top and front surfaces, where the surface temperatures are not calculated a priori, air properties are calculated at the mean value of the total temperature and the freestream / post-shock temperatures. On the top surface, air properties are determined using the mean value of the adiabatic wall temperature and the freestream / post-shock temperatures.

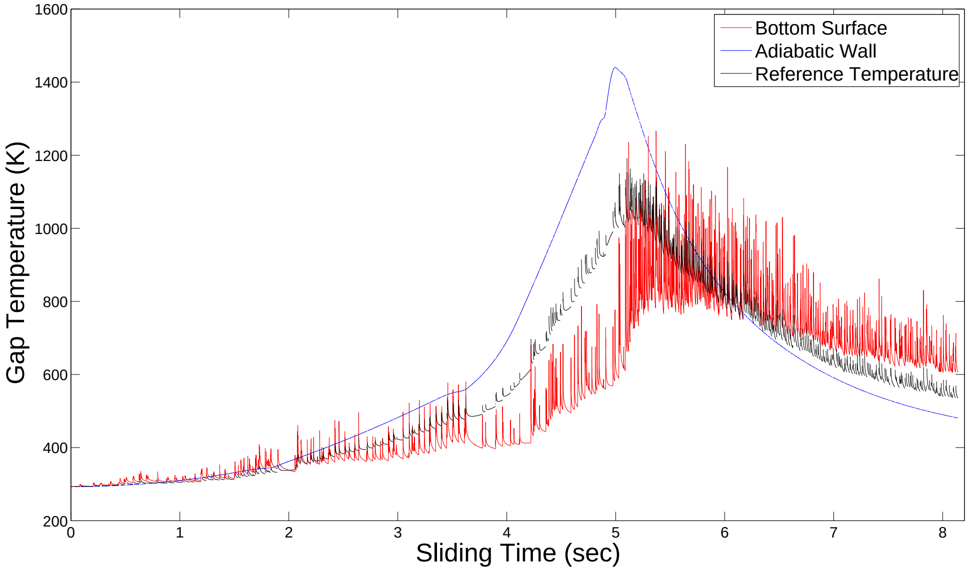

Figure 24: Gap Temperatures.

Most of the relationships describing these variations have already been introduced: viscosity varies as with Sutherland's Formula (Eq. 6), specific heat varies according to Eq. 54, and the ratio of specific as Eq. 55.

A suitable relationship for the variation of thermal conductivity with temperature could not be located so a cubic polynomial was fit to tabularized data [16],

$$k(T) = 6.5668\times10^{-12}(T-T_R)^3-3.0419\times10^{8}(T-T_R)^2+8.3012\times10^{5}(T-T_R)+0.0162 \quad (53)$$

where $T_R = 175$ K is a reference temperature employed for curve fitting accuracy. The units of thermal conductivity are W/m-K.

Air density is not recalculated from a freestream / post-shock value. Temperature gaps between the post shock temperature T_2 and the film temperatures are within 30 K to 40 K for the majority of the run (as seen in Fig. 95). This difference represents a small percentage of the absolute air temperatures. Additionally, pressure increases significantly across a shock, making precise determination of film density unfeasible. Therefore, film density is assumed to be the freestream / post-shock density. A plot of the density variation over the course of the run is shown in Appendix 1 (Fig. 96).

For low temperatures and moderate pressures, constant specific heat values may be assumed. However, at elevated temperatures, the specific heat values are dependent on temperature [8],

$$c_p = (c_p)_{\text{perf}} \left\{ 1 + \frac{(\gamma_{\text{perf}} - 1)}{\gamma_{\text{perf}}} \left[\left(\frac{\Theta}{T} \right)^2 \frac{e^{\Theta/T}}{(e^{\Theta/T} - 1)^2} \right] \right\} \tag{54}$$

Further, the ratio of specific heats (Eq. 7) is also dependent on temperature. The temperature dependence of the ratio of specific heats for air is given by the following,

$$\gamma = 1 + \frac{\gamma_{\text{perf}} - 1}{1 + (\gamma_{\text{perf}-1}) \left[\left(\frac{\Theta}{T} \right)^2 \frac{e^{\Theta/T}}{(e^{\Theta/T} - 1)^2} \right]} \tag{55}$$

where the perf subscript is used to indicate values for a calorically perfect gas. For air $(c_p)_{\text{perf}} = 1005$ J/kg-K and $\gamma_{\text{perf}} = 1.4$. The thermal constant $\Theta = 3055.56$ K.

Figure 97 in Appendix 1 illustrates the variation of the ratio of specific heats due to increased temperatures behind the shock and on the bottom slipper wall. The values are calculated using Eq. 55 with the post shock temperature T_2 and the reference temperature. Oscillations in the gap wall ratio of specific heats are due to temperature fluctuations in the gap.

3.7 Summary

This chapter described the theoretical principles required for the generation of the appropriate loads that are applied to the finite difference and finite element models.

The next chapter describes the generation of the loads in MATLAB and their application to both the finite difference and finite element models.

4 Methodology

4.1 Chapter Overview

Two mathematical modeling methods are used to simulate the heating of the slipper during a test run: a one-dimensional finite difference MATLAB code and two-dimensional finite element model in Abaqus. Previously used in research conducted by Le [26], the finite difference scheme was not altered for this research, however the material properties of both the slipper the air have been updated to reflect more reasonable values. The two-dimensional finite element model was developed specifically for this research in order to more realistically simulate aerodynamic effects (convective heating and cooling) seen on the top and front surfaces slipper during a test run. The Abaqus commercial finite element package was used for the development and implementation of the finite element model. Both models are described here.

The finite difference model can only be loaded on the bottom surface. These loads may only be applied at a single point. The finite element model, on the other hand, is loaded on the front, top, and bottom surfaces. The loads in the finite element model vary along the top and bottom surface but are constant along the front surface.

4.2 VascoMax 300 Material Description

The slipper material is VascoMax 300, an 18%-Ni maraging steel. ("Maraging" is a portmanteau of "martensitic" and "aging" - the processes by which VascoMax is formed.) Benefits to using this material are: high strength-to-weight ratio, high notched strength, as well as high impact and plane strain fracture toughness. [1] Maraging steels are used in aerospace applications, tooling and machinery, and structures. [1]

Table 2 is a listing of VascoMax 300 material properties used in both models for the present research.

Table 2: VascoMax 300 Material Properties. [1]

Property	Value
Density	8000 kg/m^3
Melt Temperature	1685 K
Latent Heat	272,000 J/kg
Thermal Conductivity	30.807 W/(m-K)
Thermal Diffusivity	858 m^2/s

The specific heat of VascoMax 300 varies with temperature; known values are shown in Table 3.

Table 3: Specific Heat of VascoMax 300 Steel. [19]

Temperature (K)	Specific Heat, c_p (J/kg-K)
298	360
422	481
598	599
700	858

4.3 DADS Data

The Dynamic Analysis and Design System (DADS) is used to model behavior of complex dynamic systems. DADS is run on a model of the HHSTT sled system prior to an actual evaluation in order to assure the system will behave within acceptable parameters. The data generated by the DADS evaluation completed prior to the January 2008 run is used as inputs to the mathematical models used in this research. Collection of real world dynamic data for a sled run is not possible in the quantity and breadth that a DADS evaluation yields. For the January 2008 test run, the DADS analysis yielded output for: horizontal velocity of the center of gravity of the sled, vertical velocity of the center of the sled, and forces between the slippers and the rails, and many others.

This research evaluates the first three stages of a four stage test run. The total duration of the three stages is 8.14 seconds. The DADS analysis yielded output at 0.2 ms intervals. Therefore, there are a total of 40,701 data points (including $t = 0$ seconds) with usable data over 40,700 time steps.

In the absence of other means of data collection, the DADS data is considered “real” sled data.

4.4 Loads and Boundary Conditions

As stated previously, the slipper will see two types of heat flux during the run. When the slipper and the rail are in contact, the friction between the two surfaces in contact generates heat. The heat dissipates into both the bottom of the slipper and the rail via conduction. When the slipper and the rail are not in contact, the effects of air flow past the bottom surface are taken into account as a convective heat flux. On the top surface and front surface of the slipper, convective heat flux is felt for the duration of the test run. The following sections discuss the generation of the heat flux loads applied in the slipper models.

4.4.1 Conduction

Conductive heat loads on the bottom surface of the slipper (Fig. 25) are far stronger than the convective heating on any face of the slipper. Although the slipper spends less time in contact with the rail than it does bouncing, the speed and downward force of the slipper acting on the rail leads to large amount of heat flux into the slipper. Conductive heating has the greatest effect on the overall temperature distribution in the slipper will be treated first.

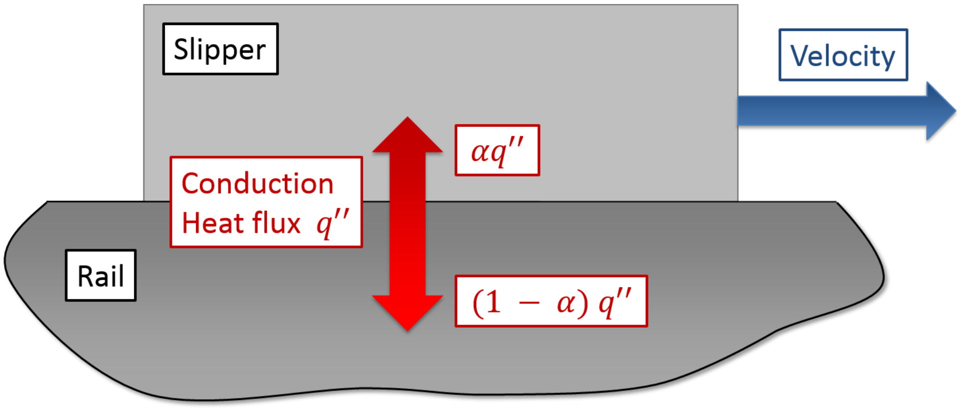

Figure 25: Conduction Loading.

Conductive heat flux is dependent on the downward force of the sled acting on the rail through the slipper, the velocity of the slipper, and the coefficient of friction between the slipper and the rail.

$$q''_{\text{slipper}}(t) = \frac{\alpha(t)F(t)v(t)\bar{\mu}(t)}{A} \tag{56}$$

where F is the downward force of the slipper acting on the rail, v is the horizontal velocity of the sled (and therefore, the slipper), $\bar{\mu}$ is the coefficient of friction between the surface of the slipper and the surface of the rail, and A is the area of contact between the two surfaces. For simplification, the contact area is assumed to be the entire bottom surface of the slipper (203.2 mm × 101.6 mm).

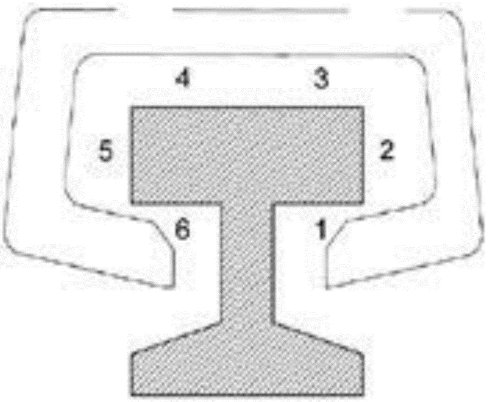

Figure 26: DADS Analysis Data Point Locations. [10]

DADS data was used for both the downward force and horizontal sled velocity. The DADS analysis provided downward force data at two points (3 and 4 in Fig. 26) for each time step. These forces act in combination so the total downward force is the sum of the forces at points 3 and 4 at each time step. The DADS horizontal velocity data is used as it was provided with no modification other than appropriate unit conversion.

Without magnification, the surface of a material may appear to be perfectly smooth to an observer. Upon closer inspection, any surface will have some degree of roughness. The relative roughness between two surfaces in sliding contact will define the coefficient of friction for their interaction.

$$\bar{\mu}(Pv) = \begin{cases} 0.2696e^{-3.409\times10^{-7}Pv} + 0.3074e^{-6.08\times10^{-9}} & \text{for } \ 0 < Pv < 4.45\times10^{8} \\ 0.02 & \text{for } \ Pv \geq 4.45\times10^{8} \end{cases} \tag{57}$$

The coefficient of friction at each time step is determined using the equation for the curve (Eq. 57, Fig. 27) established by Hale [18] using a curve fit to data generated in Montgomery's [29] research on sliding contact. As the product of the pressure and velocity increases, the friction coefficient decreases.

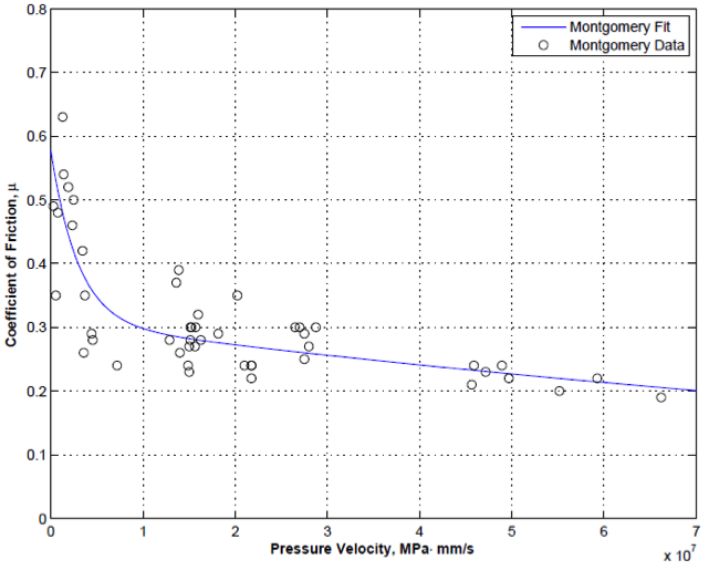

Figure 27: Montgomery Friction Coefficient Curve. [18]

Figure 28 shows the variation of the calculated friction coefficient for the test run. Maximum sled speed occurs at 5 seconds. Before 5 seconds, the sled is accelerating and lifting the slipper from the rail. When the third stage rocket disengages and the sled begins to decelerate, the sled speed decreases, but the pressure increases as the slipper is no longer feeling the same amount of lift as it had been when the rocket was engaged and the dynamic force of the sled bounces on the rails. For the remainder of the run, the slipper contacts the rail with less and less force as the friction force slows the apparatus. This decrease of the pressure-velocity product leads to larger friction coefficients as the sled comes to a stop.

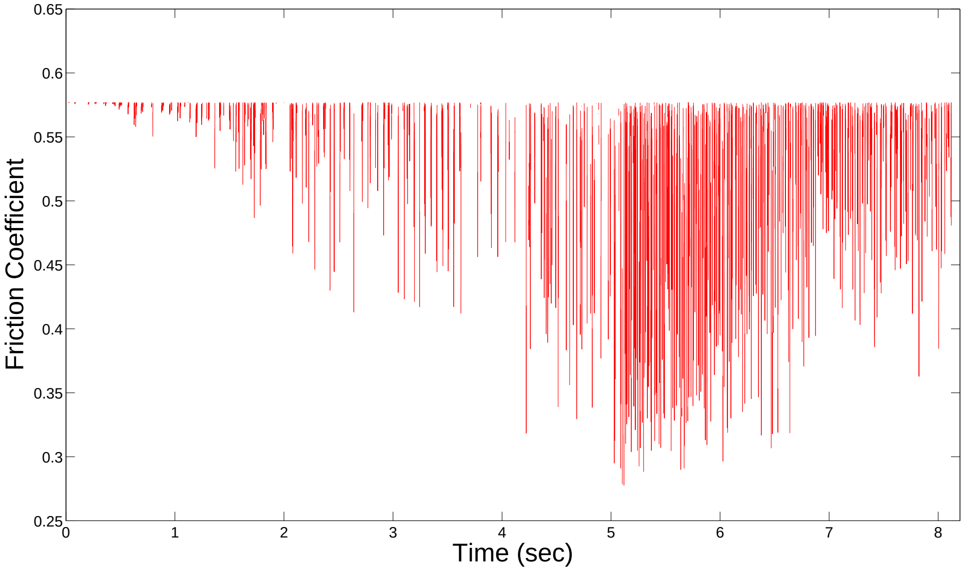

Figure 28: Calculated Friction Coefficient.

The partition function α describes the percentage of the generated frictional heat flux will be distributed to the slipper and the rail at each time step.

Heat flux into slipper,

$$q''_{\text{slipper}}(t) = \frac{\alpha(t)\bar{\mu}(t)F(t)v(t)}{A} \tag{58}$$

Heat flux into rail,

$$q''_{\text{rail}}(t) = \frac{(1-\alpha(t))\bar{\mu}(t)F(t)v(t)}{A} \tag{59}$$

Le [26] evaluated four partition functions which describe heat flux partitioning as a function of time.

The first of Le's partition functions (Eq. 60) estimates a linear decrease from the initial partitioning to the final values and is referred to as the bilinear decay function. [26]

$$\alpha(t) = \begin{cases} \alpha_0 + (\alpha_{\text{m}} - \alpha_0)\frac{t}{\text{constant}\cdot t_{\text{m}}} & t < \text{constant}\cdot t_{\text{m}} \\ \alpha_{\text{m}} & t > \text{constant}\cdot t_{\text{m}} \end{cases} \tag{60}$$

where $\alpha_0 = 0.5$ is the initial partition, $\alpha_m = 0.1$ is the partition at melt, and t_m is the estimated time to slipper melt assuming no bounce. The "constant" term is equal to the inverse of the average percentage of the slipper face assumed to be in contact with rail over the run. Le assumed an average value of 22.5% of the slipper was in contact with the rail so “constant” = 4.444. [26] The assumed slipper contact area was selected based on analysis similar to Buentello’s (discussed in Chapter 2).

Le used two expressions (developed by Paek-Spidell [30]) for estimated time to melt. The first is,

$$t_m = \frac{\pi}{k}\left(\frac{(T_m - T_0)\kappa}{2\bar{\mu}\alpha P v_0}\right) \tag{61}$$

where k is the thermal conductivity of the slipper, κ is the thermal diffusivity, $\alpha = 0.3$ is the average of α_0 and α_m, P is the average contact pressure, $\bar{\mu}$ is the coefficient of friction between the slipper and the rail, and v_0 is an assumed constant velocity.

The second expression for estimated melt time uses the solution to the following equation,

$$r^3 + \beta r - \lambda = 0 \tag{62}$$

In Eq. 62, $t_m = r^2$, $\beta = 3q_0$, and

$$\lambda = \frac{3T_m\kappa}{2\alpha P a_0}\sqrt{\frac{\pi}{k}\frac{1}{\bar{\mu}}} \tag{63}$$

where the constants are defined as above with the addition of q_0 and an assumed constant acceleration $a_0 = 305.9$ m/s^2. Equation 62 has the following exact solution,

$$r = \left(\frac{\lambda}{2}\right)^{1/3}\left[\left(\sqrt{1+N}+1\right)^{1/3} - \left(\sqrt{1+N}+1\right)^{1/3}\right] \tag{64}$$

where,

$$N = \frac{4\beta^3}{27\lambda^2} \tag{65}$$

Le used the result from Eq. 62 which yielded $t_m = 1.19$ seconds for the three partition functions in Eq. 60, 66, and 67. [26] This solution is an underprediction of the actual melt time because it does not take bounce into account.

Equations 66 - 68 are the remaining three partition functions. Equation 66 is the power function.

$$\alpha(t) = \begin{cases} \alpha_0 \left(\frac{\alpha_\mathrm{m}}{t_0}\right)^{\frac{t}{\mathrm{constant} \cdot t_\mathrm{m}}} & t < \mathrm{constant} \cdot t_\mathrm{m} \\ \alpha_\mathrm{m} & t > \mathrm{constant} \cdot t_\mathrm{m} \end{cases} \tag{66}$$

Equation 67 is the power squared partition function.

$$\alpha(t) = \begin{cases} \alpha_0 \left(\frac{\alpha_\mathrm{m}}{t_0}\right)^{\left(\frac{t}{\mathrm{constant} \cdot t_\mathrm{m}}\right)^2} & t < \mathrm{constant} \cdot t_\mathrm{m} \\ \alpha_\mathrm{m} & t > \mathrm{constant} \cdot t_\mathrm{m} \end{cases} \tag{67}$$

Equation 68 is the exponential decay function.

$$\alpha(t) = 0.4e^{-5t^2} + 0.1 \tag{68}$$

Figure 29 illustrates the decay of the four functions from the initial, equal partition to the point in the run where only 10% of the heat generated between the slipper and the rail goes to the slipper.

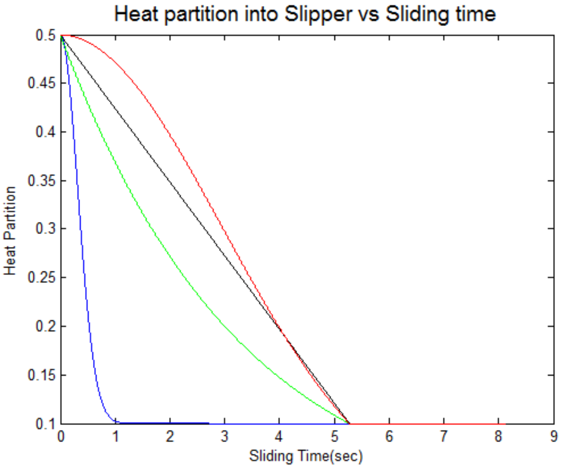

Figure 29: Partition Functions. [26]

Le [26] concluded that the exponential partition function (Eq. 29) was preferred as it led to the most reasonable prediction for melt wear volume when compared to the actual wear volume.

The conductive heat flux load felt by the slipper at each time step was calculated using the DADS force and velocity data, Montgomery's coefficient of friction function [29] applied to the DADS data, and the exponential partition (Eq. 68 described by Le [26]).

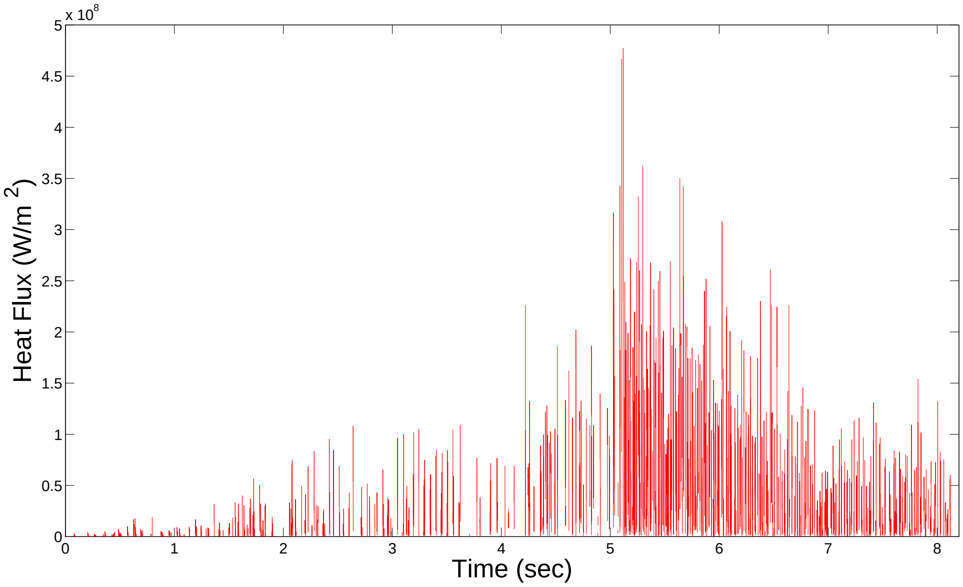

Figure 30: Conduction Heat Flux, Bottom.

Figure 30 shows the conduction heat flux generated using the exponential decay partition function (Eq. 68). The gaps in the presented data points are due to bounce; data is shown only when the slipper is in contact with the rail.

4.4.2 Convection

Convective heating occurs on the front and top surfaces of the slipper when the slipper is in contact with the rail and on all surfaces when the slipper is bouncing. Figure 31 shows the convective effects applied to the slipper sides and the quantities used employed in their application.

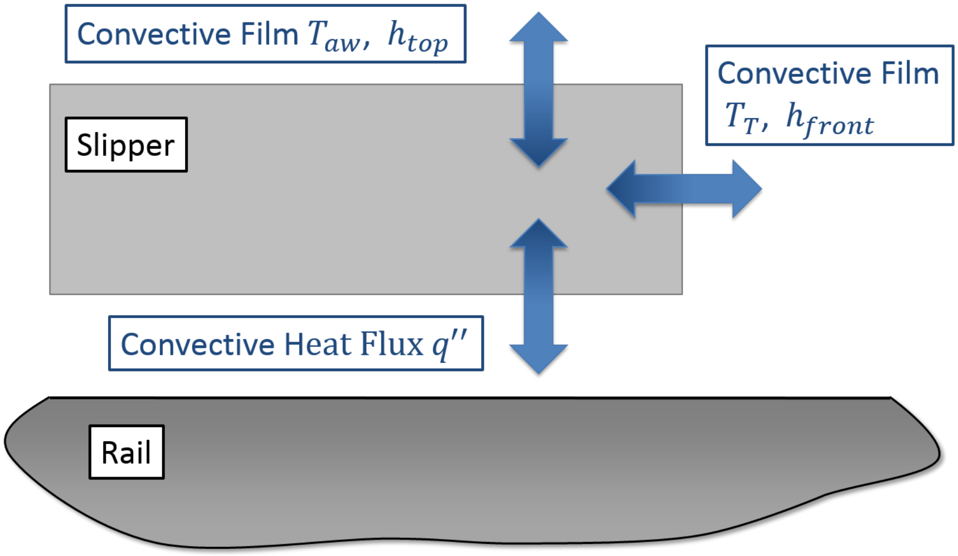

Figure 31: Bounce Loads.

Robin boundary conditions are applied to the front and top surfaces of the slipper. A Robin boundary condition is applied through the definition of a film condition. Again, Newton's Law of Cooling states,

$$q'' = h(T_f - T_s) \tag{69}$$

where T_f is the temperature of the film: the total temperature on the front of the slipper and the adiabatic wall temperature on the top. The total and adiabatic wall temperatures are calculated as described in Sections 3.6.1 and 3.6.2, respectively. Heat transfer coefficients for the front and top determined using the relationships described in Section 3.6.2. The temperature in the surface film and the heat transfer coefficient are calculated in MATLAB and assigned to the finite element model. The surface temperature is not known for the top and front faces prior to initiation of the finite element model simulation.

The film temperature and heat transfer coefficient are sufficient boundary conditions.

The temperature of the bottom surface is calculated using the finite difference solution. The bottom surface temperature is therefore assumed to be a known quantity and is used to calculate the heat flux along the bottom surface using Eq. 69. Heat flux load due to conduction (described in the previous section) and the convective heat flux are added together to generate a heat flux load which is applied to the finite element model as a Neumann boundary condition. For clarity, the convective heat flux only occurs when the slipper is bouncing and the conductive load only occurs when the slipper is in contact with the rail. There is no combination of terms; only conduction or convection occurs at a given time step.

As discussed in Section 3.4, three air flow regions exist in the gap when the slipper is bouncing as shown in Fig. 15. In the boundary layer region close to the front of the slipper, the heat flux is calculated using the adiabatic wall, surface temperature, and heat transfer coefficient to generate a heat flux in MATLAB and applied to the finite element model.

For comparison, Korkegi and Briggs [24] predicted boundary layer region gap heat flux into slipper would be [24],

$$q''_y = \frac{C_f}{2}\rho_{\mathrm{e}} u_{\mathrm{e}} \left(\frac{u_\infty^2}{2}\right) \tag{70}$$

where C_f is the coefficient of friction between the air and the slipper surface and is defined in Eq. 25 in Section 3.3.2. The Korkegi and Briggs predicted heat flux and heat flux calculated using Eq. 69 are shown plotted in Fig. 32. The horizontal black line indicates zero heat flux. Values above that line indicate convective heating of the slipper and values below indicate the slipper is being cooled by the air flow.

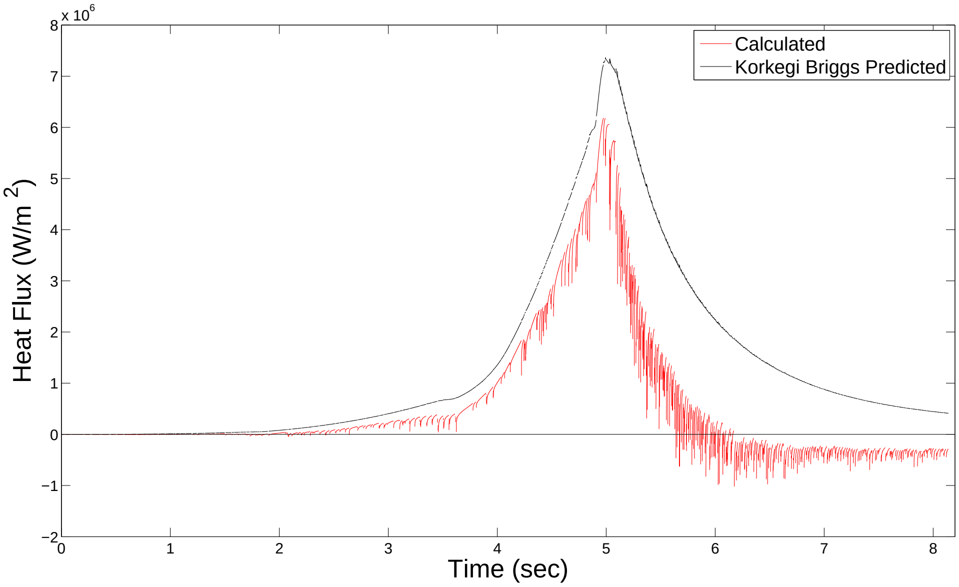

Figure 32: Boundary Layer Convection Heat Flux, Bottom.

The small variations in the Korkegi and Briggs curve result from the variations in the friction coefficient which varies with the viscosity dependence on temperature. The Korkegi and Briggs calculation assumes a cold wall so the heat flux is always into the slipper from the air (positive). The calculated values of heat flux applied to the finite element model, are based on the temperature difference between the slipper and the adiabatic wall. So, between 5.5 and 6.2 seconds, the adiabatic wall temperature transitions from being greater than the surface temperature of the slipper to being less than the temperature of the slipper. During this period, the air shifts from contributing a heating effect on the wall to cooling.

The heat flux in the Couette region is determined using Eq. 37 in Section 3.5. The Korkegi and Briggs [23] determined friction coefficients for this region are plotted in Fig. 33. For the range of Mach and Reynolds numbers seen over the duration of the test run, the friction coefficient will vary from 0.1 to 0.3. For simplification, a mid-range value of 0.2 was used for the entire run.

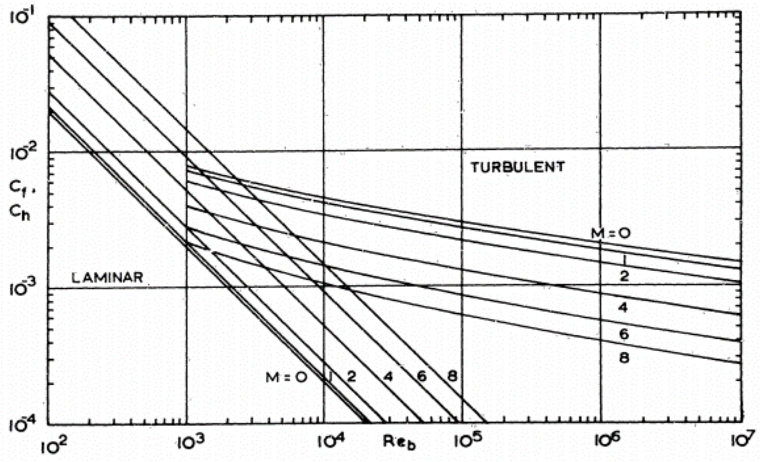

Figure 33: Friction Coefficient, Couette Flow. [23]

Heat flux in the Couette region and heat flux in the boundary layer regions are shown in Fig. 34 for comparison.

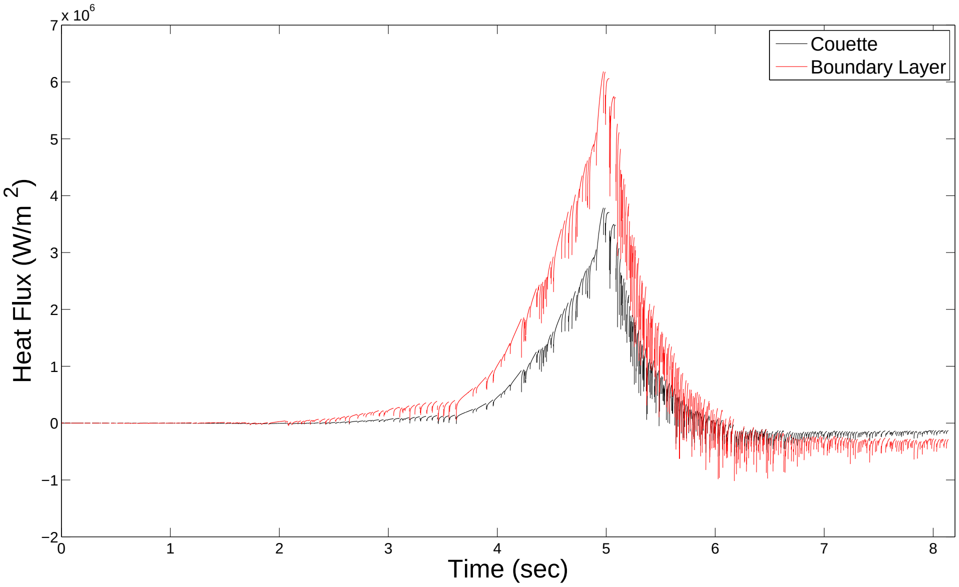

Figure 34: Gap Flow Convective Heat Flux.

The convective heat flux in the Couette region follows the same trend as the heat flux in the boundary layer region, but is smaller in magnitude.

The mergence region is the third flow region defined by Korekegi and Briggs and occurs between the point where boundary layers on the slipper and the rail combine to form a single flow state. Heat flux loads vary linearly across the transition region from the boundary layer heat flux at the front of the slipper to the Couette values at the gap exit (Fig. 34).

4.4.3 Application to Models

The total temperature, adiabatic wall temperature, heat transfer coefficients, and heat fluxes described in the preceding sections are all used to develop boundary film conditions and heat flux loads applied to the finite difference and finite element models.

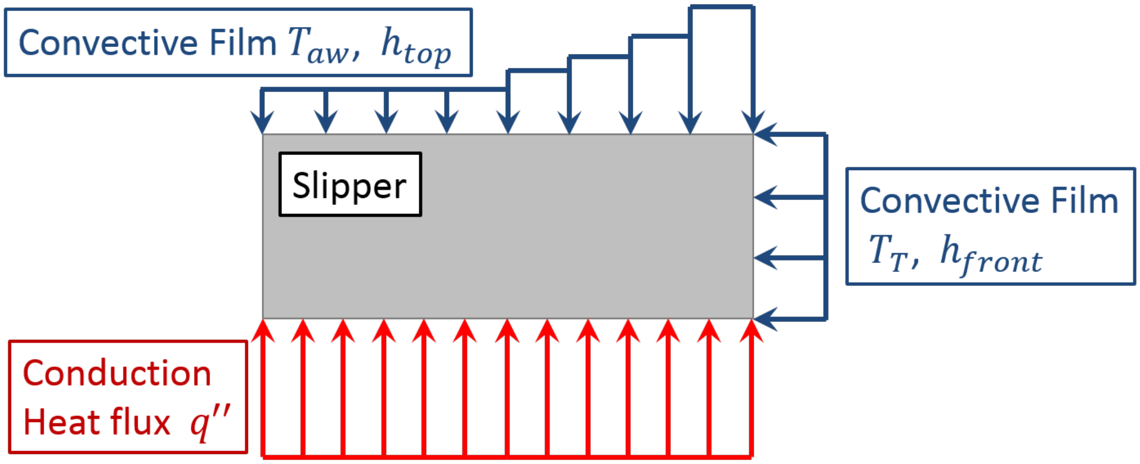

Figure 35: Contact Heat Flux and Boundary Condition Distribution.

Figure 35 shows the heat flux loads and boundary conditions as they are applied to the finite element model when the slipper is in contact with the rail. On the top surface, the adiabatic wall temperature is determined as shown in Section 3.6.2. As discussed in Section 3.6.3, the heat transfer coefficient the heat transfer coefficient varies from a maximum value at the leading edge (front surface) to a minimum at the rear. The actual application of the boundary condition on the top surface was applied in segments to simulate the $x^{-1/5}$ variation of the heat transfer coefficient, as described in Section 3.6.3. The average value of the heat transfer coefficient is determined at the point $x/L = 0.42$. The average heat transfer coefficient is then appropriately scaled for film condition application to the other regions of the top of the slipper.

The total temperature and heat transfer coefficient on the front of the slipper are described in Section 3.6.1 and Section 3.6.3, respectively. In reality, the heat transfer coefficient would vary along the front of the slipper. However, for modeling simplification the heat transfer coefficient is assumed to be constant on the front surface of the slipper. The top and front surfaces are modeled as Robin boundary conditions as the surface temperatures are not known and it is, therefore, impossible to calculate heat flux on those sides.

The conductive heat flux due to sliding friction is applied uniformly across the bottom of the slipper. Determination of the conductive heat flux on the bottom of the slipper is described in Section 4.4.1. The conductive heat flux is applied as a Neumann Boundary condition.

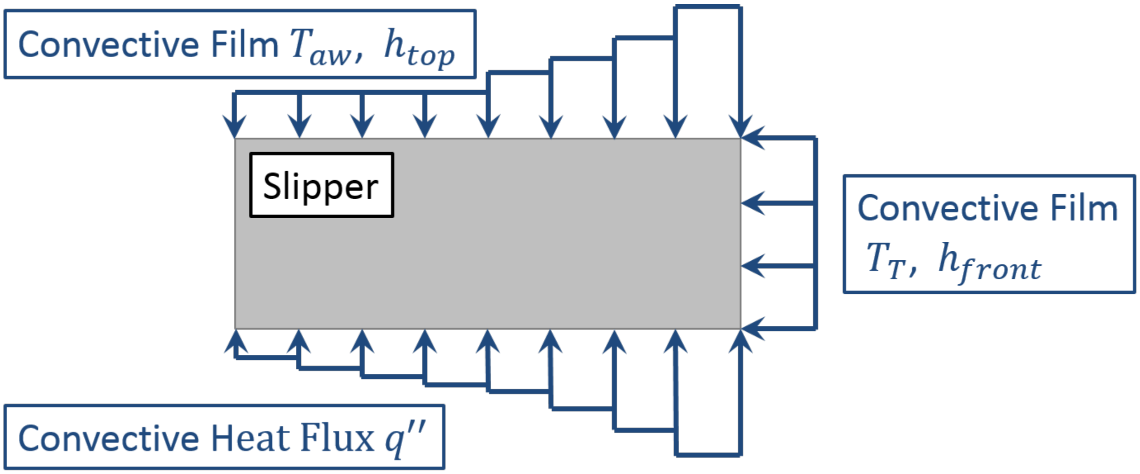

Figure 36: Bounce Heat Flux and Boundary Condition Distribution.

Figure 36 shows the heat flux loads and boundary conditions as they are applied to the slipper when the slipper is bouncing. The film conditions on the top and on the front are largely the same as they are when the slipper is in contact with the rail. The only difference is the heat transfer coefficient on the front is larger by a factor of $\sqrt{2}$, as described in Section 3.6.3.

When the slipper is bouncing, the air in the boundary layer region near the front of the slipper behaves precisely as the boundary layer on the top of the slipper. Each segment in the boundary layer region has the same heat transfer coefficient as the corresponding segment on the top of the slipper directly above.

The heat flux in the Couette region (the rear-most segment in Fig. 36) is calculated using the Couette heat flux described in Section 3.5. For the mergence region, the heat flux varies linearly (constant on the segments in Fig. 36) from the value at the rear of the boundary layer region to the heat flux value in the Couette region. For modeling simplification, the mid-point of the slipper
($x/L = 0.5$) was used as the start of the mergence region rather than the $x/L = 0.525$ location determined in Section 3.4.

The surface temperature on the bottom of the slipper is calculated using the finite difference scheme, so the convective heat flux in all three regions (boundary layer, mergence, and Couette) of the bottom of the slipper is calculated directly and applied as a Neumann boundary condition.

For the one-dimensional finite difference model, the conductive heat flux load is applied at the single point representing the bottom surface of the slipper when the slipper is in contact with the rail. When the slipper is bouncing, the film condition is modeled as a single point in the boundary layer region. The average heat transfer coefficient over the bottom surface of the plate (taken at $x/L = 0.42$) is used for this location. The front and top surfaces are not modeled in the one-dimensional finite difference model. The finite difference scheme is discussed in detail in the following section.

4.5 Finite Difference Model

In previous research, a finite difference scheme was employed to estimate melt wear and generate a one-dimensional temperature distribution. This solution estimates total melt wear and allows for examination the temperature distribution in a region near the bottom surface of the slipper. Conductive and convective heat flux is applied at the bottom of the slipper only.

4.5.1 Assumptions

A fundamental assumption in the finite difference model is that the thermal wave does not have time in the 8.14 second test run to propagate through the thickness of the slipper. A fixed diffusivity depth y^* is assumed,

$$y^* = \sqrt{\frac{t_{\text{total}} k_{\text{VM}}}{\rho_{\text{VM}} c_{p,\text{VM}}}} \tag{71}$$

The temperature at this depth is held constant at the assumed ambient temperature above the upper surface of the wall (293 K). This assumption allows for the removal of melt layer and reapplication of heat flux loading to the new bottom surface of the slipper as the melted material is removed. The formulation and execution of this methodology is described in the Formulation section.

4.5.2 Modeling Considerations

The finite difference scheme is unchanged from previous research. Refinements are made to the input air properties to include shock effects and appropriate heat transfer coefficient variation in order to generate more realistic results

4.5.3 Formulation

The one-dimensional finite difference model is limited to heat flux load application (conduction or convection) on the bottom surface only. This limitation is driven by the assumption that the temperature on the upper surface of the slipper remains constant. Although the model allows for removal of elements whose temperatures have met or exceeded the melt temperature and heat flux load reapplication to the surface node of the slipper, the temperature distribution through the thickness is limited to variation up to the diffusion depth only. Above the diffusion depth, the temperature of the slipper is assumed to be constant at the initial ambient temperature. Figure 37 is a representation of the conduction condition considered by the finite difference model.

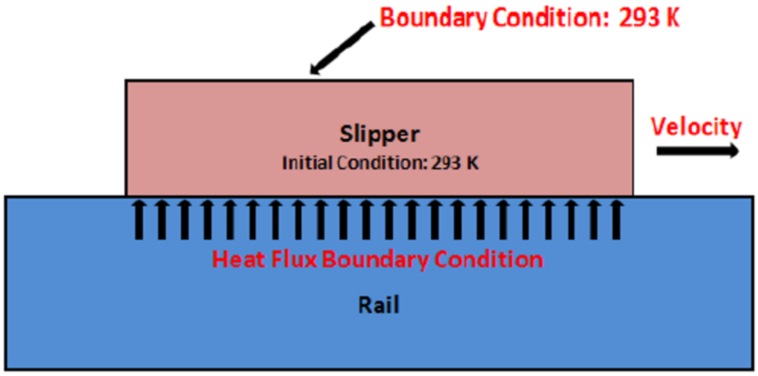

Figure 37: Slipper Rail Interface, Finite Difference Model. [26]

$$q''(t) = -k\frac{\partial T}{\partial y}\bigg|_s \tag{72}$$

Contact between the surfaces is handled by the switching function $m(t)$. The DADS force data is checked to determine contact at each time step. If the force is non-zero, the two surfaces are in contact and $m = 1$. When the force is zero, the slipper is bouncing (Fig. 5) and $m = 0$. Employing the switching function in Eq. 73 allows for a single function to describe the heat flux on the bottom surface for the duration of the run.

$$-k\frac{\partial T}{\partial y}\bigg|_s = m(t)q''(t) + [1 - m(t)]\, h(T_s - T_{1|2}) \tag{73}$$

Fourier's Law can be written as,

$$\frac{\partial T}{\partial t} = \kappa\nabla^2 T \tag{74}$$

which, for the one-dimensional analysis, reduces to,

$$\frac{\partial T}{\partial t} = \kappa\left(\frac{\partial^2 T}{\partial y^2}\right) \tag{75}$$

A central difference scheme is used to calculate the temperature at each spatial node.

$$\left(\frac{\partial^2 T}{\partial y^2}\right)_i^n = \frac{T_{i+1}^n - 2T_i^n + T_{i-1}^n}{(\Delta y)^2} \tag{76}$$

The subscript i describes the node number and the superscript n indicates the time step. The mesh consists of 100 equally spaced nodes extending vertically from the bottom surface of the slipper ($n = 1$, as represented in Fig. 38) to the diffusion length ($n = 100$).

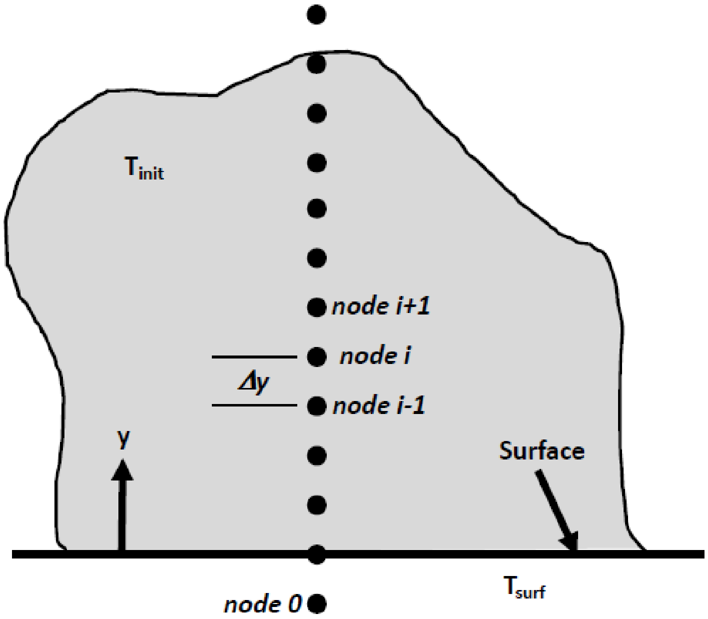

Figure 38: Spatial Discretization, Finite Difference Model. [18]

A forward difference scheme is employed to evaluate the temperature at each successive time step.

$$\left(\frac{\partial T}{\partial t}\right)_i^n = \frac{T_i^{n+1} - T_i^n}{\Delta t} \tag{77}$$

Equations 76 and 77 are combined as in Eq. 75 to solve for temperature at next increment in time.

$$T_i^{n+1} = T_i^n + \frac{k\Delta t}{(\Delta y)^2}\left(T_{i+1}^n - 2T_i^n + T_{i-1}^n\right) \tag{78}$$

As the scheme progress through time, heat propagates from the surface and the temperature increases at the nodes inside the slipper. The potential exists for the temperature in the node at the bottom of the slipper to meet or exceed the melt temperature. Paek-Spidell [30] developed a method for removal of melted material in the finite difference code. If the melt temperature is exceeded, the scheme checks the temperature at the next node. Assuming the temperature at this node has not exceeded the melt temperature, linear interpolation is conducted to estimate the point between the two nodes that would be exactly at melt temperature. Node 1 is reset at the point where the melt temperature occurs. The entire spatial grid is shifted up to account for the new location of Node 1. The difference between the new location of Node 1 and the original location of Node 1 is the melt depth. Melt can occur many times throughout the course of a run. Total melt depth is the sum of the calculated melt depths at each step. Spatial discretization does not change. The mesh always consists of 100 nodes and always has a total length equal to the initially calculated diffusivity length.

$$-k\frac{\partial T}{\partial y}\bigg|_{y=\sigma(t)} = m(t)\left(q''(t) - \rho l\frac{d\sigma}{dt}\right) + [1-m(t)]\,h(T_s - T_{1|2}) \tag{79}$$

Equation 79 is the heat flux on the bottom surface and is the same as Eq. 73 with the inclusion of the effects of latent heat and melt. The additional term in Eq. 79 includes the slipper density ρ, the latent heat l, and the melt depth σ. Figure 39 illustrates the melt layer removal in the finite difference model as time progresses.

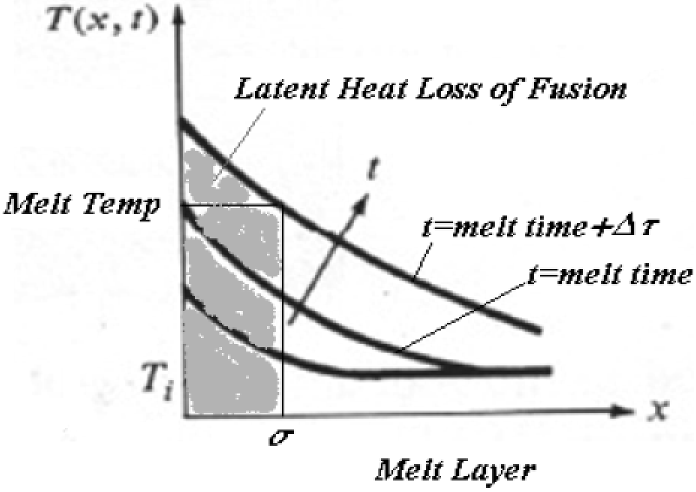

Figure 39: Melt Layer. [26]

4.6 Finite Element Model

The two-dimensional finite element model allows for loading in two dimensions. In addition to the alternating heat flux on the bottom of the slipper, friction-generated conduction and the convective heat flux, the two-dimensional finite element model allows for application of aerodynamic heating and cooling on the front and top surfaces of the slipper. The additional aerodynamic loads are not applied in the one-dimensional finite difference model.

Another motivation for the development of the two-dimensional finite element model was to enable visualization of the temperature distribution through both length and thickness of the slipper cross section. Application of heat flux load in 0.2 ms time steps leads to significant temperature variation throughout the model. Temperature contours and heat flux gradients are readily visible in Abaqus outputs.

4.6.1 Assumptions

The underlying assumptions for the finite element model were discussed in Chapter 1.

4.6.2 Formulation

The equations for finite element transfer solutions are as described by Cook, Malkus, Plesha, and Witt [14]. The two-dimensional finite element heat flux relationship (Eq. 80) is an extension of Fourier's Law (Eq. 72), used in the finite difference calculation.

$$\begin{Bmatrix} q''_x \\ q''_y \end{Bmatrix} = -\begin{bmatrix} k_x & 0 \\ 0 & k_y \end{bmatrix} \begin{Bmatrix} T_{,x} \\ T_{,y} \end{Bmatrix} \tag{80}$$

Heat flux across on a two-dimensional differential element with no internal heat generation is represented in Fig. 40, where $q''_{x,x}dx$ and $q''_{y,y}dy$ is the infinitesimal difference in heat flux across the element in the x and y directions, respectively.

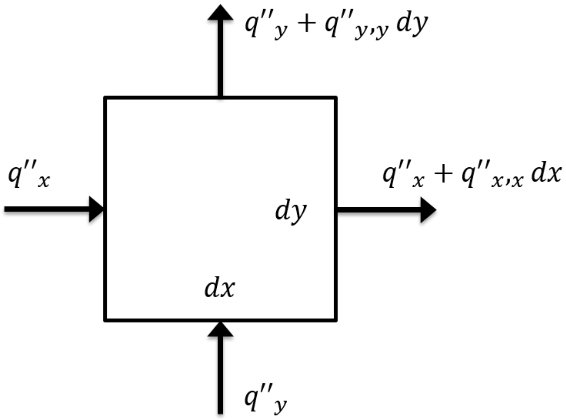

Figure 40: Differential Element.

Summing the heat flux loads into the four sides will result in stored energy $c_p\rho dxdy\dot{T}$ in the element,

$$(q''_{x,x}dx)dy + (q''_{y,y}dy)dx = -c_p\rho dxdy\dot{T} \tag{81}$$

Reducing this equation yields,

$$q''_{x,x} + q''_{y,y} = -c_p\rho\dot{T} \tag{82}$$

Combining Eq. 80 with Eq. 82 gives,

$$\frac{\partial}{\partial x}k_xT_{,x} + \frac{\partial}{\partial y}k_yT_{,y} = c_p\rho\dot{T} \tag{83}$$

which may be expressed as,

$$k\left(T_{,xx} + T_{,yy}\right) = c_p\rho\dot{T} \tag{84}$$

where $\dot{T} = \partial T/\partial t$ is the time rate of change of temperature. [14] Equation 84 is the two dimensional form of Eq. 75 used in the finite difference equation. Abaqus solves this equation for each element at each time step.

Reddy [32] describes the construction of the finite element matrices and the transition from local to global element matrices. The following finite element formulation is an adaption of Reddy's description. [32]

Temperature within in a single linear rectangular heat transfer element (shown in

Fig. 41, adapted from Reddy [32]) is defined by the following [32],

$$T(\bar{x}, \bar{y}) = \sum_{i=1}^{4} T_i^e \psi_i^e(\bar{x}, \bar{y}) \tag{85}$$

where the subscript i indicates the node number, the superscript e is the element number, and $\bar{x}$ and $\bar{y}$ are the local (elemental) horizontal and vertical coordinate axis with origin at Node 1. The dimensions of the element are $\bar{a}$ and $\bar{b}$. The geometric weighting function ψ_i^e defines value assigned to the temperature from each node [32],

$$\begin{aligned} \psi_1^e &= \left(1 - \frac{\bar{x}}{\bar{a}}\right)\left(1 - \frac{\bar{y}}{\bar{b}}\right) \\ \psi_2^e &= \frac{\bar{x}}{\bar{a}}\left(1 - \frac{\bar{y}}{\bar{b}}\right) \\ \psi_3^e &= \frac{\bar{x}}{\bar{a}}\frac{\bar{y}}{\bar{b}} \\ \psi_4^e &= \left(1 - \frac{\bar{x}}{\bar{a}}\right)\frac{\bar{y}}{\bar{b}} \end{aligned} \tag{86}$$

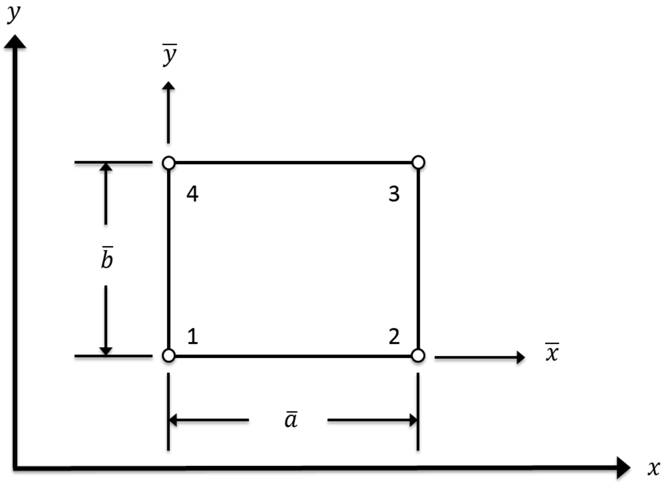

Figure 41: Single Finite Element. [32]

The conductivity coefficient matrix for an element of this type is defined as,

$$[\boldsymbol{k}^e] = k_{xx}^e[S^{11}] + k_{yy}^e[S^{22}] \tag{87}$$

where

$$[S^{11}] = \frac{1}{6}\begin{bmatrix} 2\bar{\alpha} & -2\bar{\alpha} & -\bar{\alpha} & \bar{\alpha} \\ -2\bar{\alpha} & 2\bar{\alpha} & \bar{\alpha} & -\bar{\alpha} \\ -\bar{\alpha} & \bar{\alpha} & 2\bar{\alpha} & -2\bar{\alpha} \\ \bar{\alpha} & -\bar{\alpha} & -2\bar{\alpha} & 2\bar{\alpha} \end{bmatrix} \tag{88}$$

$$[S^{22}] = \frac{1}{6}\begin{bmatrix} 2\bar{\beta} & \bar{\beta} & -\bar{\beta} & -2\bar{\beta} \\ \bar{\beta} & 2\bar{\beta} & -2\bar{\beta} & -\bar{\beta} \\ -\bar{\beta} & -2\bar{\beta} & 2\bar{\beta} & \bar{\beta} \\ -2\bar{\beta} & -\bar{\beta} & \bar{\beta} & 2\bar{\beta} \end{bmatrix} \tag{89}$$

and $\bar{\alpha} = \bar{b}/\bar{a}$ and $\bar{\beta} = \bar{a}/\bar{b}$. [32] The elemental heat flux is equally distributed at the nodes using,

$$Q_i^e = \frac{Q_e \bar{a}\bar{b}}{4} \tag{90}$$

For a single element the equations are,

$$\begin{aligned} K_{11}^1 T_1^1 + K_{12}^1 T_2^1 + K_{13}^1 T_3^1 + K_{14}^1 T_4^1 &= Q_1^1 + q_1^1 \\ K_{21}^1 T_1^1 + K_{22}^1 T_2^1 + K_{23}^1 T_3^1 + K_{24}^1 T_4^1 &= Q_2^1 + q_2^1 \\ K_{31}^1 T_1^1 + K_{32}^1 T_2^1 + K_{33}^1 T_3^1 + K_{34}^1 T_4^1 &= Q_3^1 + q_3^1 \\ K_{41}^1 T_1^1 + K_{42}^1 T_2^1 + K_{43}^1 T_3^1 + K_{44}^1 T_4^1 &= Q_4^1 + q_4^1 \end{aligned} \tag{91}$$

where Q is applied heat flux, q is internal heat flux, K is nodal conductivity, and T is nodal temperature. For example, the $K_{23}^1 T_3^1$ is the product of the effective conductivity of Node 2 acting at Node 3 (K_{23}) and the temperature at Node 3 (T_3) in Element 1 (superscript 1). [32] Incorporating the single element in Fig. 41 to the global element matrix is accomplished by the adding the appropriate nodal contributions at intersecting nodes of adjacent elements. Figure 42 shows two representative adjacent elements.

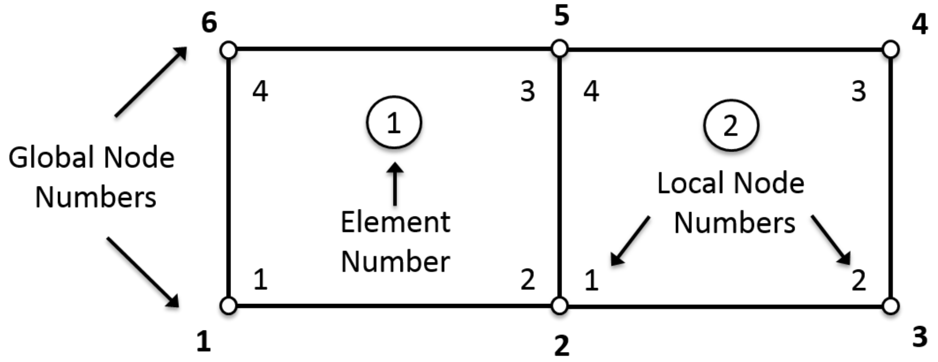

Figure 42: Global Finite Element Construction.

Combining the local contributions from Elements 1 and 2 (in Eq. 91) yields the following at global Node 2,

$$\begin{aligned} &(K^1_{21}T^1_1 + K^1_{22}T^1_2 + K^1_{23}T^1_3 + K^1_{24}T^1_4) \\ +\ &(K^2_{11}T^2_1 + K^2_{12}T^2_2 + K^2_{13}T^2_3 + K^2_{14}T^2_4) \\ &= (Q^1_2 + q^1_2) + (Q^2_1 + q^2_1) \end{aligned} \tag{92}$$

and at global Node 5,

$$\begin{aligned} &(K^1_{31}T^1_1 + K^1_{32}T^1_2 + K^1_{33}T^1_3 + K^1_{34}T^1_4) \\ +\ &(K^2_{41}T^2_1 + K^2_{42}T^2_2 + K^2_{43}T^2_3 + K^2_{44}T^1_4) \\ &= Q^1_3 + q^1_3 + Q^2_4 + q^2_4 \end{aligned} \tag{93}$$

The finite element heat transfer problem is formulated as a plane quasiharmonic. [14] The solution is obtained using the Galerkin method. The finite element functional Π for heat transfer may be written as [14],

$$\Pi = \int \left(\frac{1}{2} \{\boldsymbol{T}_\partial\}[\boldsymbol{\kappa}]\{\boldsymbol{T}_\partial\} + c\rho T\dot{T} \right) dV - \int \left(q_b T + hT_{\text{film}}T - \frac{1}{2}hT^2 \right) dS \tag{94}$$

For a single element, Eq. 94 becomes the following,

$$\Pi_e = \frac{1}{2}\{\boldsymbol{T}_e\}^T\left([\boldsymbol{k}] + [\boldsymbol{h}]\right)\{\boldsymbol{T}_e\} + \{\boldsymbol{T}_e\}^T\left([\boldsymbol{c}_p]\{\dot{\boldsymbol{T}}_e\} - \{\boldsymbol{f}_B\} - \{\boldsymbol{f}_h\}\right) \tag{95}$$

where $\{\boldsymbol{T_e}\}$ is the nodal temperatures of the element. The elemental thermal conductivity matrix $[\boldsymbol{k}]$ is,

$$[\boldsymbol{k}] = \int [\boldsymbol{B}]^T [\boldsymbol{\kappa}][\boldsymbol{B}] dV \tag{96}$$

where $[\boldsymbol{B}]$ is the derivative of the finite element shape function $\lfloor \boldsymbol{N} \rfloor$,

$$[\boldsymbol{B}] = \{\boldsymbol{\partial}\} \lfloor \boldsymbol{N} \rfloor \tag{97}$$

The shape function is defined as,

$$\lfloor \boldsymbol{N} \rfloor \begin{bmatrix} N_1 & 0 & N_2 & 0 & N_3 & 0 & N_4 & 0 \\ 0 & N_1 & 0 & N_2 & 0 & N_3 & 0 & N_4 \end{bmatrix} \tag{98}$$

which as the following elements,

$$\begin{aligned} N_1 &= \frac{1}{4}(1-\xi)(1-\eta) \quad & N_2 &= \frac{1}{4}(1-\xi)(1-\eta) \\ N_3 &= \frac{1}{4}(1+\xi)(1+\eta) \quad & N_4 &= \frac{1}{4}(1-\xi)(1-\eta) \end{aligned} \tag{99}$$

The shape functions are used to interpolate the temperature field. [14]

The remaining terms in Eq. 95 are the convection heat transfer coefficient $[\boldsymbol{h}]$,

$$[\boldsymbol{h}] = \int [\boldsymbol{N}]^T [\boldsymbol{N}] h dS \tag{100}$$

Specific heat $[\boldsymbol{c_p}]$,

$$[\boldsymbol{c_p}] = \int [\boldsymbol{N}]^T [\boldsymbol{N}] c_p \rho dV \tag{101}$$

Heat flux vector $\{\boldsymbol{f}_B\}$,

$$\{\boldsymbol{f}_B\} = \int \lfloor \boldsymbol{N} \rfloor^T q_b dS \tag{102}$$

And boundary convection vector $\{\boldsymbol{f}_h\}$

$$\{\boldsymbol{f}_h\} = \int \lfloor \boldsymbol{N} \rfloor^T h T_{\text{film}} dS \tag{103}$$

The elemental components (indicated by the lower case letters in the matrix handles) of Eq. 95 are combined to form the global matrix for the model,

$$[\boldsymbol{C}]\{\dot{\boldsymbol{T}}\} + [\boldsymbol{K}_T]\{\boldsymbol{T}\} = \{\boldsymbol{F}_T\} \tag{104}$$

where,

$$[\boldsymbol{K}_T] = [\boldsymbol{K}] + [\boldsymbol{H}] \tag{105}$$

and,

$$\{\boldsymbol{F}_T\} = \{\boldsymbol{F}_B\} + \{\boldsymbol{F}_h\} \tag{106}$$

Capital letters are used to indicate global matrices.

The time dependence in this problem (due to the variation of heat flux load inputs at each 0.2 ms time step) necessitates solution of a system of ordinary differential equations of the form,

$$\boldsymbol{T}_{n+1} = \boldsymbol{T}_n + \Delta t[(1-\bar{\alpha})\dot{\boldsymbol{T}}_n + \bar{\alpha}\dot{\boldsymbol{T}}_{n+1}] \tag{107}$$

To solve the system numerically, the ordinary differential equations are transformed into algebraic expressions at time t_{n+1} of the form,

$$\hat{\boldsymbol{K}}_{n+1}\boldsymbol{T}_{n+1} = \hat{\boldsymbol{F}}_{n,n+1} \tag{108}$$

where the terms are defined as,

$$\hat{\boldsymbol{K}}_{n+1} = [\boldsymbol{C}] + \bar{\alpha}\Delta t\boldsymbol{K}_{n+1} \tag{109}$$

$$\hat{\boldsymbol{F}}_{n,n+1} = \Delta t[\bar{\alpha}\boldsymbol{F}_{n+1} + (1-\bar{\alpha})\boldsymbol{F}_n] + [\boldsymbol{C} - (1-\bar{\alpha})\Delta t\boldsymbol{K}_n]\boldsymbol{T}_n \tag{110}$$

The solution is stable for $\alpha' \geq 0.5$ and for the Galerkin scheme ($\alpha' = 2/3$) the the solution is unconditionally stable. [32] The vector $\boldsymbol{F}$ is the sum of the heat source vector $\boldsymbol{Q}^e$ and the internal flux vector $\boldsymbol{q}^e$ and is "known for both times t_n and t_{n+1}, at all nodes at which the solution is unknown (because $Q(x,y,t)$ is a known function of time and the sum of q_j^e

at these nodes is zero).” [32]

Abaqus solves this system of equations (Eq. 108 to Eq. 110) using a backward difference algorithm. [2]

$$\frac{d\bar{u}}{dt}_{t+\Delta T} = (\bar{u}_{t+\Delta t} - \bar{u}_t)\left(\frac{1}{\Delta t}\right) \tag{111}$$

Solution convergence is determined by minimization of residual internal energy $\bar{u}$ in the model.

4.6.3 Modeling Considerations

Initial output from course, uniformly meshed models showed largest temperature gradients on the bottom of the slipper. Along the bottom of the slipper, the largest temperature variations were seen at the front of the slipper. Neither of these observations are surprising. The bottom of the slipper is the area of the slipper that sees the largest heat flux magnitudes (from convection) and largest heat flux variations (rapid changes from heating to cooling). Additionally, the convection heat transfer coefficient is greatest at the leading edge of the slipper which will amplify the convective effects. Aerodynamic heating at the leading edge of the slipper leads to further increased temperatures in this region. The bottom surface close to the leading edge is also the only region of the slipper where melt occurs in the model.

Model refinement iterations naturally led to small elements along the bottom surface of the slipper with the smallest elements at the front. The goal of the refinement was to account for the large temperature gradients and to best capture size of the melt area by attempting to limit the total melt boundary to an area that stayed completely within element boundaries.

The model was generated with 4-node linear quadratic elements (DC2D4 in Abaqus). Abaqus has only four options for heat transfer elements: 3-node linear, 4-node linear, 6-node quadratic, and 8-node quadratic. When latent heat effects are present (as in the slipper melt region) first order elements are preferred. This is due to the fact that Abaqus uses a numerical integration rule that lumps specific heat terms in the element corners. As a result, the internal energy rate term of the Jacobian is diagonal. [2] The 4-node elements were selected because calculation of melt region area is simplified with quadrilateral elements.

As described previously, the loads and boundary conditions were generated externally (in MATLAB) for each time step and applied to the slipper model in Abaqus. So the finite element heat flux model does not calculate the heat flux loads resulting from the flow around the slipper. The slipper is modeled as a stationary object and the loads and boundary conditions vary with each time step to simulate the air flow variation on the surfaces due to the high speed air flow and slipper rail contact.

Abaqus considers the heat transfer elements employed to model the slipper using the Lagrangian description of temperature flow field through the model. By contrast, the external heat flux loads and boundary conditions were generated using the Eulerian method of spatial description. The loads and boundary conditions were calculated at defined points in time and Eulerian space and applied to the Lagrangian model.

An alternative method for modeling the slipper would have been to use a coupled Eulerian / Lagrangian model within Abaqus by defining the flow field external to the slipper and allowing the flow to define the boundary conditions the slipper encounters. Unfortunately, latent heat effects (and therefore melt) cannot be modeled in Abaqus using the Convective (as they are called) heat transfer elements.

The finite element model was run using four different meshes. The details for each mesh are shown in Table 4. The element dimensions listed in Table 4 are for the smallest elements located on the bottom of the slipper near the leading edge.

Table 4: Finite Element Model Specifications.

Model	Elements	Nodes	Width mm	Height mm	Area mm^2
1	41,584	42,066	0.1	0.1	0.01
2	25,600	26,000	0.1	0.2	0.02
3	17,920	18,265	0.2	0.2	0.04
4	852	936	2.12	0.98	2.074

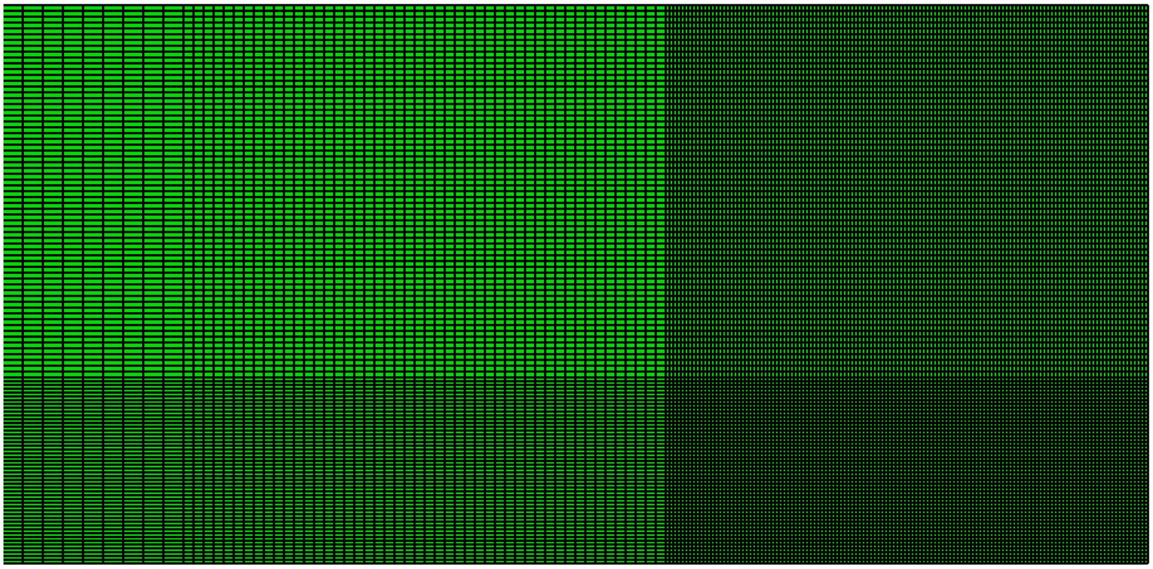

Figure 43: Finite Element Mesh, Model 1.

Figure 43 shows the area near the leading edge ($H = 14.7$ mm, $L = 30$ mm) of a representative finite element mesh (Model 1). This is the finest mesh used to model the slipper.

The finite element model in Abaqus handles latent heat differently than the finite difference code handles latent heat. When the slipper material reaches its melting temperature T_m, Abaqus increases the specific heat of the material by,

$$c_p(T) = c_p(T) + \frac{l}{T_l - T_s} \tag{112}$$

where l is the latent heat of the slipper, T_s is the solidus temperature (equal to the melt temperature of the slipper so $T_s = 1,685$ K), and T_l is the liquidus temperature $T_l = 1,715$ K. The difference between the solidus and liquidus temperature represents phase change region. Figure 44 shows a graphical depiction of how Abaqus handles the effect of latent heat.

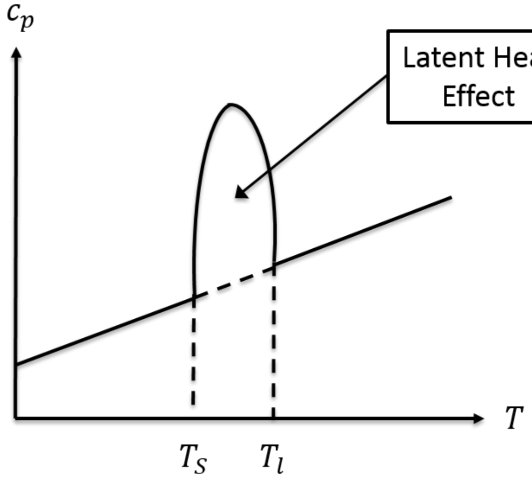

Figure 44: Latent Heat.

In raising the specific heat, the finite element model stores additional internal energy (discussed further in the next section) in this region. This area is considered the melted area of the slipper for the purposes of this research.

With respect to model convergence, the solution scheme described in Eq. 108 to Eq. 110 is linear so the solution is evaluated exactly and no iterations are required. Fig. 45 and Fig. 46 illustrate the variation in the Abaqus solutions determined using two different meshes (specifically, Model 1 and Model 4). For $t \leq 5.2$ seconds, the temperatures curves are almost identical across the two figures. After $t = 5.2$ seconds, the temperature values in the curves from Model 1 (Fig. 45) are higher than the values determined using Model 4 (Fig. 46). The difference in the temperatures in these curves is due to the fact smaller elements permit greater temperature variation in a smaller area and more closely approximate material continuum.

Nonlinearity incurred with the introduction of the latent heat effect does influence model convergence. The specific heat in the latent heat range is temperature dependent (Eq. 112) so iteration is required to determine specific heat and appropriate temperature. When refining the finite element model, the size of the latent heat range is of particular importance. The coarsest mesh (Model 4, Table 4) model converged to a solution with the appropriate 30 K phase change range (T_s = 1,685 K to T_l = 1,715 K). However, when using the finest mesh (Model 1) the model did not converge to a solution using the appropriate phase change range because the time step used (DADS time interval 0.2 ms) was too large. The solution diverged at the onset of melt at $t = 5.1$ seconds. Adjusting the phase change range to 90 K (by setting $T_l = 1{,}775$ K) lessened the influence of the elevated specific heat in this region and the solution converged. The onset of melt still occurs at $T_m = 1{,}685$K and while the temperatures seen in the melt region using Model 4 with the larger phase change range are significantly higher than the temperatures would be when using the appropriate, smaller phase change range, the energy stored in the melt region is the same.

Unfortunately, no closed form solution exists for the time dependent, slipper heating problem with phase change. Therefore, no conclusions may be drawn regarding the accuracy of the temperature values resulting from the finite element models. However, the finest mesh solution is preferred as it most closely models the continuum and instantaneous heating effects due to the rapidly changing heat flux values (particularly near the bottom surface) are more closely modeled than in the coarser mesh models. Therefore, finite element results displayed in Chapter 5 are primarily from Model 1. The exception to this is the heat flux vector plots (Section 5.3.4) which were generated using Model 4 in order to show a representative set of heat flux vectors without overwhelming the figures with vector symbols.

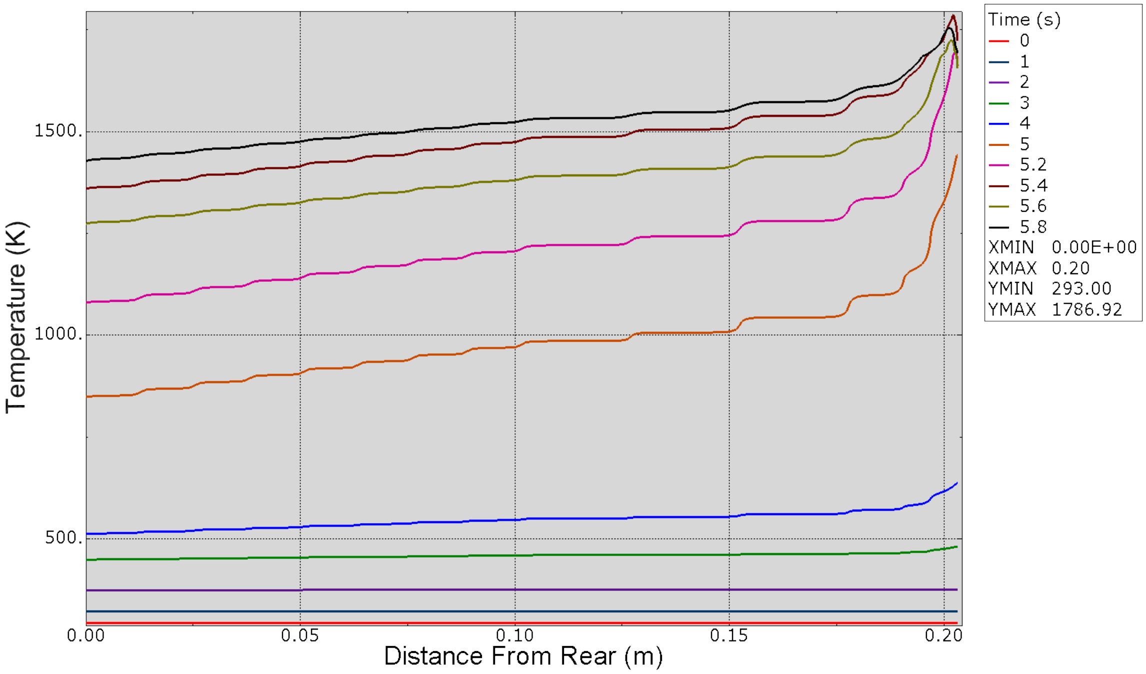

Figure 45: Model 1, Bottom Surface Temperature, $t = 0$ to 5.8 seconds.

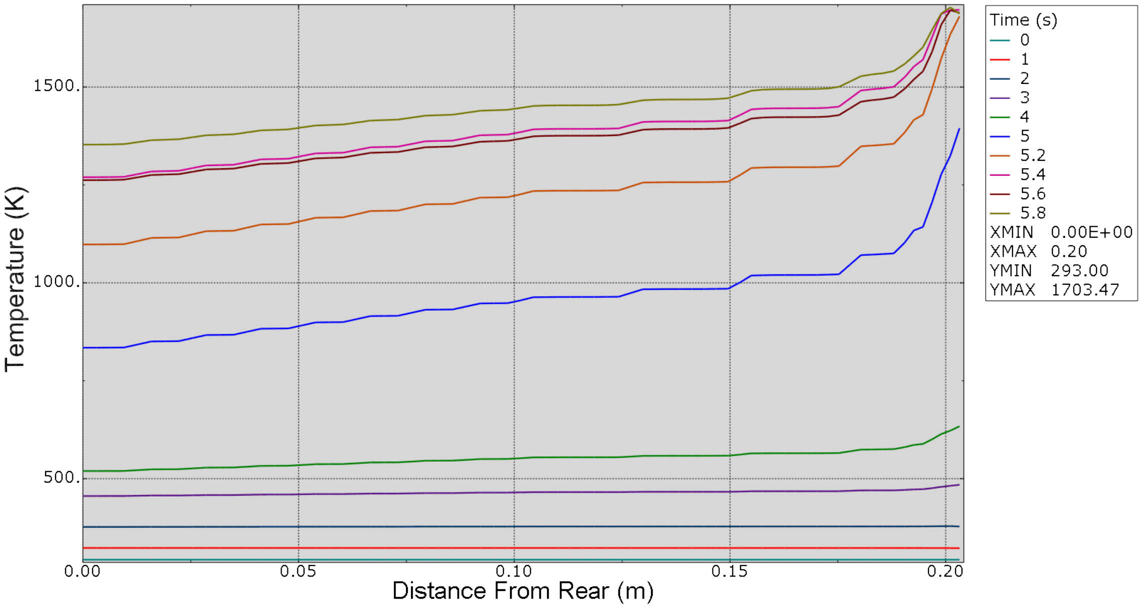

Figure 46: Model 4, Bottom Surface Temperature, $t = 0$ to 5.8 seconds.

4.7 Summary

This chapter describes load generation and application to the finite difference and finite element models. The same physical and mathematical principles are employed to solve for the temperature distribution in each model, but the solution execution is not the same. It is noteworthy that the models handle melt in very different ways.

5 Analysis and Results

5.1 Chapter Overview

This chapter presents results generated using both the finite difference and finite element models. Finite difference model generated results are limited to comparison of partition function using calculated melt wear values. The finite element results include two dimensional temperature and heat flux contour plots, and estimated melt wear.

5.2 Finite Difference Results

The finite difference model is restricted to application of conductive heat flux and convective film at a single point on the bottom surface of the rail. So the only region of the slipper considered is a portion of the thickness measured up from the bottom. The point of application may be varied to consider various convection coefficients resulting from unique gap air flow parameters at each location along the surface of the slipper.

Le [26] used the finite difference code to predict wear using four heat flux partitioning functions. Each one of the test runs assumed a 100 percent contact between the slipper and the rail and all of Le's simulations kept constant air properties. Le's melt wear results are reproduced in Table 5.

Table 5: Partion Function Predicted Wear. [26]

Parition Function	Total Melt Wear (%)
Bilinear	3.39
Power	3.61
Power Squared	2.06
Exponential Decay	0.787

With the convective heat flux refined to account for variable gap temperatures and heat transfer coefficients, the finite difference method yields zero melt when the entire slipper surface is in contact with the rail for the duration of the run. This is true for all four partition functions.

Considering again Buentello's [10] estimation of wear on segments of the slipper due to the changing orientation of the slipper (Fig. 13 on page 22), in reality, the slipper will not strike the rail with its complete surface every time it hits the rail. For each point on the horizontal axis, contact percentage is assumed constant for the entire test run. So, if "Surface Contact, %" is 40%, then the point under examination was somewhere in a region of the slipper that was 40% of the slipper area and came into contact with sled every at every possible time step at the same contact percentage.

Figures 47 to 50 were generated by varying the contact percentage to determine the amount of wear that would be predicted if the contact area was less than the full slipper area. Lower contact areas lead to more melt because the same downward force (from the DADS data) is applied over a smaller area so the pressure and therefore heat fluxes are larger than for full contact.

The melt wear results when using the exponential (Fig. 47) or bilinear partition function (Fig. 48) are almost identical.

Melt wear results from the power (Fig. 49) and power squared (Fig. 50) partition functions are greater than the results determined using the exponential and bilinear function.

The wear numbers are much less than those predicted by Le. [26] due to the use of larger values for the heat transfer coefficients and variation of air properties at elevated temperatures. A greater amount of heat is removed from the slipper in the current version of the model. The relative melt wear trends between the partition functions match those seen by Le with the exception of the bilinear function due to melt time calculation differences. Le used Eq. 62 for the melt time and Eq. 61 is used in the current research.

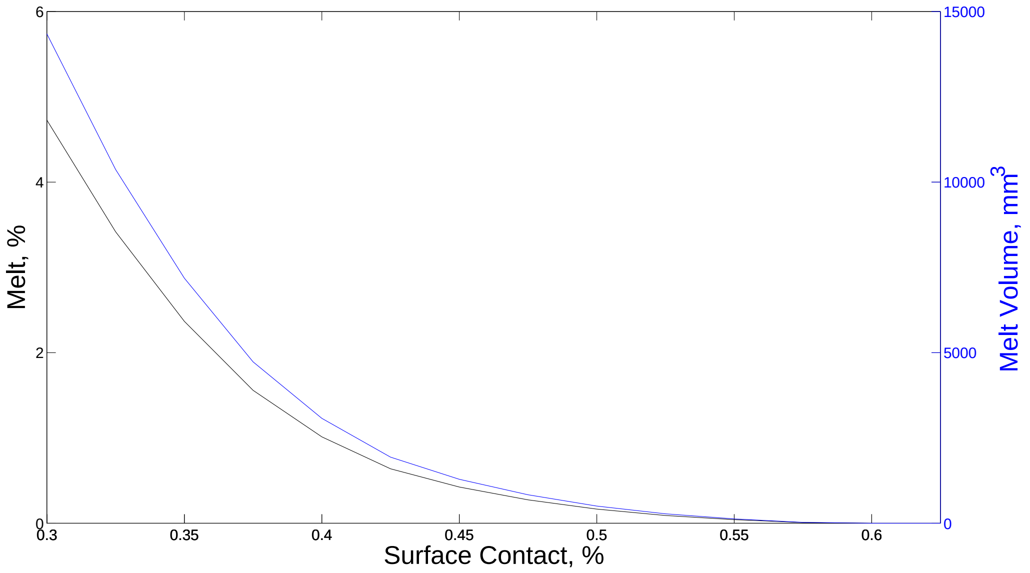

Figure 47: Melt Wear, Exponential Partition Function.

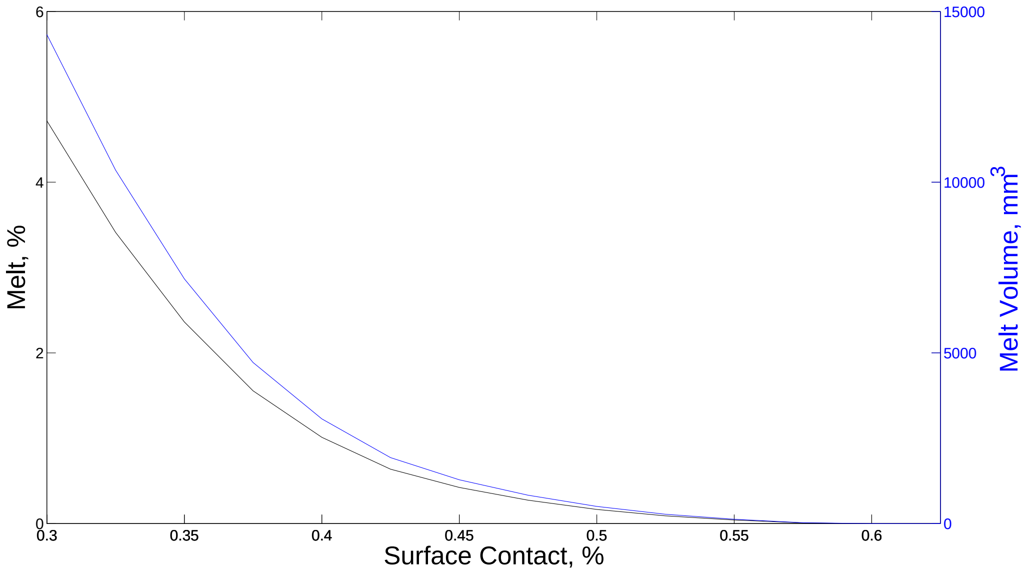

Figure 48: Melt Wear, Bilinear Partition Function.

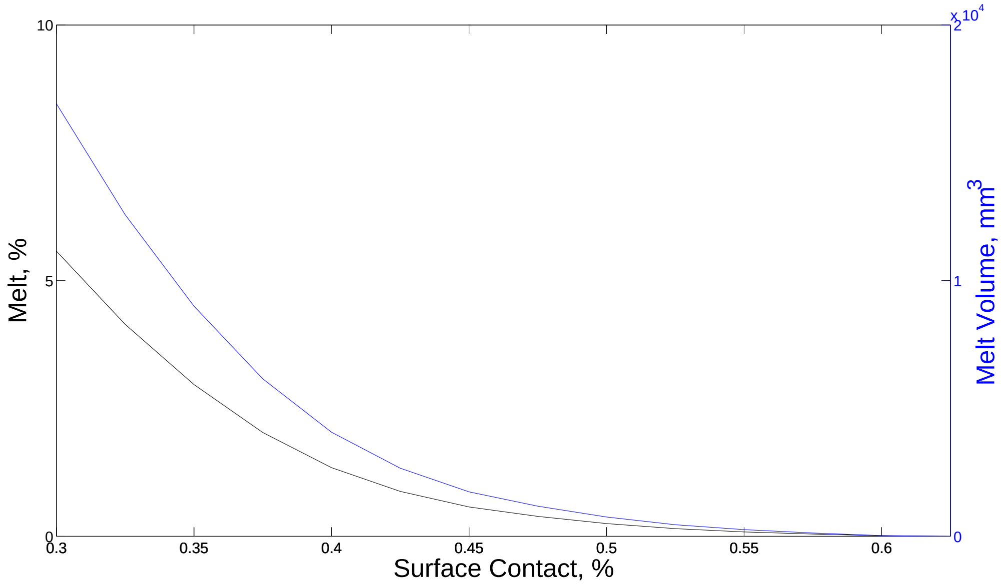

Figure 49: Melt Wear, Power Partition Function.

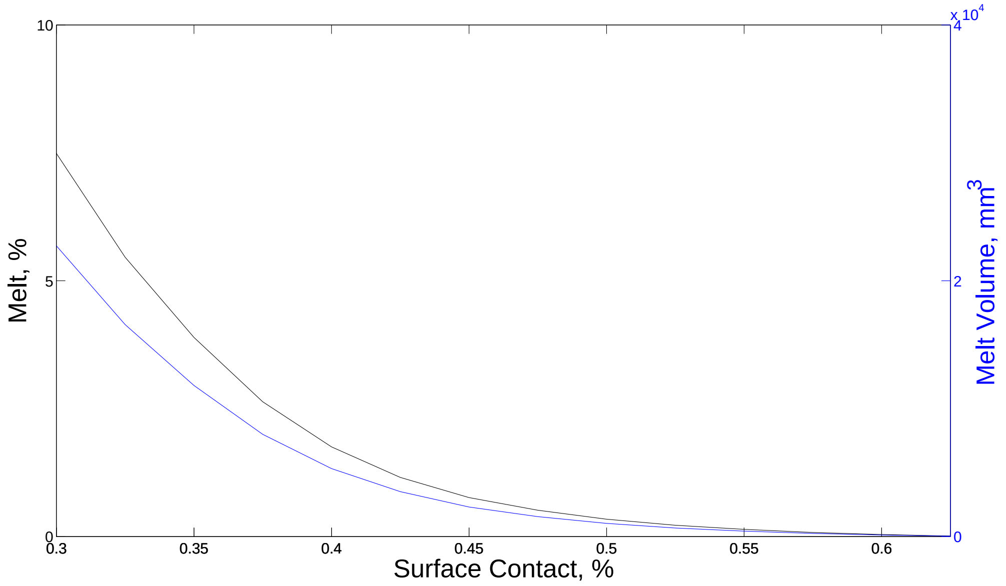

Figure 50: Melt Wear, Power Squared Partition Function.

5.3 Finite Element Results

The finite element results are presented in five sections. First, one-dimensional slipper temperature distributions on the front, top, and bottom surfaces, as well as distributions from the mid-length and mid-height cross sections are shown at selected times throughout the run. Second, two-dimensional slipper temperature contour plots are shown in between 4 seconds and 8.14 seconds (Figs. 70 to 79). In the third section, one-dimensional heat flux distributions are shown on the front, top, and bottom surfaces of the slipper at various times during the test run. Fourth, two-dimensional heat flux vector plots are presented. Between 5 seconds and 6.2 seconds, the heat flux vector plots illustrate heat flux variation during the segment of the run that sees both maximum heat flux magnitude and the transition from aerodynamic heating to cooling on the front and top of the slipper. The maximum heat flux magnitude times in the heat flux vector plots do not coincide with the maximum melt area times in the two-dimensional temperature distributions. Melt wear estimates are presented in the fifth and final finite element results section. The maximum observed slipper melt area occurs at 5.38 and 5.64 seconds.

Although the finite element model uses a 0.2 ms time step, output was written at each 20 ms increment in order to reduce processing time. Finite element results are, therefore, shown at each 20 ms increment.

5.3.1 One-Dimensional Temperature Distributions

Figures 51 and 52 show temperature distributions along the front surface of the slipper. The figures are split at $t = 5.4$ seconds to show the distributions more clearly. If the temperature distributions were shown for the duration of the run on a single figure, the plotted lines would overlap. Temperatures generally increase from $t = 0$ to $t = 5.4$ seconds and decrease thereafter.

As seen in Fig. 51, the temperature at the bottom of the slipper ($y = 0$ m) increases steadily as time progresses from the minimum 293 K at $t = 0$ seconds to a maximum value at $t = 5.4$ seconds. The maximum temperature ($T = 1{,}722.44$ K) is obviously greater than the melt temperature of the slipper ($T_m = 1{,}685$ K). This is a result of the model retaining melted material and adjusting the specific heat to include the effects of latent heat. In the melted region, the energy applied to the model as heat flux is stored and continues to raise the temperature of both the melted region and the surrounding area. In reality, the slipper would lose material and the heat flux load would be applied to the new surface created by the lost, melted slipper material.

At $t = 5.4$ seconds, the temperature in bottom section of the slipper ($y < 0.045$ m) is at a maximum, but the temperature above that point has decreased to below the values seen at $t = 5.2$ seconds. The temperature decrease in the upper section is a result of the convective aerodynamic cooling effects on the front and top of the slipper.

After $t = 5.4$ seconds (Fig. 52), the temperatures in the upper portion of the slipper ($y > 0.045$ m) continue to decrease steadily due to aerodynamic cooling. Below that point, temperatures also generally decrease as time progresses. However, temperature fluctuations are observed in the region close to the bottom surface of the slipper due to large variations in the alternating convective and conductive heat fluxes as the slipper decelerates.

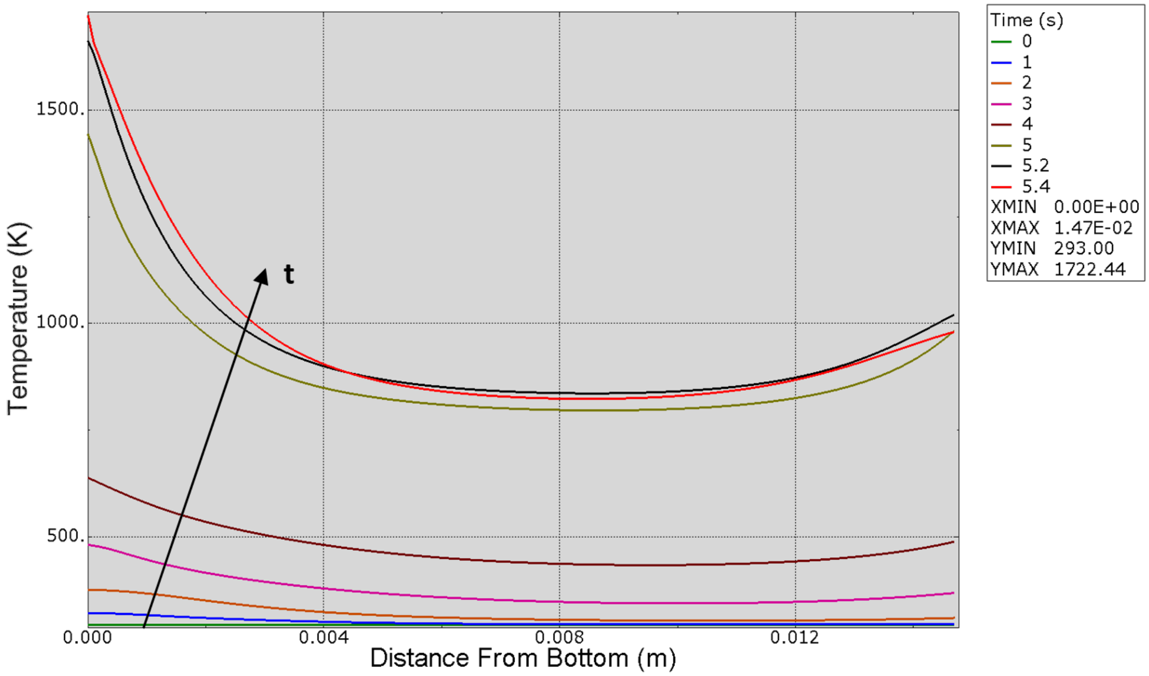

Figure 51: Front Surface Temperature, $t = 0$ to 5.4 seconds.

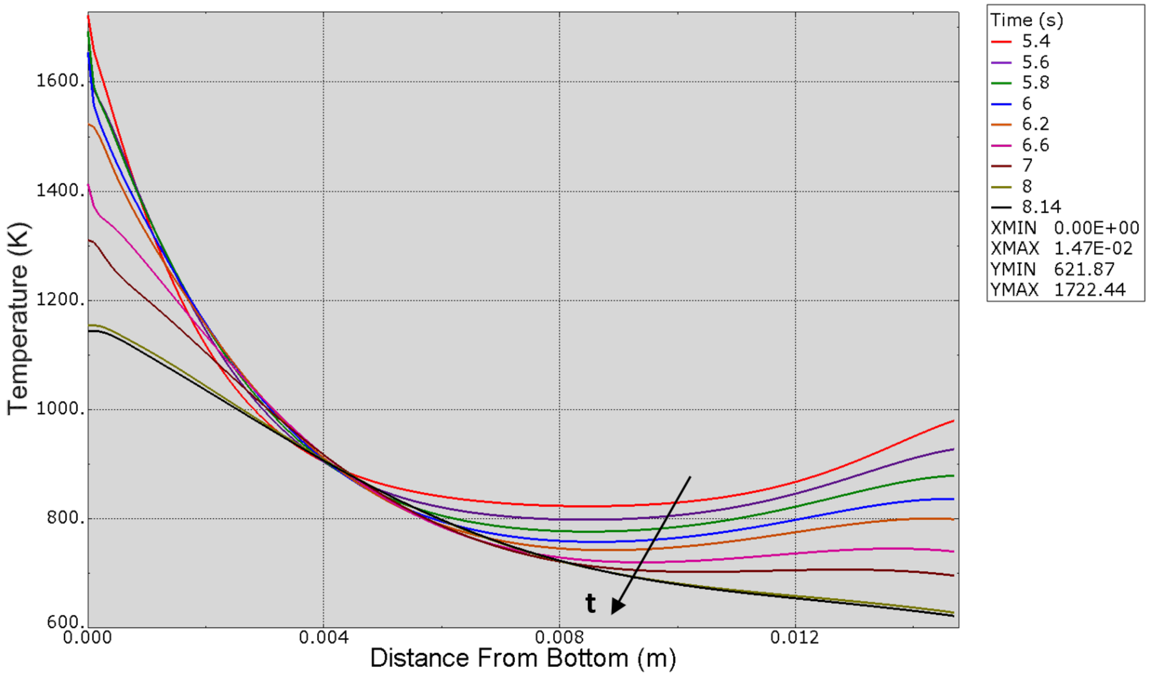

Figure 52: Front Surface Temperature, $t = 5.4$ to 8.14 seconds.

Figures 53 and 54 show temperature distributions in the vertical (y) direction at the horizontal mid-length of the slipper ($x/L = 0.5$) as time progresses through the run. As with Figs. 51 and 52, Figs. 53 and 54 are split to show temperature distributions for times before and after $t = 5.4$ seconds to avoid overlapping lines.

Figure 53 shows temperatures increasing at all points along the slipper cross section as time progresses. The greatest temperature increases are seen at the bottom of the slipper as a result of the conductive heating from the slipper / rail contact. Temperature increase at the top of the slipper is due to convective aerodynamic heating. At $t = 5.4$ seconds, the temperature on the top has not increased beyond the value seen at $t = 5.2$ seconds. This is a result of the reversal of the convective aerodynamic effects from heating to cooling on the top surface.

After $t = 5.4$ seconds (Fig. 54), the temperatures decrease near the top and bottom surfaces of the slipper, but increase in the middle. The temperature increase in the middle section of the slipper is due to the propagation of the thermal wave resulting from the conductive frictional heat flux acting on the bottom of the slipper.

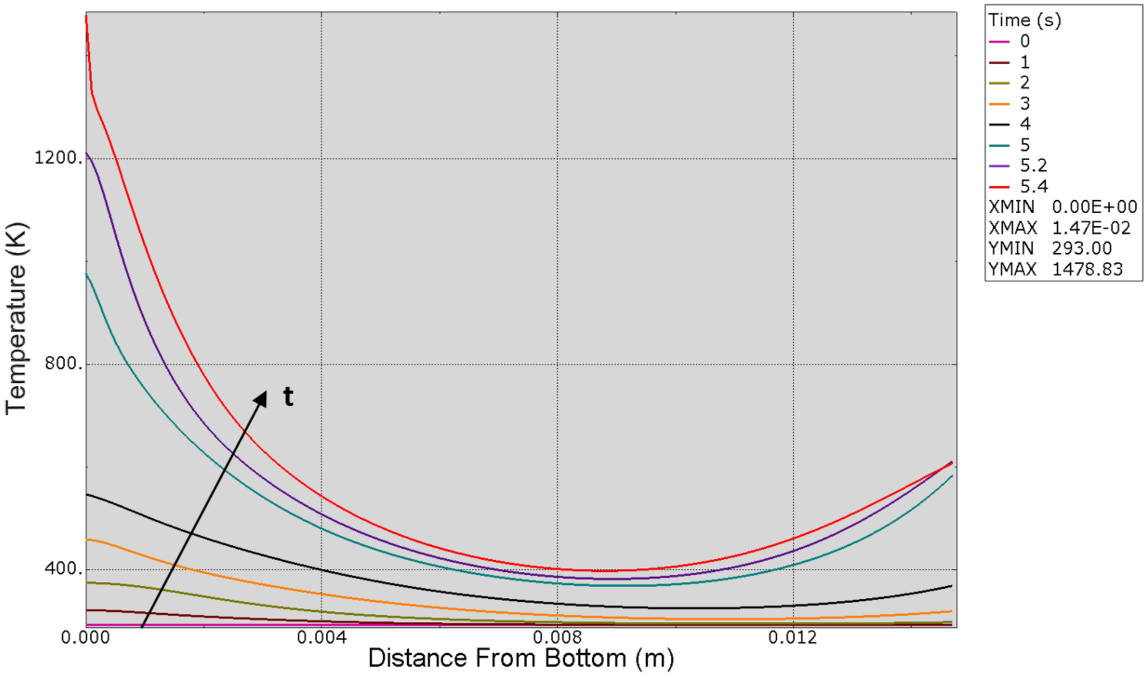

Figure 53: Mid-length ($x/L = 0.5$) Temperature, $t = 0$ to 5.4 seconds.

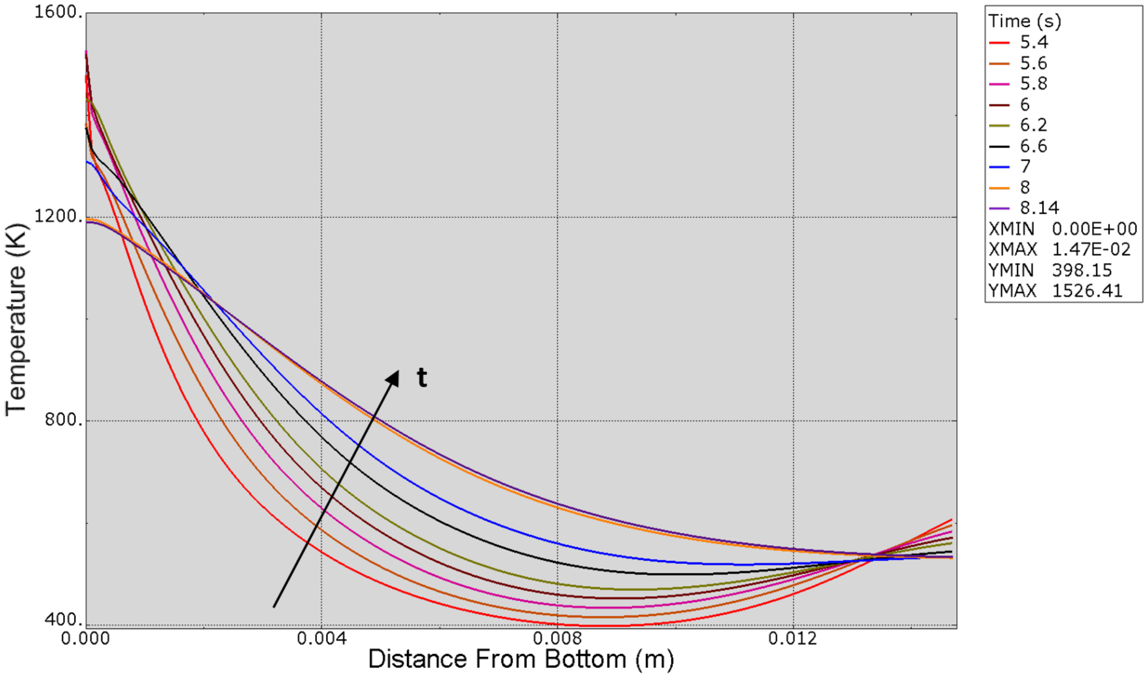

Figure 54: Mid-length ($x/L = 0.5$) Temperature, $t = 5.4$ to 8.14 seconds.

Figures 55 to 60 show horizontal temperature distributions along the bottom surface, at the mid-height ($y/L = 0.5$), and along the top surface of the slipper. Again, at each location, the curves are split to show distributions that are generally increasing then decreasing with time to avoid overlap.

In the bottom surface temperature distribution curves of Figs. 55 and 56, the conductive heat flux load is applied uniformly across the bottom surface, so the temperature variation seen along each curve is a result of the convective effects on the bottom and front surfaces of the slipper. First, convective heating along the bottom surface varies from maximum at the front (boundary layer region) to a minimum at the rear (Couette region). Second, convective heating at the front further increases the temperature on the bottom of the slipper near the leading edge. The stepping variation along each curve is due to the segmentally applied convective loading.

The curves in Fig. 55 show temperature increasing with time along the bottom surface from $t = 0$ to 5.4 seconds. The temperatures at $t = 5.6$ seconds are less than those at $t = 5.4$ seconds due to the variation in the applied heat flux load resulting from slipper bounce. Temperatures exceeding the melt temperature ($T_m = 1{,}685$ K) occur close to the leading edge of the slipper beginning at $t = 5.2$ seconds. The elevated temperatures near the leading edge are due to the increased aerodynamic heating effects on the front and bottom edges of the slipper.

Figure 56 shows decreasing temperature distributions along the bottom of the slipper as time progresses from $t = 5.8$ seconds to the end of the run at $t = 8.14$ seconds. In each curve, the maximum temperature is no longer at the leading edge ($x = 0.2032$ m) of the slipper. This is a result of the convective aerodynamic cooling effect on the front as the slipper is decelerating. The maximum temperature occurs behind the leading edge and moves away from the leading edge as time increases.

The mid-height ($y/L = 0.5$) and top surface temperature distribution curves in Fig. 57 to Fig. 60 follow the same trends as those seen in the bottom surface temperature distributions of Fig. 55 and Fig. 56. However, the melt temperature is not exceeded in the mid-height or top temperature distributions.

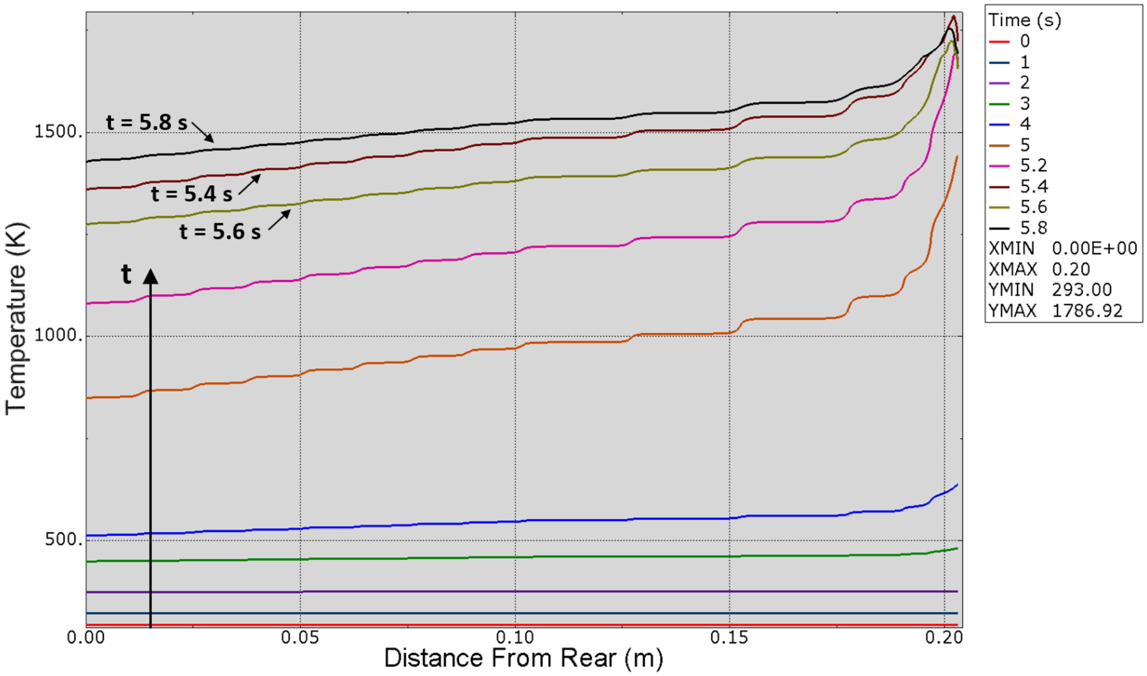

Figure 55: Bottom Surface Temperature, $t = 0$ to 5.8 seconds.

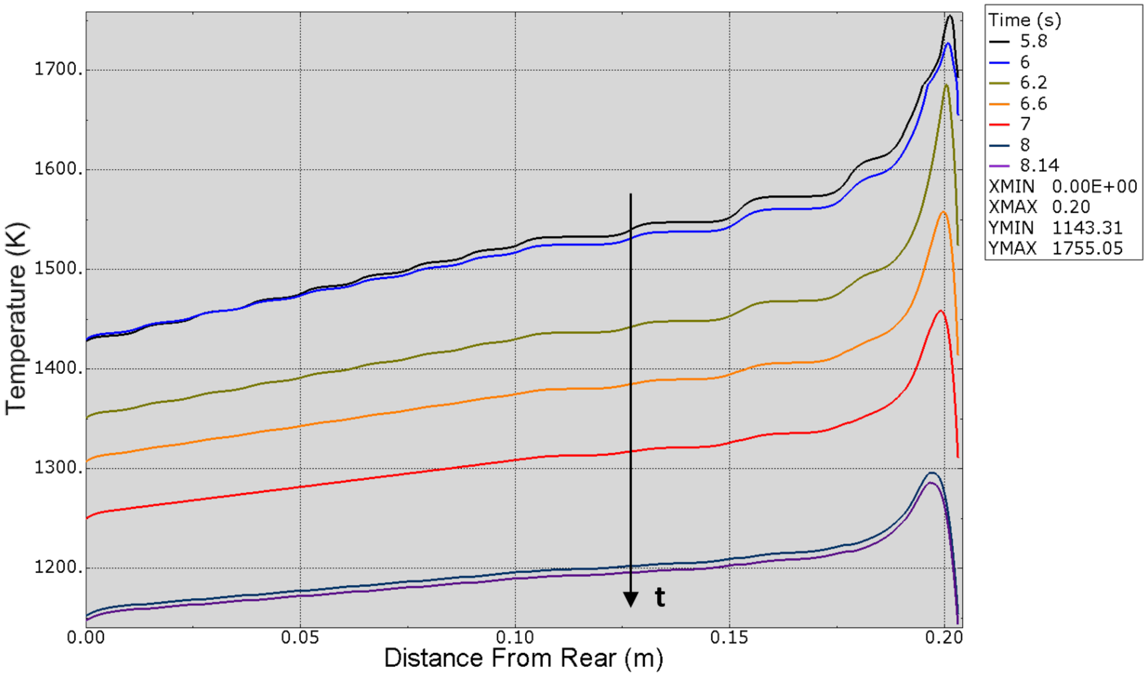

Figure 56: Bottom Surface Temperature, $t = 5.8$ to 8.14 seconds.

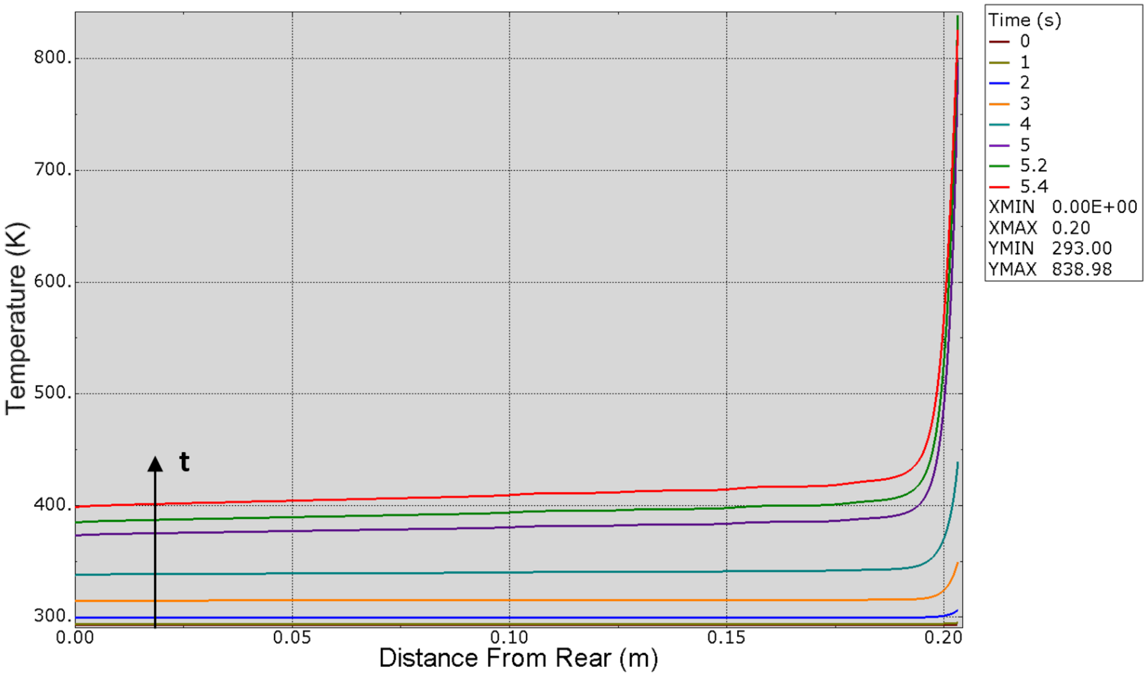

Figure 57: Mid-height $(y/L = 0.5)$ Temperature, $t = 0$ to 5.4 seconds.

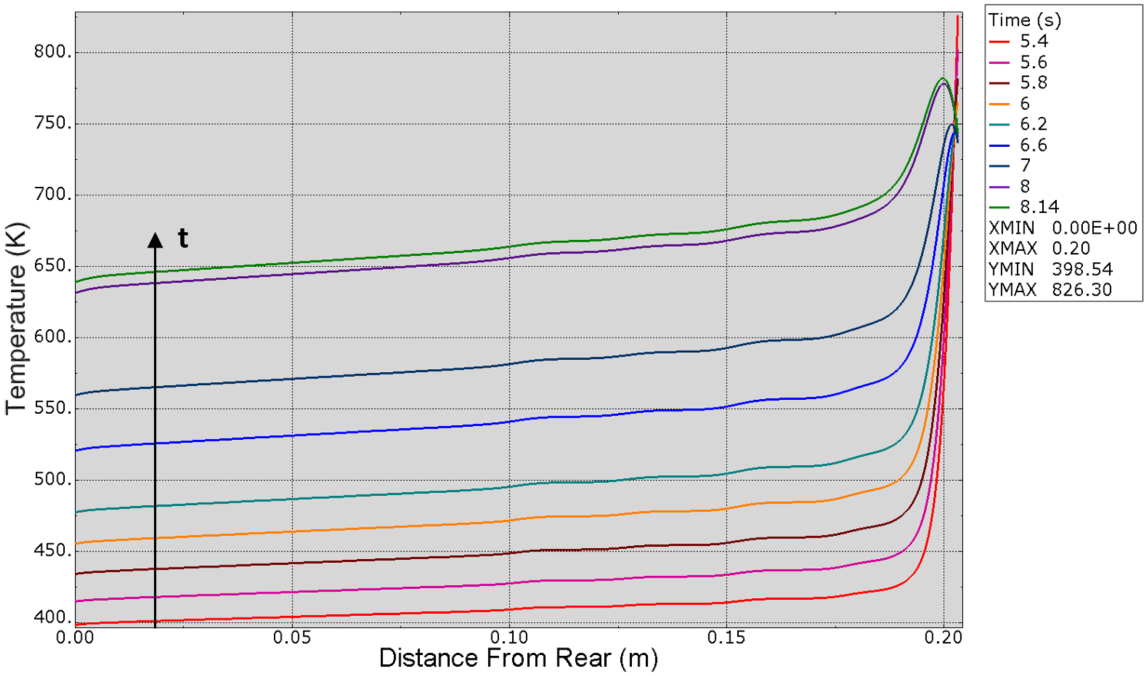

Figure 58: Mid-height $(y/L = 0.5)$ Temperature, $t = 5.4$ to 8.14 seconds.

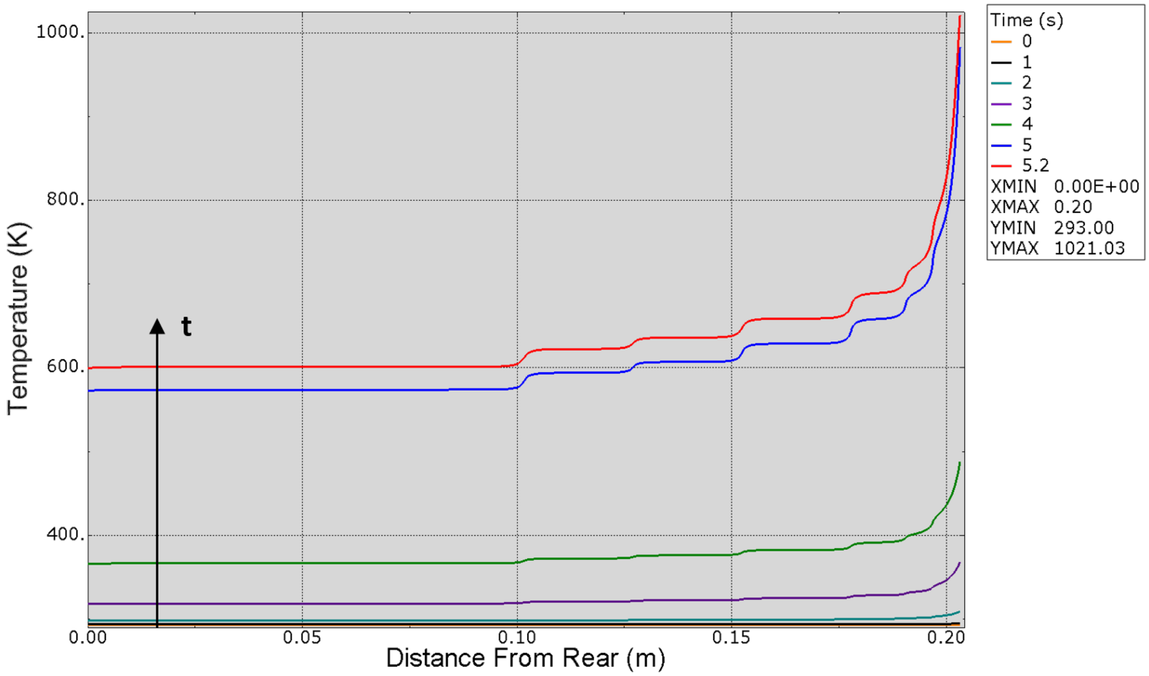

Figure 59: Top Surface Temperature, $t = 0$ to 5.2 seconds.

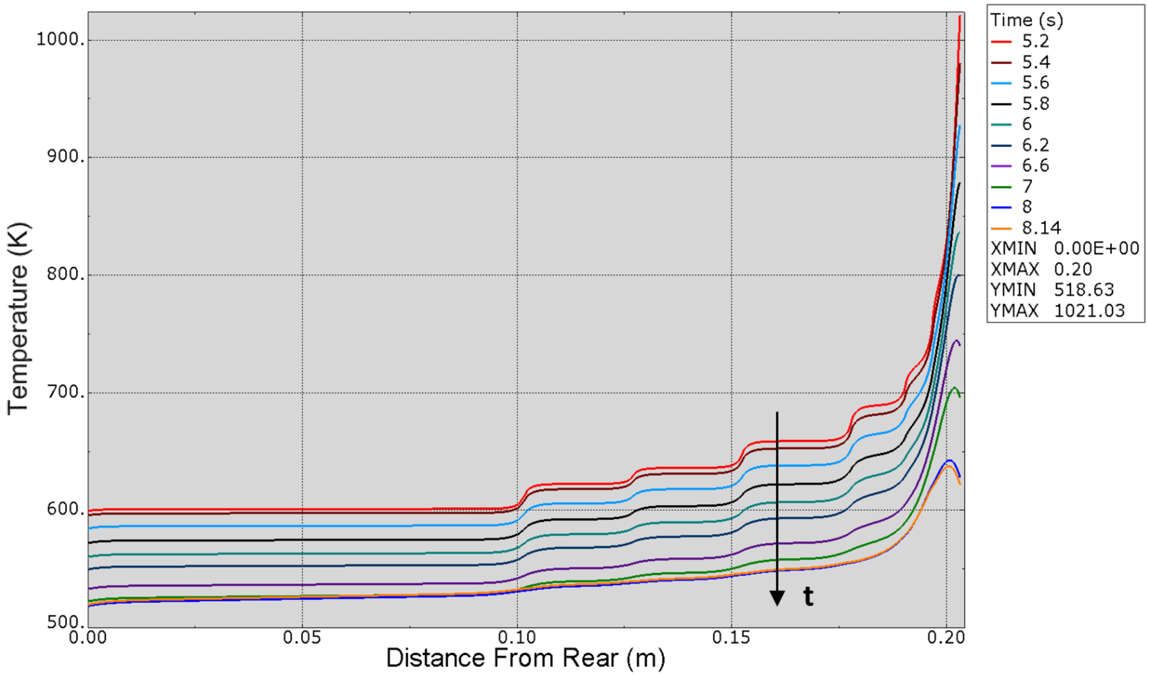

Figure 60: Top Surface Temperature, $t = 5.2$ to 8.14 seconds.

Figures 61 through 69 show temperature variation over the course of the run at single nodes. Each figure illustrates temperature change at multiple nodes (related by geometry) to show how the slipper heats and cools along different surfaces and in different regions over time.

Figure 61 shows temperature variation at four points on the bottom of the slipper. All four curves follow the same oscillatory pattern resulting from the variation in the heat flux due to sliding friction. The differences between the curves are due to the convective aerodynamic heating and cooling effects on the slipper. For the first two seconds of the run, the curves at the four points all follow the same path as the sliding friction heat flux dominates. As the run progresses, the variation of the convective heat flux along the bottom surface leads to temperature differences between the nodes. As expected, the temperature at the leading edge node ($x = 203.2$ mm) is the highest temperature on the bottom surface for most of the run. As seen previously, the temperature at the leading edge exceeds the slipper melt temperature (between 5.1 and 6 seconds). When the sled begins to decelerate and convective cooling takes over on the front surface, the temperature of the leading edge node decreases more rapidly than the temperature of the other three nodes. At approximately 6.4 seconds, the leading edge temperature has decreased to below the temperature at the node 51.8 mm away from the leading edge ($x = 152.4$ mm). By the end of the run, the temperature of the leading edge has decreased to the same temperature as the rear of the slipper, but the interior points are at a higher temperature. This change at the leading edge is a result of aerodynamic cooling on the front of the slipper as the slipper decelerates.

Figure 62 shows temperature variation at six points along the top surface of the slipper. The only heating and cooling occurring on the top surface results from the convective aerodynamic effects. The curves follow the same general trend at all six points. Temperatures increase from the initial value (293 K) to a maximum at approximately 5.2 seconds, then decrease steadily as the sled decelerates for the remainder of the run. As expected, the highest temperatures are seen at the leading edge of the slipper.

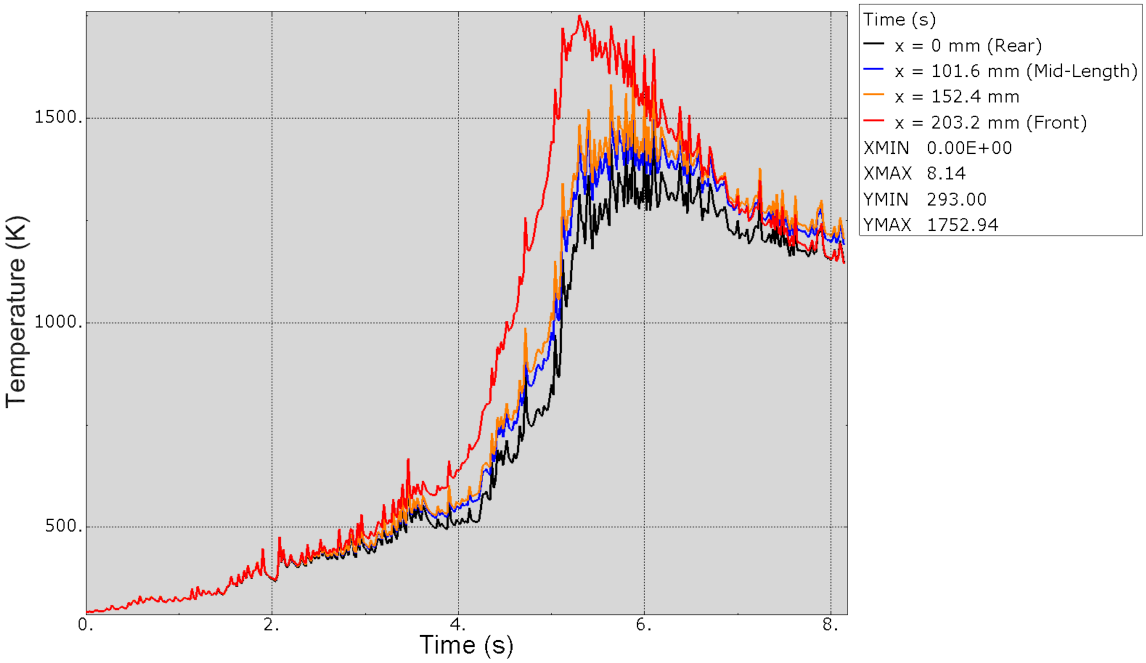

Figure 61: Temperature, Bottom Surface.

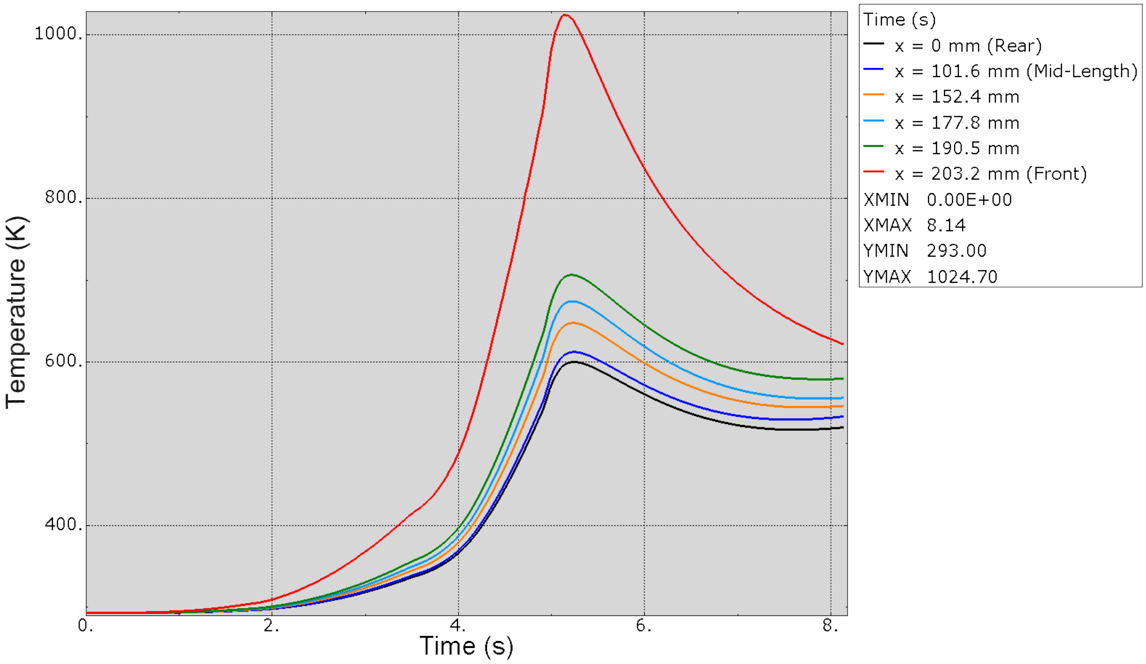

Figure 62: Temperature, Top Surface.

Figures 63 through 65 show the temperature at four points aligned vertically at even intervals from the bottom of the slipper to the top of the slipper. Figure 63 shows the temperature at points along the front surface of the slipper. The highest temperature occurs at the bottom of the slipper. The maximum temperature at the top ($y = 14.7$ mm) is greater than the maximum temperatures seen at the mid-side nodes ($y = 4.9$ and 9.8 mm) on the front face. However, as the slipper decelerates, the temperature at the top decreases steadily due to convective aerodynamic cooling, while the temperature at the mid-side nodes decreases less rapidly as a result of heating from the bottom of the slipper. Further, at $y = 4.9$ mm, the temperature first decreases at $t = 5.1$ seconds then increases to a near constant value due to the coupled effects of aerodynamic cooling on the front and heating on the bottom of the slipper.

Figures 64 and 65 show points aligned vertically on lines inset from the leading edge 12.7 mm and 101.6 mm, respectively. The maximum temperature ($T = 1{,}685.8$ K) on the bottom of the slipper in Fig. 64 indicates this location (12.7 mm from the leading edge) is the rear-most point of the melt region. Steady temperature increase of the interior points, resulting from thermal wave propagation through the slipper, is seen in both figures.

Figure 66 depicts the bottom surface temperature calculated at the slipper mid-length using the one-dimensional finite difference scheme. The curve follows the same general trend as the bottom surface mid-length temperature calculated using the finite element model (the red curve in Fig. 65). A greater number of fluctuations are shown in the finite difference calculated curve because output is shown at each 0.2 ms time step, whereas the finite element output is only shown at each 20 ms increment. Clearly, the finite element calculated surface temperature is higher than the finite difference solution throughout the run. This difference in temperature magnitude may be due to the fact that the convective heat flux applied to the finite element model was calculated using the surface temperature output from the finite difference solution and produces a heat flux that is too large. The actual temperature distribution may be between the two curves. In future research, implementation of an iterative solution accounting for temperature dependent properties in the air flow at each time step would be appropriate.

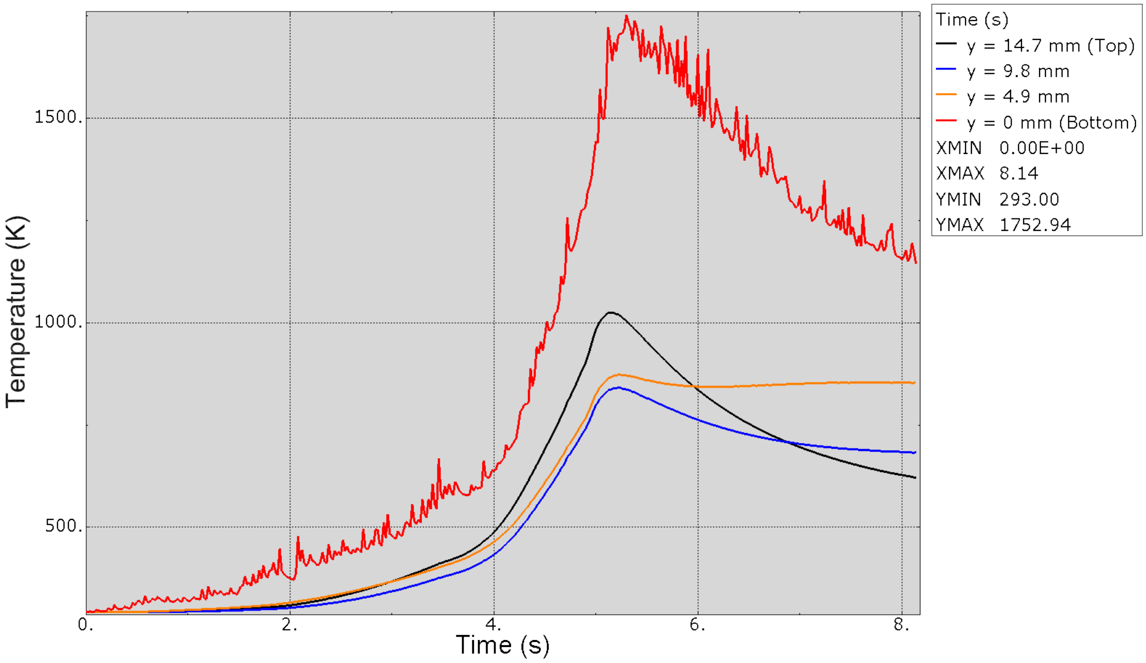

Figure 63: Temperature, Front Surface.

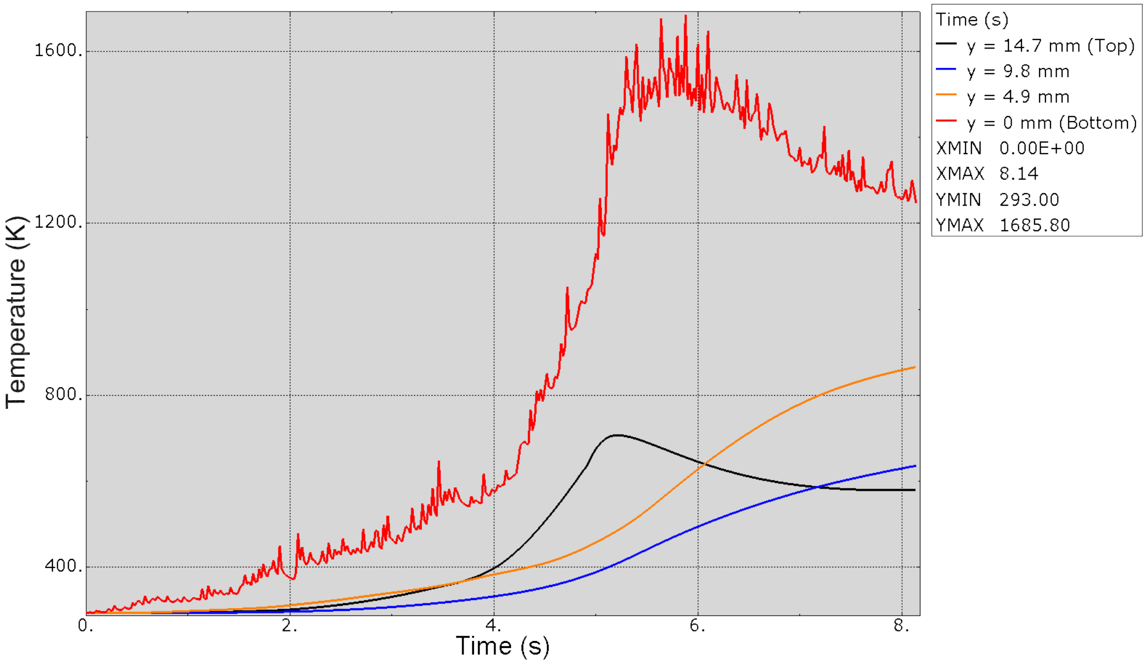

Figure 64: Temperature, 12.7 mm From Front Surface.

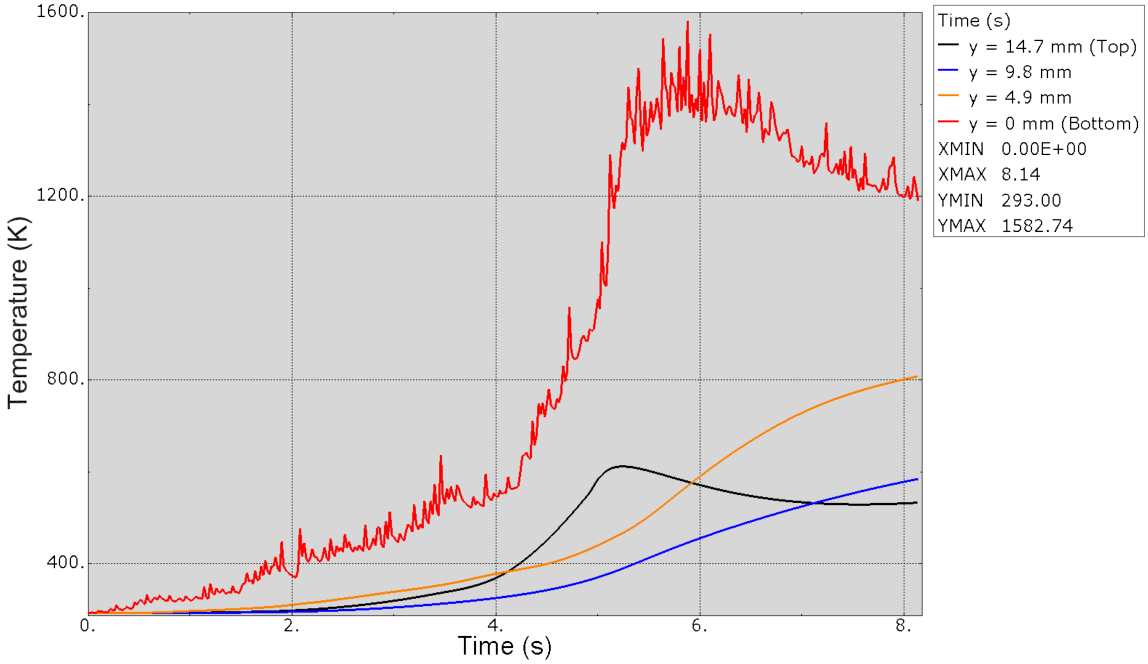

Figure 65: Temperature, Mid-Length.

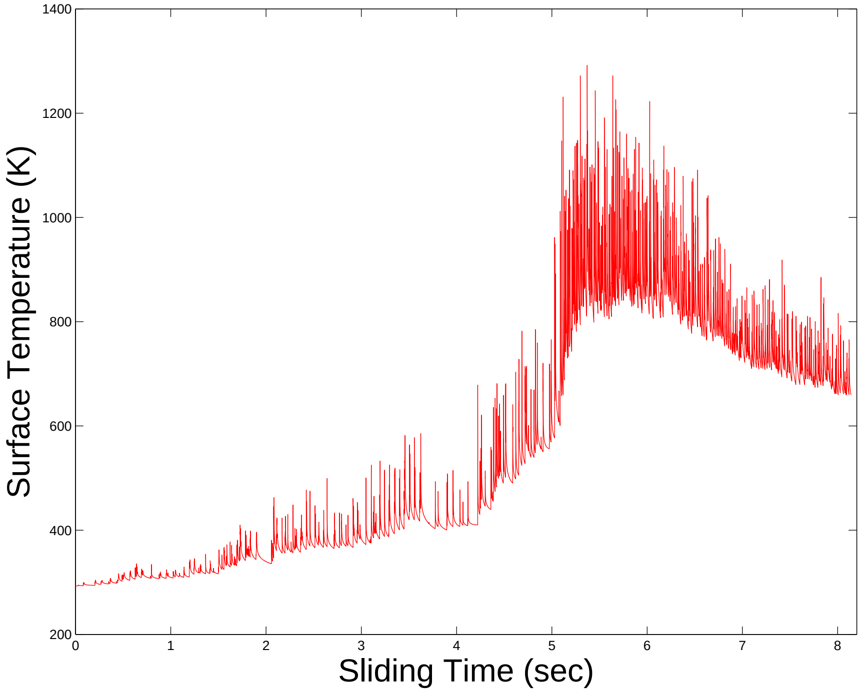

Figure 66: Surface Temperature, Mid-Length, Finite Difference.

Figures 67 through 69 show temperature variation at points aligned horizontally along a line 4.9 mm above the bottom surface of the slipper. The leading edge ($x = 203.2$ mm) temperature curve is the same in each figure and is shown in red. Figure 67 shows temperatures at points on this horizontal line over the entire length of the slipper. Figure 68 shows points on the line between the leading edge point and the first point away from the leading edge in Fig. 67 ($x = 190.5$ mm, shown in green in both figures). Figure 69 shows points on the line between the leading edge point and the first point away from the leading edge in Fig. 68 ($x = 201.6$ mm, shown in light blue in both figures).

The three figures illustrate the relative degree of influence of the heat flux on the bottom and the convective film on the front of the slipper. For most of the length of the slipper, the temperature increase with time results from heating on the bottom of the slipper. Figure 69 shows that the aerodynamic effects on the front surface only significantly affects the temperature in the region near the front of the slipper.

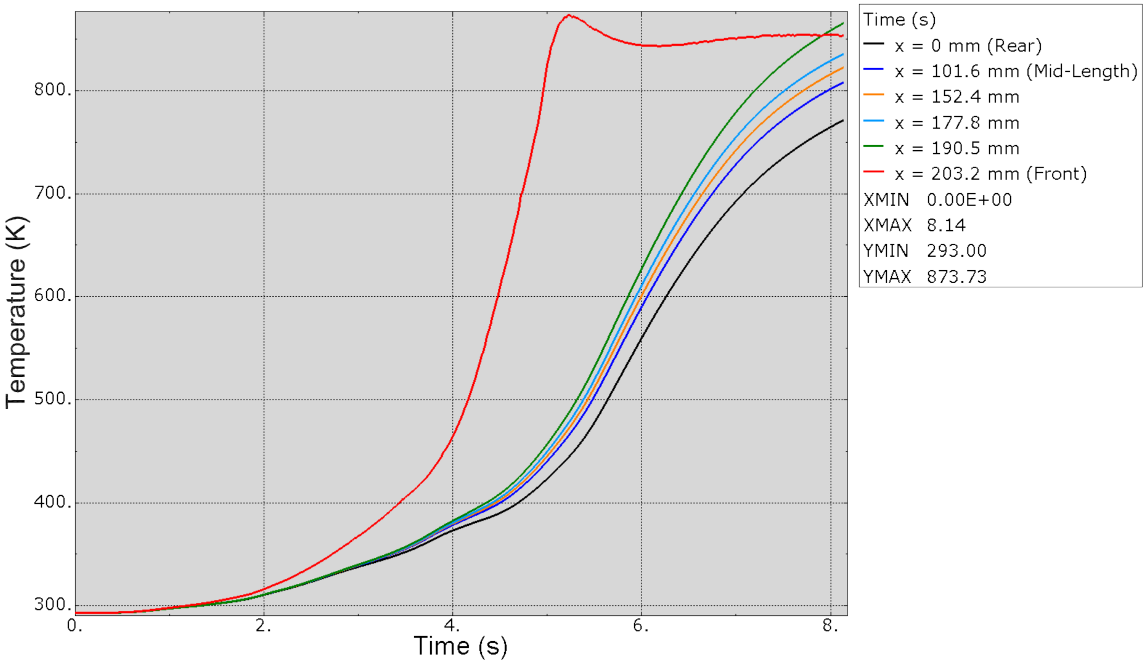

Figure 67: Temperature, 4.9 mm Above Bottom Surface, Total Length.

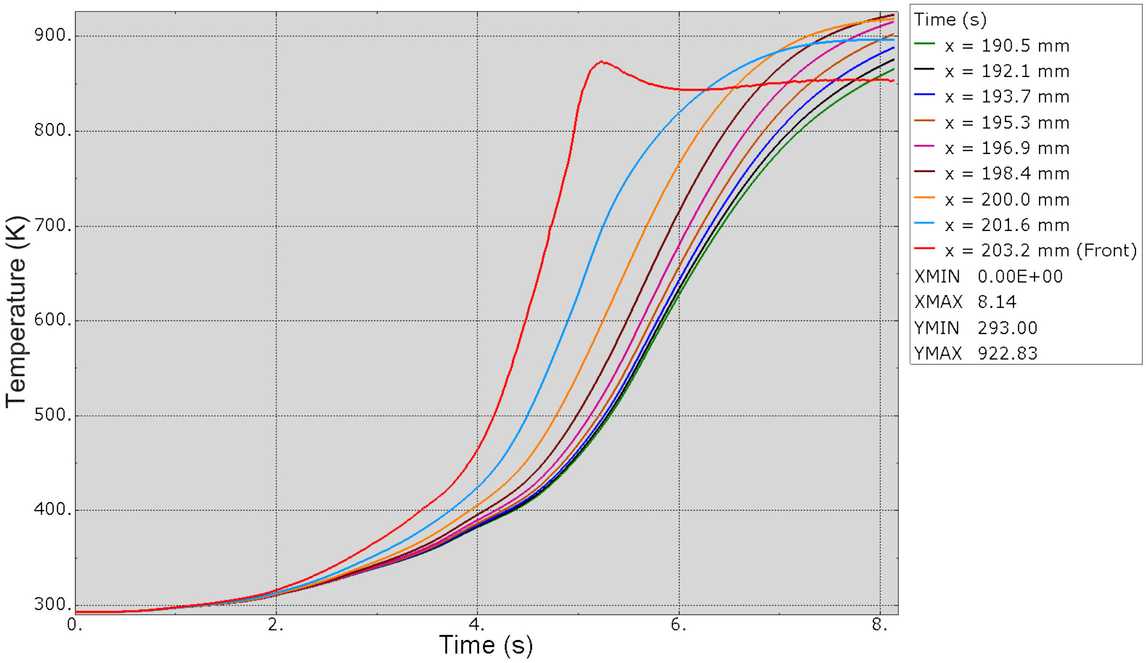

Figure 68: Temperature, 4.9 mm Above Bottom Surface, Front 12.7 mm.

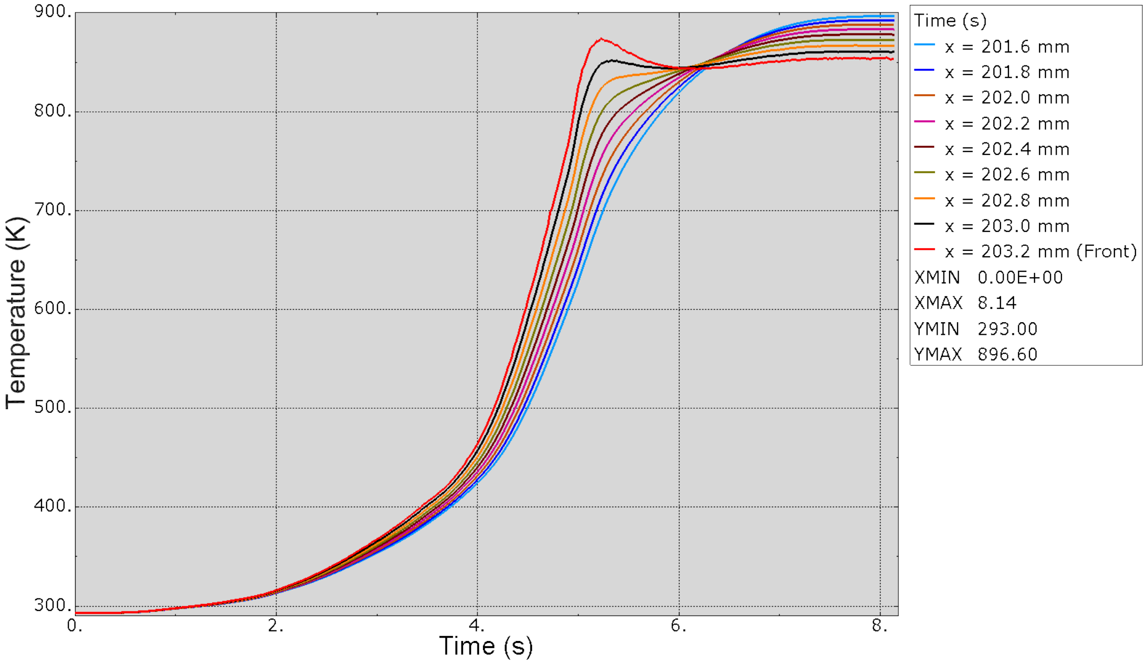

Figure 69: Temperature, 4.9 mm From Bottom Surface, Front 1.6 mm.

5.3.2 Two-Dimensional Temperature Contours

A significant advantage to using the finite element model in the Abaqus commercial software package over the finite difference code in MATLAB is the ease with which results may be displayed and interpreted. Temperature distributions have been generated at each of the 40,700 time steps.

The temperature scale is the same for all temperature distributions in order to facilitate comparison between the images. Temperatures vary from the minimum, initial slipper temperature (T = 293 K) to a the VascoMax 300 melt temperature (T = 1,685 K) in increments of 100 K.

Two temperature distributions are shown at each time step. Figures 70(a) to 79(a) show the complete slipper cross section. Figures 70(a) to 79(a) show the front 25.4 mm (the leading edge) of the slipper.

For the first few seconds of the simulation, the temperature distributions show little activity of interest. Convective heat flux pulses due to the slipper hitting the rail are minimal and conductive heat flux acts to cool the bottom surface. Prior to 4.00 seconds, on the scale shown, temperature within the slipper distribution is not significantly affected. The temperature does rise above the 300 K threshold almost immediately in most of the slipper, but temperatures greater than 400 K do not occur until after 3 seconds.

At 4.00 seconds (Fig. 70), the slipper shows the first signs of the effects of the aerodynamic heating. Temperatures in excess of 400 K are observed on the leading edge. The sled velocity at this point is 901.3 m/s which leads to a (post-shock) Total temperature of 694.3 K. The elevated film temperature coupled with a heat transfer coefficient of 4,573 W/m^2-K leads to a greater than 1×10^6 W/m^2 heat convective heat flux into the slipper's front face.

Convective heating effects are also observed on the top of the slipper. The largest heat transfer coefficient values are applied to the front 6 mm of the slipper. At the leading edge, the convective heating is affected by heating from both the top and the front faces so the 400 K wave extends furthest from either surface in that corner.

(a) Complete Slipper, $H = 14.7$ mm, $L = 203.2$ mm.

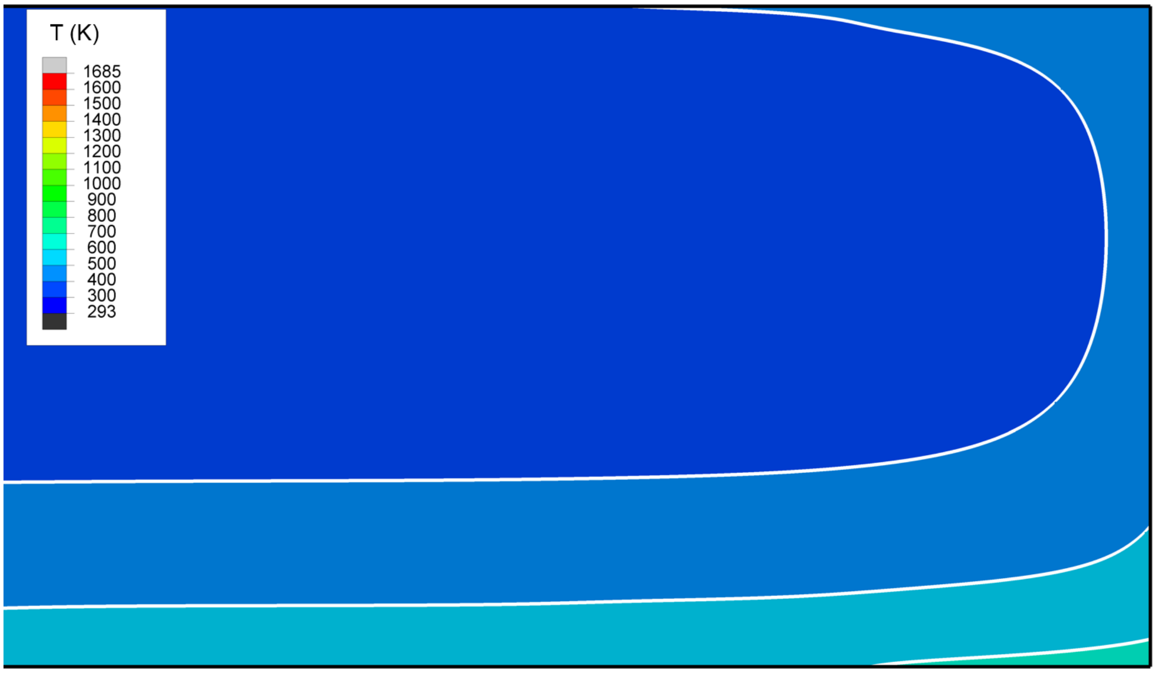

(b) Slipper Leading Edge, $H = 14.7$ mm, $L = 25.4$ mm.

Figure 70: Temperature Distribution, $t = 4.00$ s.

The temperature on the bottom of the slipper, away from the leading edge, has increased to greater than 500 K for the entire slipper length. Near the front, the temperature has exceeded 600 K as a result of the combination of conductive heating into the bottom and the aerodynamic heating on the front.

At 4.50 seconds (Fig. 71), the sled speed has increased to 1,224 m/s and the total temperature in the front film has exceeded 1,000 K. A heat transfer coefficient of almost 7,000 W/m^2-K leads to a heat flux of $3{\times}10^6$ W/m^2. At this point, temperature in the coolest section of the slipper front surface is approaching 600 K.

Heating on the top has increased the temperature of the entire surface to an excess of 400 K. The combined effects of the aerodynamic heating on the front and top surfaces force the temperature of the top of the leading edge to well above 600 K.

Temperatures on the bottom surface exceed 700 K along most of the surface and at

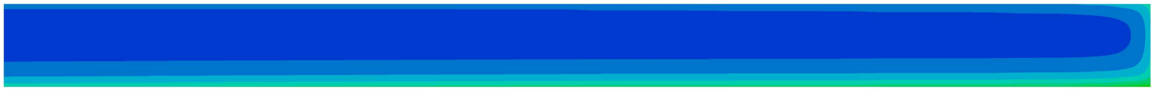

(a) Complete Slipper, $H = 14.7$ mm, $L = 203.2$ mm.

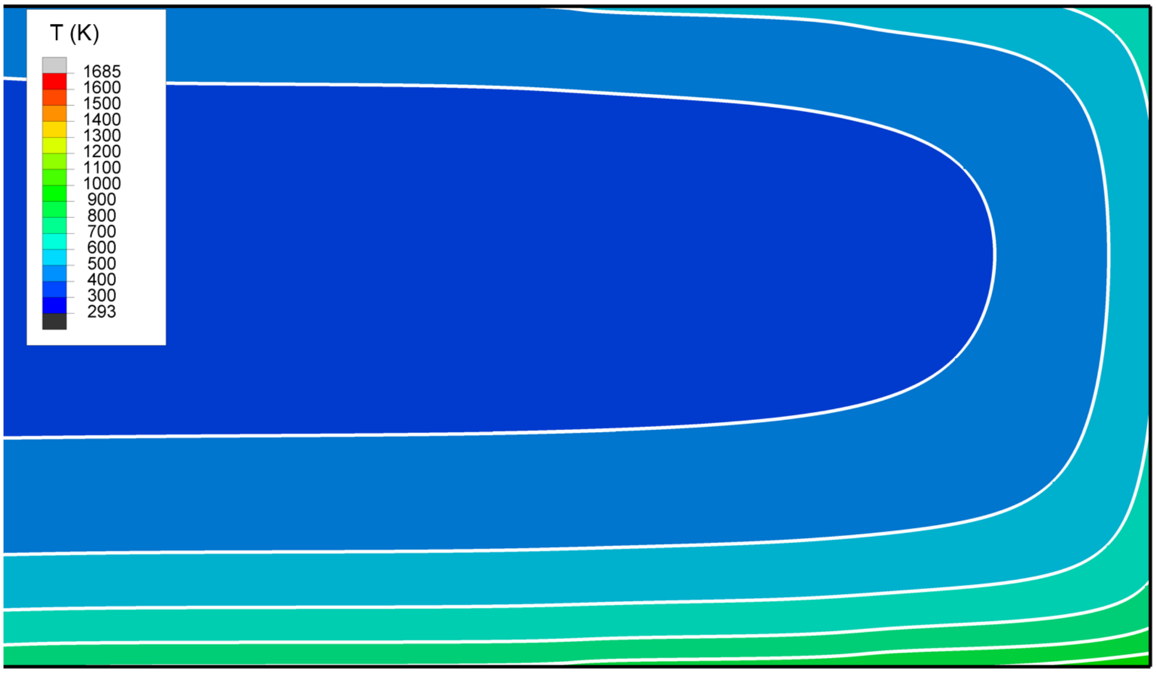

(b) Slipper Leading Edge, $H = 14.7$ mm, $L = 25.4$ mm.

Figure 71: Temperature Distribution, $t = 4.50$ s.

the leading edge are over 900 K.

At 5.00 seconds (Fig. 72) the sled speed ($v = 1,528.7$ m/s) is almost at its maximum ($v = 1,528.9$ m/s). The temperature of the entire front face has exceeded 900 K and the total temperature in the film is 1,444 K. With a heat transfer coefficient at this point of 9,300 W/m^2-K, the surface is exposed to a heat flux of 3×10^6 W/m^2.

The temperature at every point on the upper surface is over 500 K and above 900 K at every point on the front. The temperature along the bottom surface is above 1,400 K at the leading edge and exceeds 900 K at every point on its length. At 5.00 seconds, the onset of melt has not yet occurred.

Approximately 5 seconds into the run, the third stage rocket is expended and the third stage sled is released. Without the acceleration provided by the rocket and the aerodynamic lifting effects, the weight of the sled now begins to dominate the forces in the

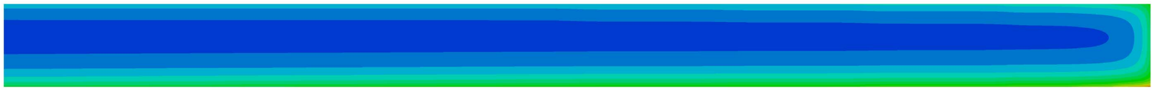

(a) Complete Slipper, $H = 14.7$ mm, $L = 203.2$ mm.

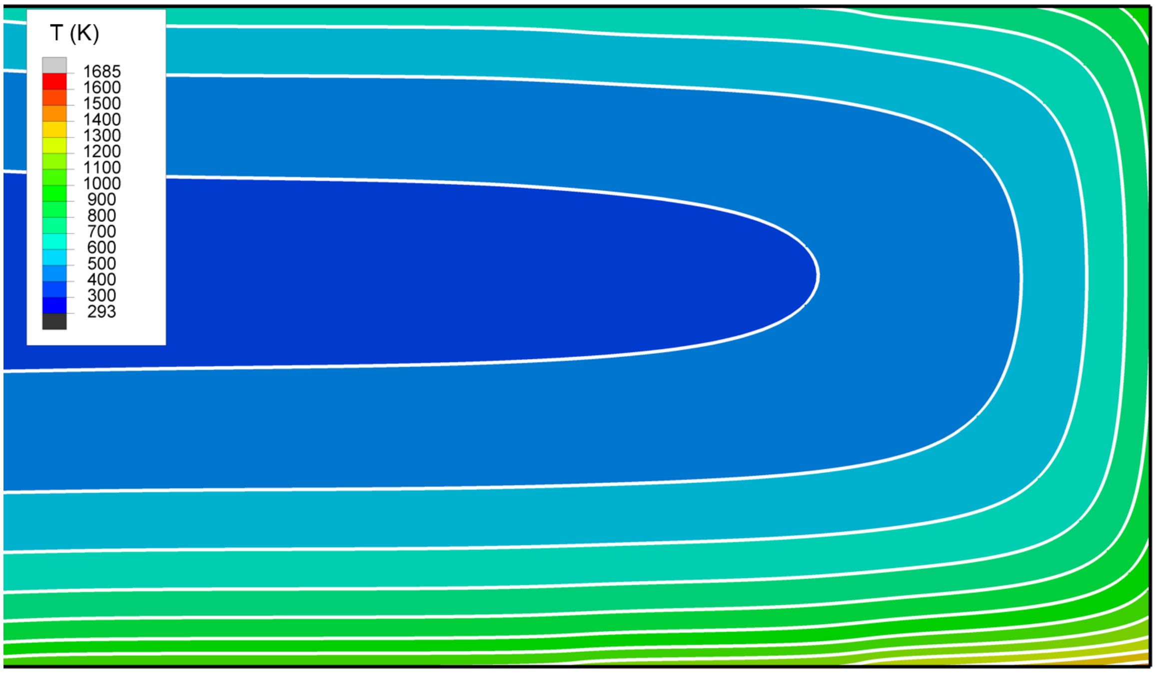

(b) Slipper Leading Edge, $H = 14.7$ mm, $L = 25.4$ mm.

Figure 72: Temperature Distribution, $t = 5.00$ s.

vertical direction. The slipper contacts the rail with greater downward dynamic force and the friction between the slipper and the sled (coupled with aerodynamic drag) causes the sled to decelerate. As a result, the bottom surface sees the largest conductive heat flux values between t = 5 and 6 seconds (Fig 30).

The melt temperature is exceeded initially at 5.1 seconds. A small section of the slipper at the bottom of the leading edge has a temperature above the melting point for approximately one second seen in Figs. 73 to 76. The size of the melted region is different at each time step and varies both in depth into the slipper and length across the bottom. The largest melt areas are seen in the temperature distributions at 5.38 and 5.64 seconds (Figs. 73 and 75).

The temperature on the bottom surface has exceeded 1,400 K for most of the length of the slipper. Temperatures on the front and the top of the slipper are higher than they

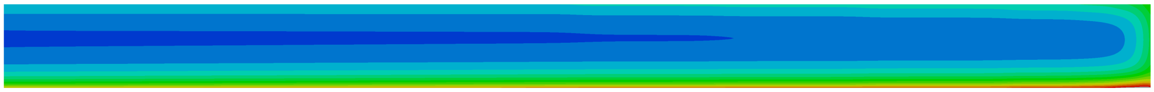

(a) Complete Slipper, $H = 14.7$ mm, $L = 203.2$ mm.

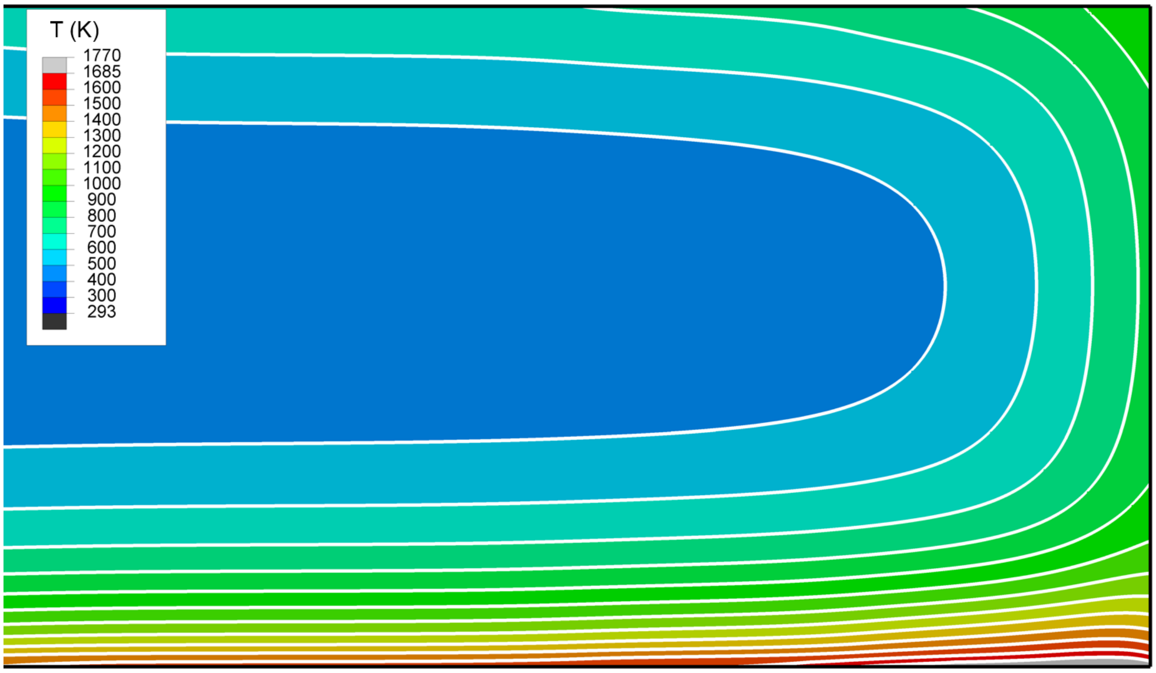

(b) Slipper Leading Edge, $H = 14.7$ mm, $L = 25.4$ mm.

Figure 73: Temperature Distribution, $t = 5.38$ s.

were at 5.00 seconds, but they are now close to their peak values. Away from the slipper surfaces, the temperature continues to increase as the heat from the warmer surface regions naturally flows to the cooler region in the middle.

The largest melt region occurs at 5.38 seconds (Fig. 73(b)).

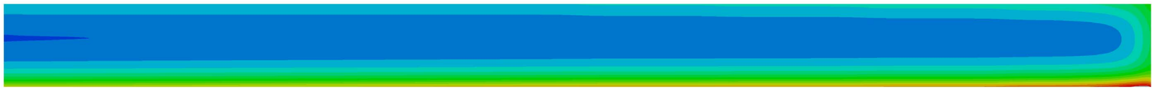

(a) Complete Slipper, $H = 14.7$ mm, $L = 203.2$ mm.

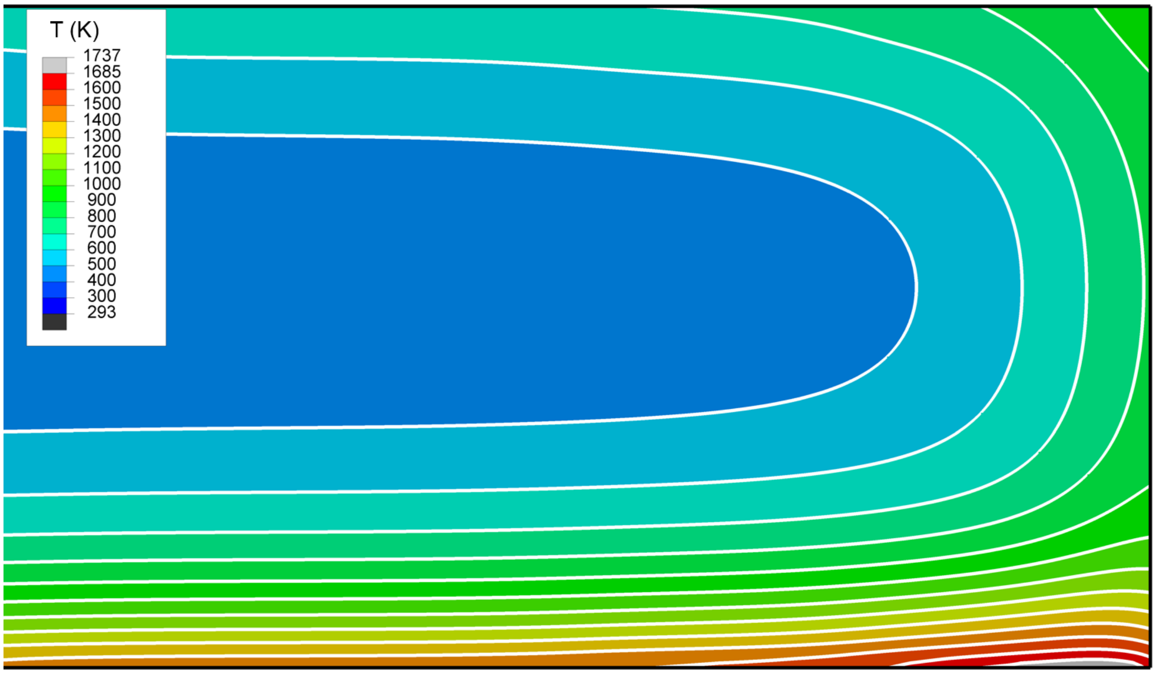

(b) Slipper Leading Edge, $H = 14.7$ mm, $L = 25.4$ mm.

Figure 74: Temperature Distribution, $t = 5.50$ s.

At 5.50 seconds (Fig. 74), the melt region has moved away from the leading edge of the slipper. As the model is not capable of removing elements in which the melt temperature has been exceeded, decreasing temperature in a region that has exceeded the melt temperature will lead to a corresponding reduction in the latent heat affected specific heat. When enough energy has been removed via convective cooling and the melt temperature has been reached from above, the model will again treat the region as solid. In reality, some of the slipper material would be removed and the heat flux loads would be applied at a location that is currently inside the model.

Temperatures on the front and top surfaces have stabilized as the sled is decelerating and heat fluxes on those surfaces are decreasing. The heat continues to propagate into the middle and the temperature has exceeded 400 K for almost the entire slipper.

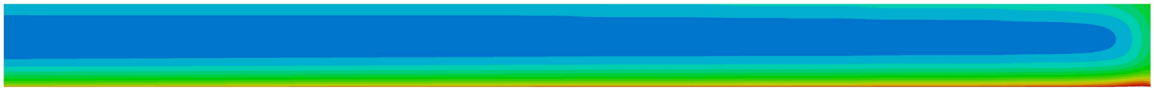

(a) Complete Slipper, $H = 14.7$ mm, $L = 203.2$ mm.

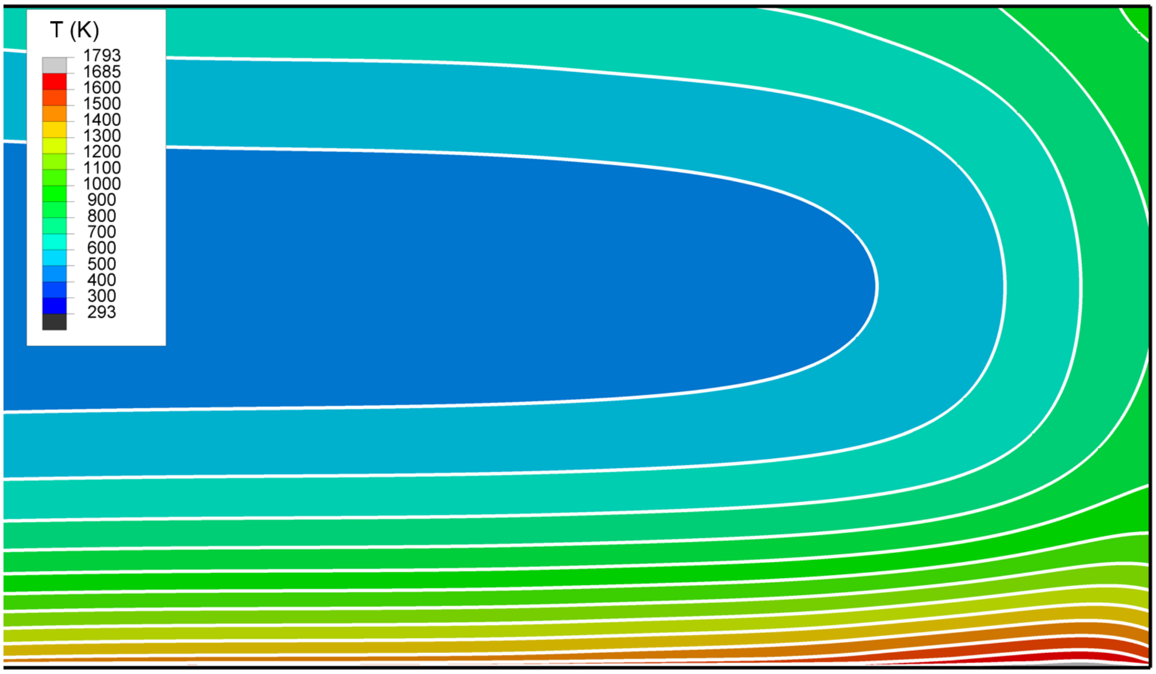

(b) Slipper Leading Edge, $H = 14.7$ mm, $L = 25.4$ mm.

Figure 75: Temperature Distribution, $t = 5.64$ s.

The second largest melt area occurs at 5.64 seconds (Fig. 75). Bottom surface temperatures continue to increase with the large conductive heat flux loads. Temperatures on the top and front are now beginning to decrease as the adiabatic wall and total temperatures are less than the surface temperatures. The internal temperature is above 400 K throughout the slipper.

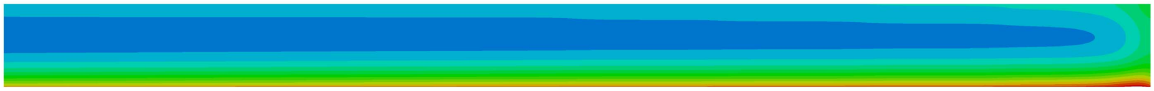

(a) Complete Slipper, $H = 14.7$ mm, $L = 203.2$ mm.

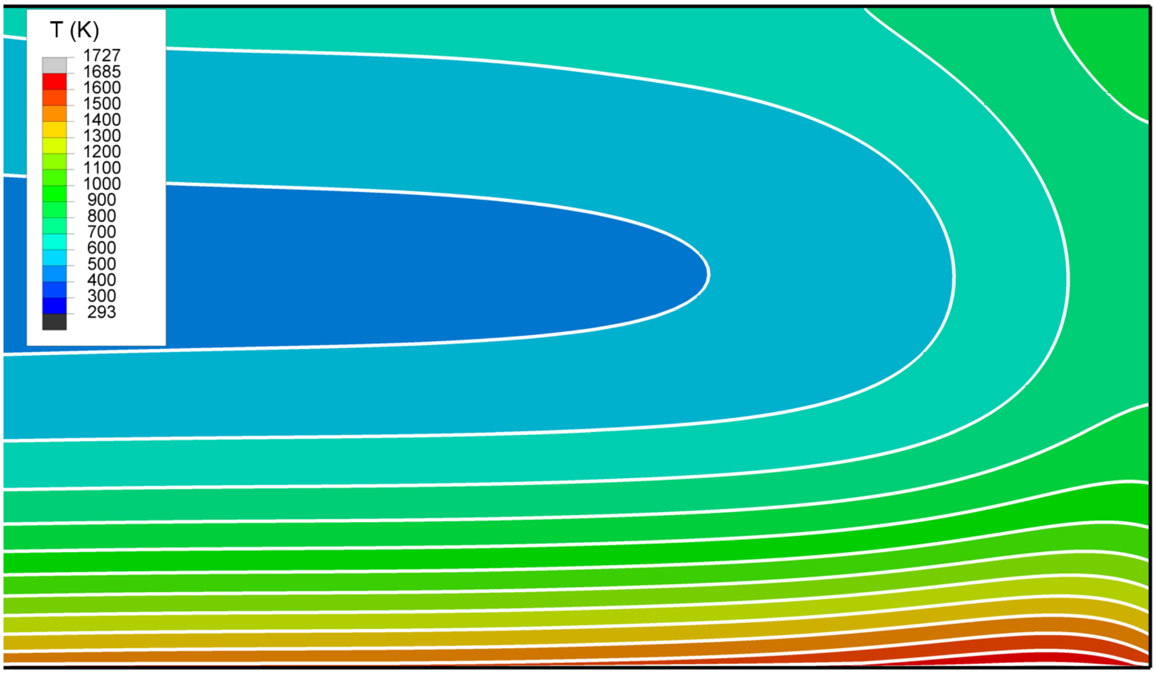

(b) Slipper Leading Edge, $H = 14.7$ mm, $L = 25.4$ mm.

Figure 76: Temperature Distribution, $t = 6.00$ s.

At 6.00 seconds (Fig. 76), the melt region is much smaller than it had been as the conductive heat flux magnitudes on the bottom surface decrease with decreasing sled velocity. The elevated surface temperatures on the front and top continue to decrease as heat is removed via convection to the surrounding air and conduction to the middle of the slipper.

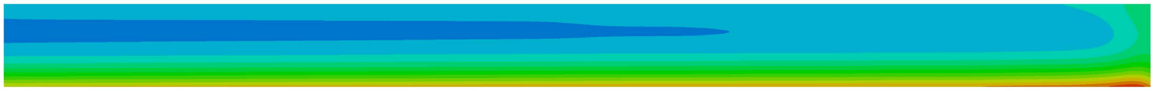

(a) Complete Slipper, $H = 14.7$ mm, $L = 203.2$ mm.

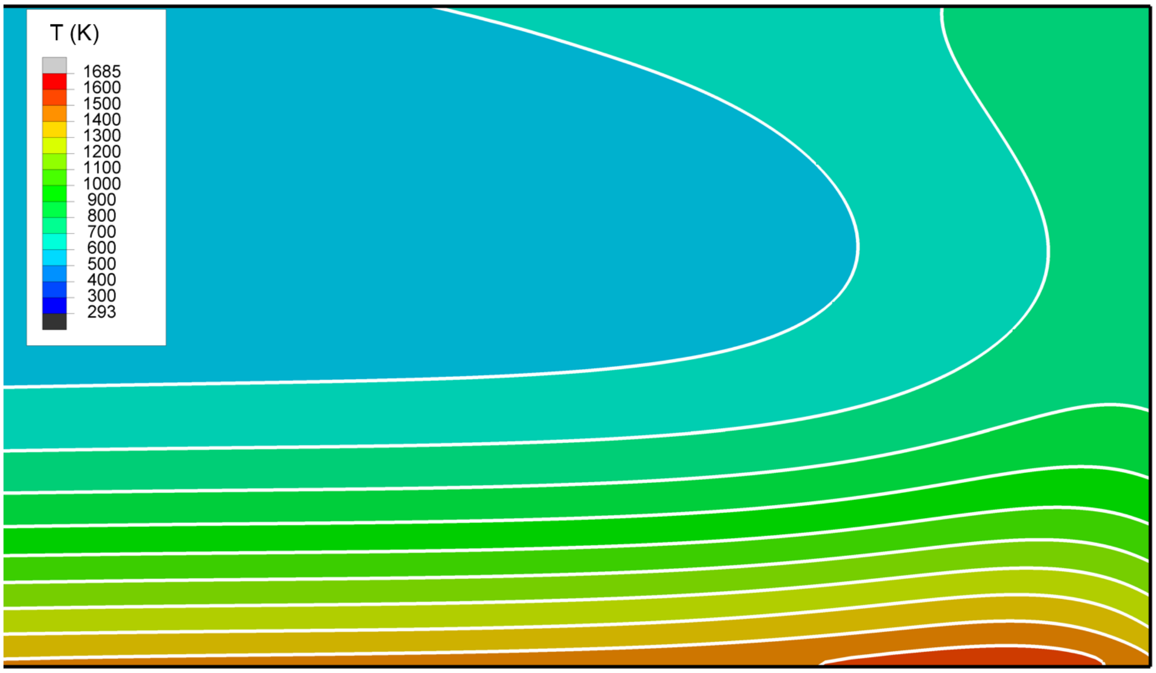

(b) Slipper Leading Edge, $H = 14.7$ mm, $L = 25.4$ mm.

Figure 77: Temperature Distribution, $t = 6.50$ s.

At 6.50 seconds (Fig. 77), the melt region is completely gone. Cooling due to convection has resolidified the entire region. The highest temperature in the slipper remains in the same region where melt existed. The model stored the energy that would have naturally gone to melting the slipper material, so the temperatures in this region are higher than they would have been had the material been removed from the slipper. Cooling on the front surface of the slipper has moved the previously melted, high temperature region on the bottom surface away from the leading edge.

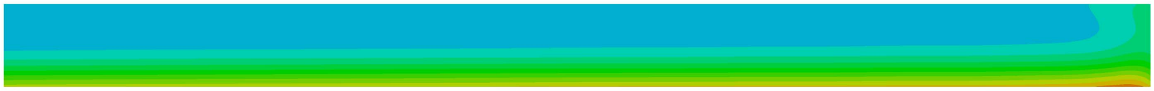

(a) Complete Slipper, $H = 14.7$ mm, $L = 203.2$ mm.

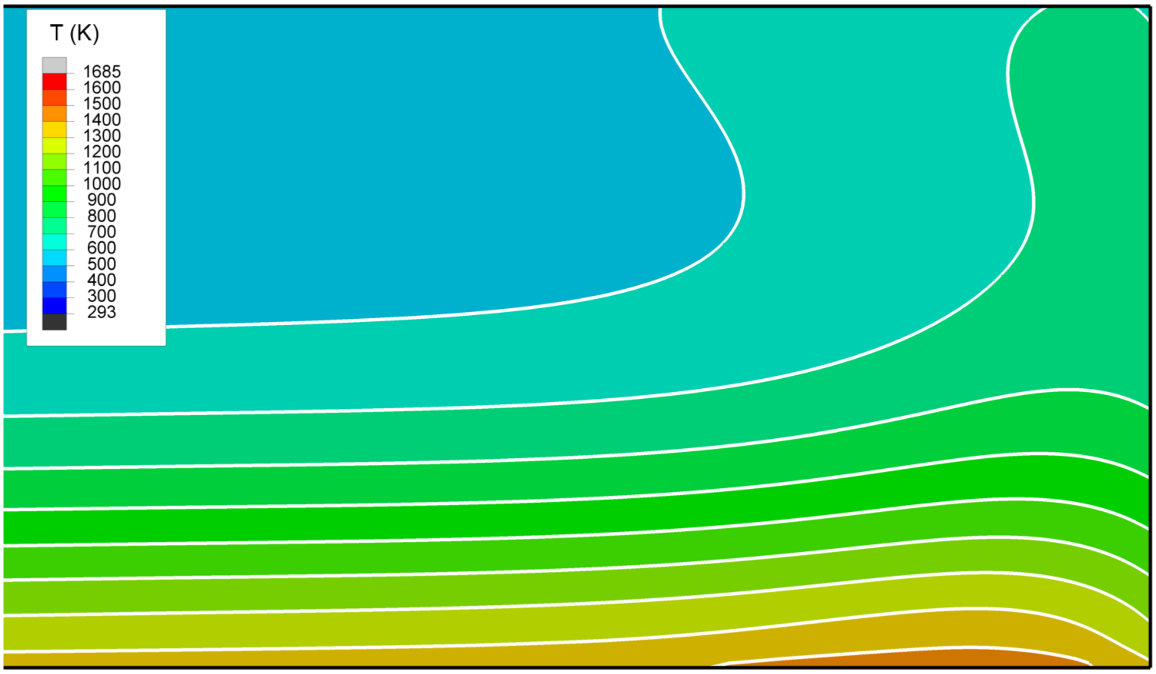

(b) Slipper Leading Edge, $H = 14.7$ mm, $L = 25.4$ mm.

Figure 78: Temperature Distribution, $t = 7.00$ s.

At 7.00 seconds (Fig. 78), cooling continues on all of the slipper surfaces. The thermal wave from the bottom surface continues to push upwards through the slipper and the entire slipper temperature has now exceeded 500 K. Further, the mid-thickness temperature is close to 600 K.

A heat flux reversal is observed on the top surface near the front of the slipper. Temperatures had been increasing in this region and are now decreasing due to the fact that the adiabatic wall film temperature is less than the temperature on the surface of the slipper. The outward directed heat flux vectors on the top surface of Fig. 92 in Section 5.3.4 further illustrates the convective cooling effect.

(a) Complete Slipper, $H = 14.7$ mm, $L = 203.2$ mm.

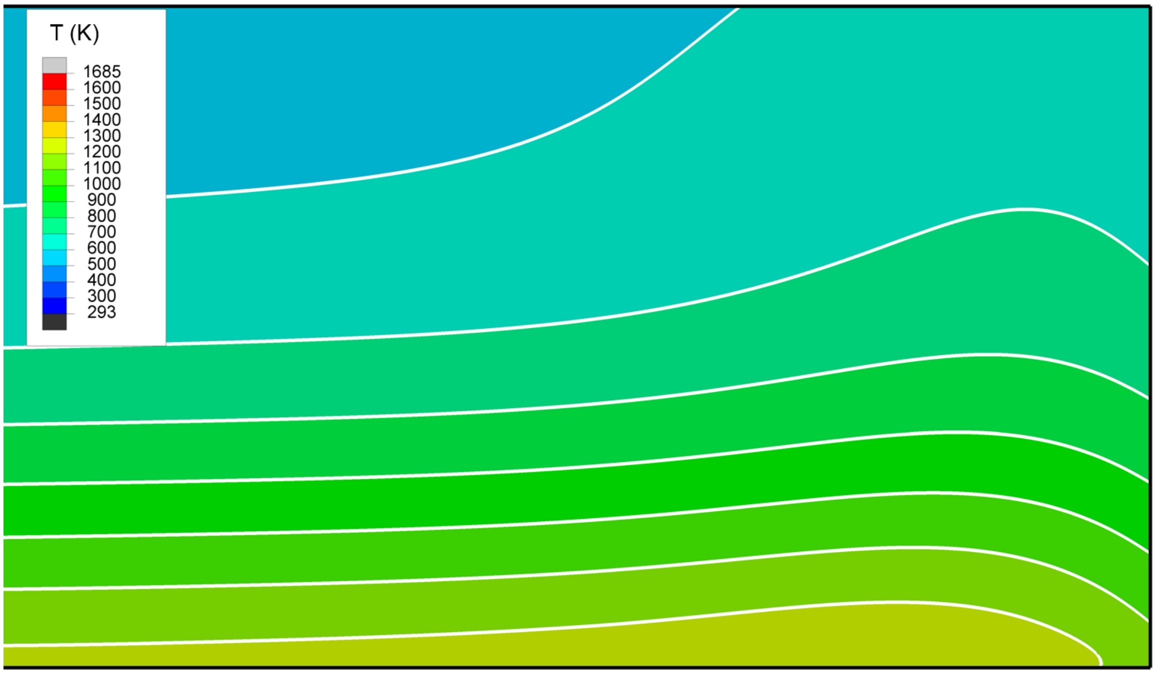

(b) Slipper Leading Edge, $H = 14.7$ mm, $L = 25.4$ mm.

Figure 79: Temperature Distribution, $t = 8.14$ s.

The temperature distribution at 8.14 seconds (Fig. 79) is largely unchanged from the distribution at 7.00 seconds (Fig. 78). Intervening distributions are, therefore, not included.

The heat from the melted region has almost completely dissipated and while the temperature along the front surface is elevated compared to the rest of the slipper, it is significantly decreased from its maximum.

After 8.14 seconds, the distribution would continue to equilibrate to an even distribution similar to that seen in the rear of the slipper. No data exists beyond $t = 8.14$ seconds.

5.3.3 One-Dimensional Heat Flux Distributions

Figures 80 to 85 show one-dimensional heat flux distributions along the front, bottom, and top surfaces of the slipper. As with the one-dimensional temperature distributions, the heat flux distributions are divided into two sets along each surface in order to eliminate overlapping periods of increasing and decreasing heat flux over the course of the run.

Heat flux distributions on the front surface of the slipper are shown in Fig. 80 and Fig. 81. On the front face of the slipper, positive is out of the slipper and negative is into the slipper. This is due to the orientation of the finite element model and the corresponding direction of the applied heat flux loads.

In Fig. 80, for the first part of the run ($t = 0$ to 5 seconds), heat flux along the front of the slipper is generally increasing in magnitude. For times up to $t = 5$ seconds, the heat flux is into the slipper on the entire front face. Minimum heat flux magnitudes occur at the top and bottom of the slipper because the slipper is hotter in those regions as a result of heating on those surfaces. The difference between the front surface temperature and the film temperature (total temperature) is less at the top and the bottom than it is in the middle region of the front face of the slipper so the magnitude of the heat flux is less. After $t = 5$ seconds, the heat flux magnitude decreases over most of the slipper. Near the bottom of the slipper, the heat flux has switched from negative (into the slipper) to positive (out of the slipper). Again, this is a result of the elevated temperature on the bottom of the slipper due to the conductive, frictional heating.

Heat flux distributions for $t \geq 5.4$ seconds are shown in Fig. 81. Heat flux is into the slipper (negative) for the upper sections of the slipper for $t < 6$ seconds, but with decreasing magnitude as time increases. The decreasing magnitude is due to the deceleration of the sled which has the effect of decreasing the total temperature on the front of the slipper. At $t = 6$ seconds, the heat flux at the top of the slipper is small but positive, indicating a shift from heat flux into the slipper to heat flux out of the slipper. At $t = 6.6$ seconds, the curve consists of only positive values and the heat flux is out of the slipper over the entire front face. Near the bottom surface of the slipper, heat flux variations are seen between $t = 5.4$ and 6.6 seconds. After, $t = 6.6$ seconds, the heat flux near the bottom surface is decreasing due to convective cooling acting on the front and bottom surfaces and smaller conductive loads acting on the bottom surface.

Figures 82 and 83 show variation of heat flux along the bottom surface of the slipper with respect to time. For the bottom of the slipper, positive heat flux loads are into the slipper and negative heat flux is out of the slipper.

In Fig. 82, for the first part of the run ($t < 4$ seconds), the heat flux increases with time. For $t \geq 4$ seconds, the magnitude of the heat flux varies greatly with time. The variation is due to the disparity in magnitudes of the applied, alternating conductive and convective heat flux loads on the bottom surface. For $t > 5.4$ seconds, the heat flux values near the leading edge of the slipper ($x = 0.2032$ m) are less than they are over the rest of the slipper. This is due to the increased temperature in this region resulting from the combination of the largest applied heat flux loads on the bottom of the slipper and the heat flux on the front surface.

Figure 83 shows heat flux distributions along the bottom surface of the slipper for $t \geq 5.8$ seconds. Heat flux over the bottom surface is generally decreasing over this period of the run due to sled deceleration. For $t \geq 6.6$ seconds, heat flux magnitude is generally decreasing with time and is smallest close to the leading edge of the slipper. At $t = 8$ seconds, the heat flux in regions near the leading edge of the slipper is negative indicating convective cooling now dominates the heat flux in this region.

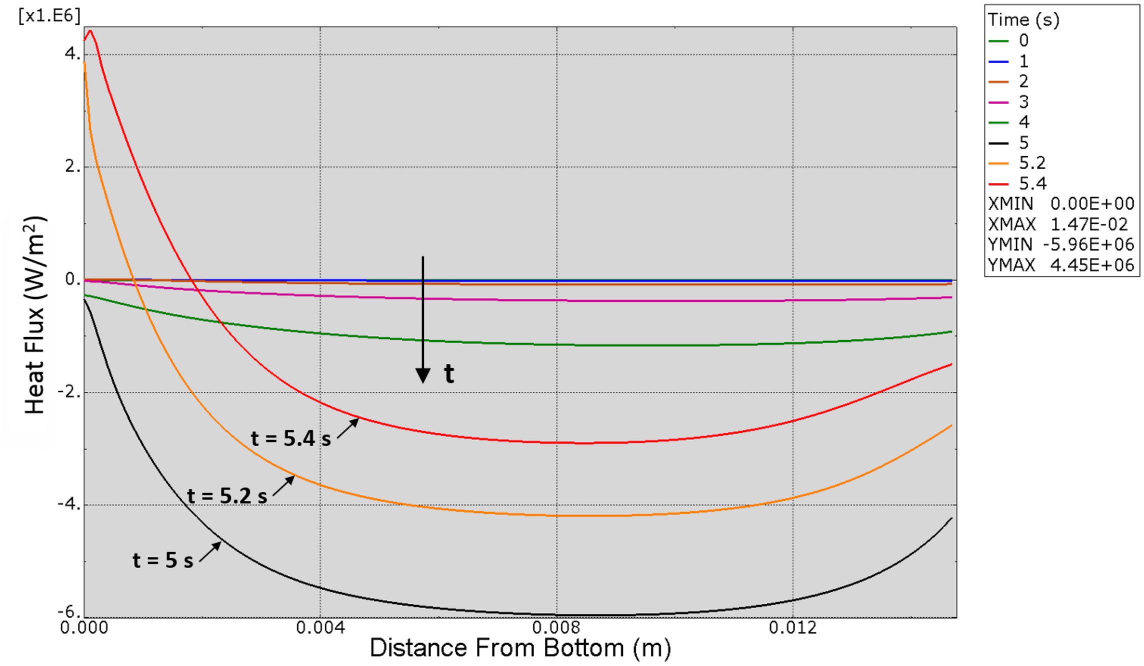

Figure 80: Front Surface Heat Flux, Horizontal Component, $t = 0$ to 5.4 seconds.

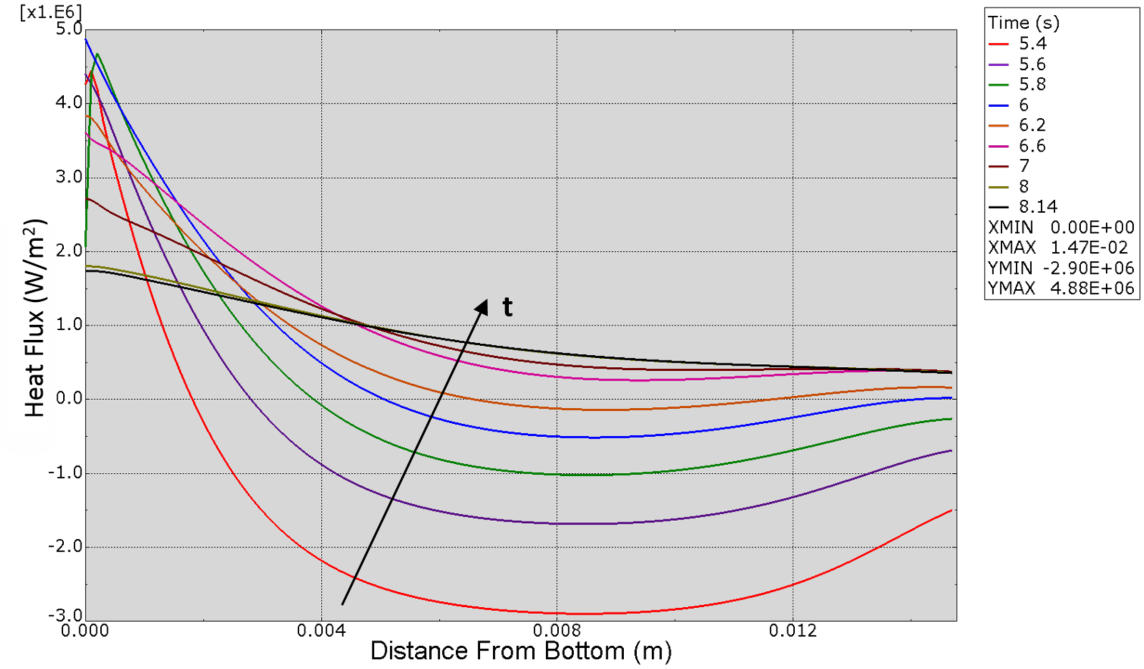

Figure 81: Front Surface Heat Flux, Horizontal Component, $t = 5.4$ to 8.14 seconds.

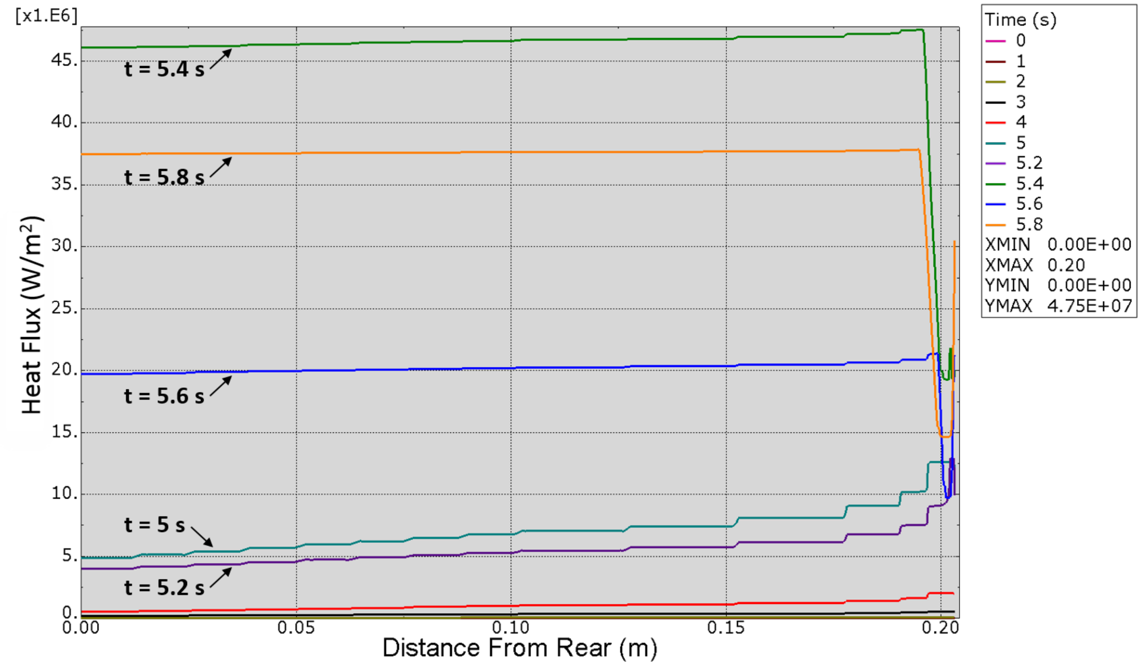

Figure 82: Bottom Surface Heat Flux, $t = 0$ to 5.8 seconds.

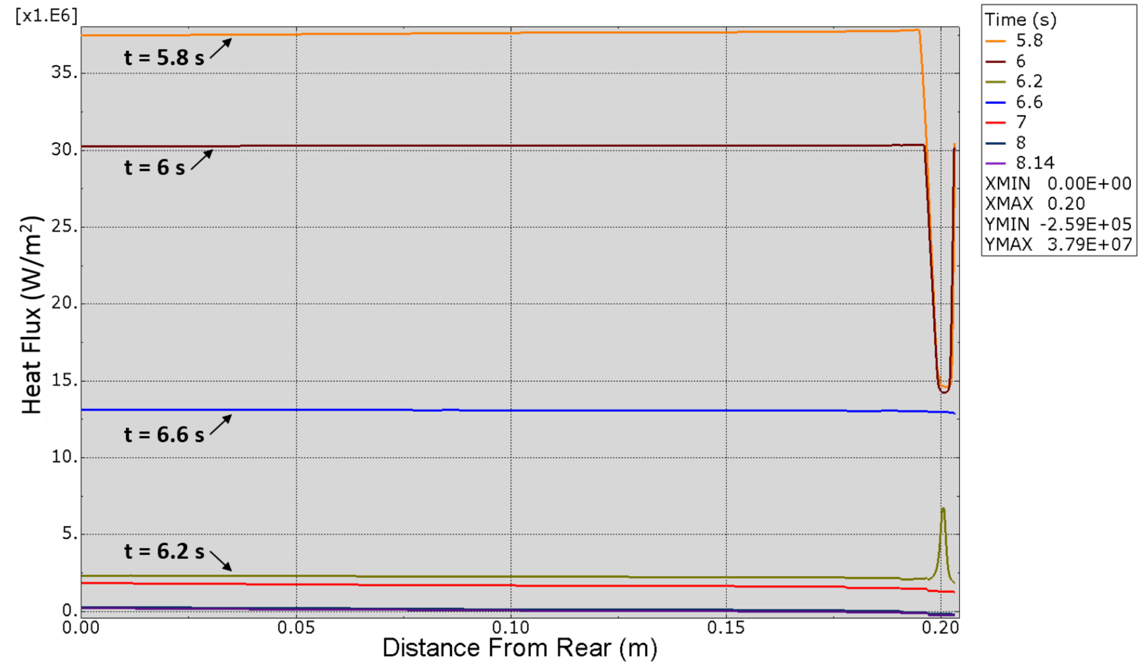

Figure 83: Bottom Surface Heat Flux, $t = 5.8$ to 8.14 seconds.

Figures 84 and 85 show variation of heat flux along the top surface of the slipper with respect to time. On the top surface of the slipper, negative heat flux loads are into the slipper and positive heat flux is out of the slipper.

The heat flux curve for the first 5.4 seconds of the run, seen in Fig. 84, are negative and are generally increasing in magnitude, indicating convective aerodynamic heating is greater the sled accelerates. The step variations along each curve are due to the segmented application of the film coefficient over the top surface. The ramp variations in each step are a result of: (1) elevated temperatures due convective heating at the front surface and (2) elevated temperatures in the neighboring region (closer to the leading edge) due to larger heat transfer coefficient in that region.

Heat flux distributions along the top surface for $t \geq 5.4$ seconds are shown in Fig. 85. The sled is decelerating and the adiabatic wall film temperature is decreasing so the heat flux into the slipper is decreasing. At $t = 6$ seconds, the heat flux at the leading edge takes on a positive value indicating heat flux out of the slipper. For $t \geq 6$ seconds, the region of positive heat flux (out of the slipper) increases in size. At $t = 8$ seconds, the heat flux is positive over the entire surface of the slipper.

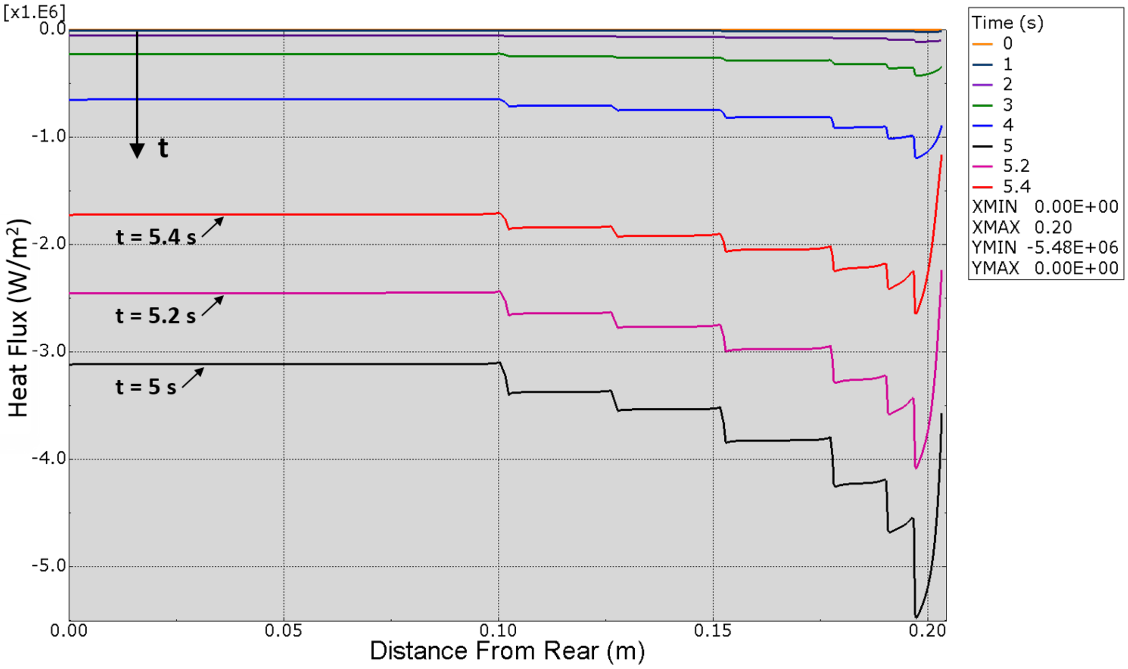

Figure 84: Top Surface Heat Flux, $t = 0$ to 5.4 seconds.

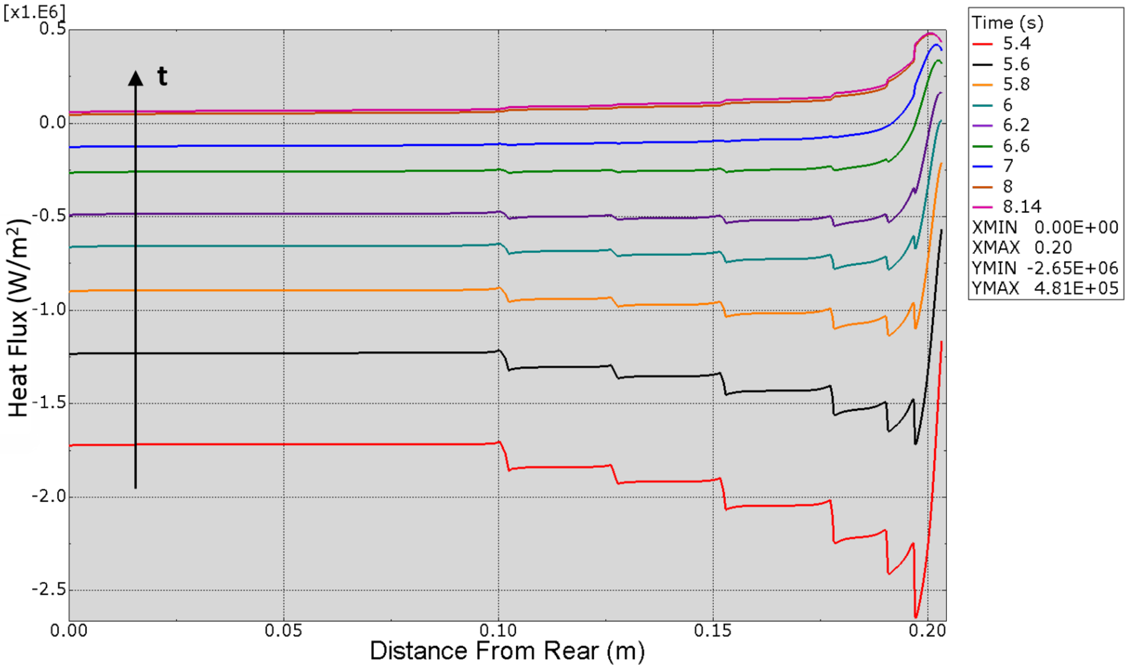

Figure 85: Top Surface Heat Flux, $t = 5.4$ to 8.14 seconds.

5.3.4 Two-Dimensional Heat Flux Vector Plots

Heat flux, due to loads applied along the surfaces, propagates into the slipper as test run progresses. The applied heat fluxes interact with one another in each element of the model and resultant heat flux vectors (magnitude and direction) develop. Heat flux is calculated at each node for each time step. Resultant heat flux vector plots are presented for selected time steps in Fig. 86 through Fig. 93.

The heat flux vectors vary in both size and color corresponding to magnitude. For example, small magnitude heat flux vectors are illustrated with small blue arrows and large magnitudes are shown with large red arrows. The arrow indicates the direction of the heat flux vector. The scale is the same for all vector plots in order to facilitate comparison of vector magnitudes over the course of the run. The coarsest mesh (Model 4) is employed to show vectors at the fewest representative locations. The dimensions of each figure is $H = 14.7$ mm by $L = 25.4$ mm. (These are the same dimensions as the two-dimensional leading edge temperature contour figures in Sec. 5.3.2). Multiple vectors originating from a single node are resultant heat flux vectors calculated in adjacent elements. Use of a finer mesh resolves these inter-element heat flux discrepancies.

The heat flux vector plot at $t = 4.0$ seconds (shown in Fig. 86), shows resultant vectors due to the small magnitude (compared to later in the run) heat fluxes on all three sides. At this point, the vector magnitudes are comparable on the top and the front of the slipper. The vector magnitudes are larger along the bottom of the slipper, with the largest magnitude vectors occurring at the leading edge. In the corners of the slipper, the vectors are clearly resultant vectors due to the combination of heat fluxes on the adjacent sides. On all sides, the heat flux vectors are directed into the slipper indicating heating.

At $t = 4.5$ seconds (Fig. 87), the vector distribution is similar to the distribution at $t = 4$ seconds. The heat flux on the top and front surfaces are similar in size, but the heat flux on the bottom surface is now much larger, by comparison.

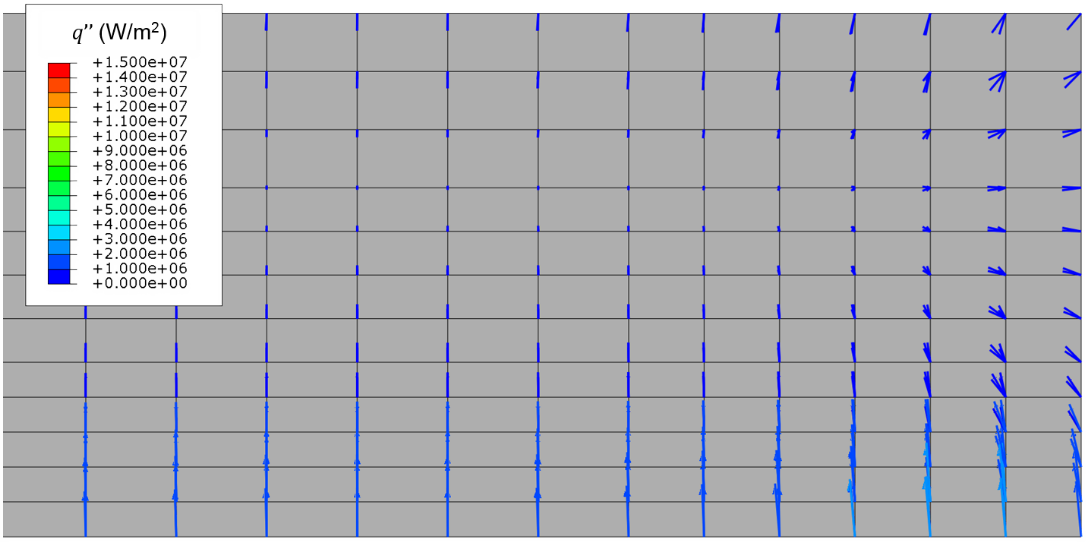

Figure 86: Heat Flux Vectors, Slipper Leading Edge, t = 4.00 seconds.

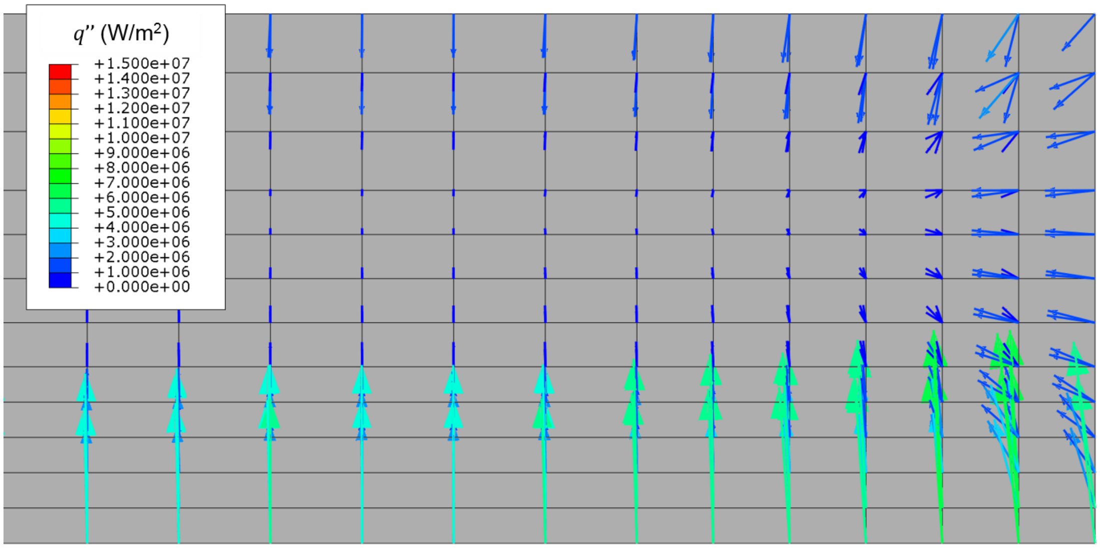

Figure 87: Heat Flux Vectors, Slipper Leading Edge, t = 4.50 seconds.

At $t = 5$ seconds (Fig. 88), the heat flux vectors are much larger on the bottom than the heat flux vectors are on the front or on the top surfaces. The sled is nearing its maximum velocity and the conductive frictional heating is much larger than it was in in the earlier distributions.

At $t = 5.2$ seconds (Fig. 89), the magnitude of the heat flux on the bottom surface has reached a maximum. The red arrows indicate the maximum heat flux in the slipper is seen near the leading edge. The large magnitude is due to the combination of the greatest conductive heating coupled with the greatest convective heating seen in the entire run.

At $t = 5.6$ seconds (Fig. 90), the sled is decelerating so the convective heat loads are smaller on the top and on the front of the slipper than in previous plots. Additionally, the conductive loads on the bottom are smaller because the combination of downward force and horizontal sled velocity is smaller. At this point, the resultant heat flux load vector in the bottom corner at the leading edge is directed straight up. Before $t = 5.6$ seconds, this vector had a horizontal component into the slipper. The direction of this vector indicates heating upward into the slipper, but the horizontal component is transitioning from heating (Fig. 89) to cooling (Fig. 91) the slipper. The zero horizontal component indicates that, at this point, this corner of the slipper is the same temperature as the total temperature on the front of the slipper.

At $t = 6$ seconds (Fig. 91), the magnitudes of the heat fluxes on the front and top surfaces continue to shrink. The heat flux magnitudes on the bottom surface are much larger than the heat fluxes on the top and front. The heat flux in the bottom corner on the leading edge has transitioned from heating to cooling the slipper. The temperature of the slipper at this point is greater than the total temperature in the film on the front surface. At this time, the convective heat flux only cools this portion of the front surface due to the elevated slipper temperature that results from the frictional heating on the bottom of the slipper.

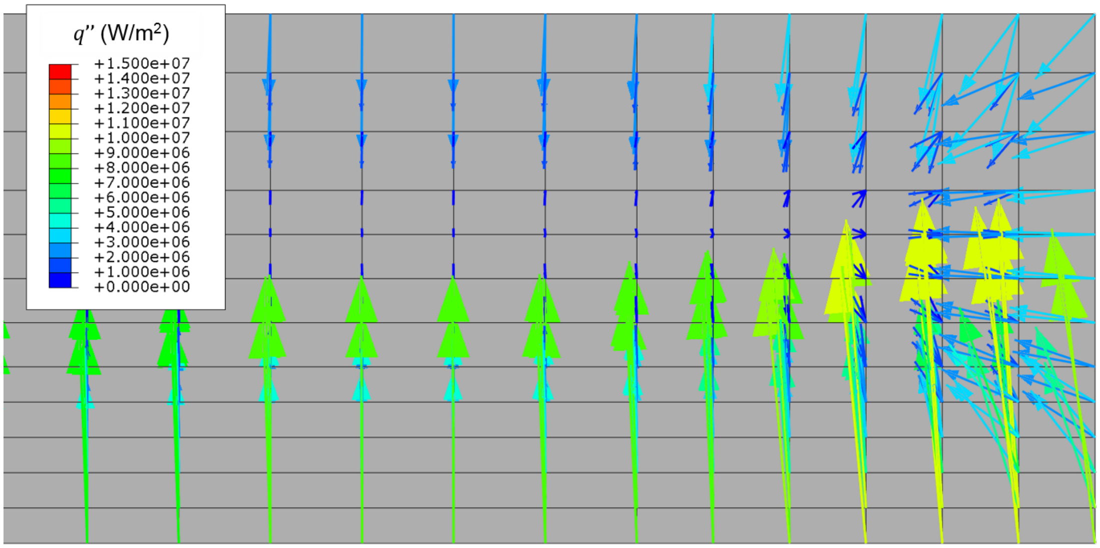

Figure 88: Heat Flux Vectors, Slipper Leading Edge, $t = 5.00$ seconds.

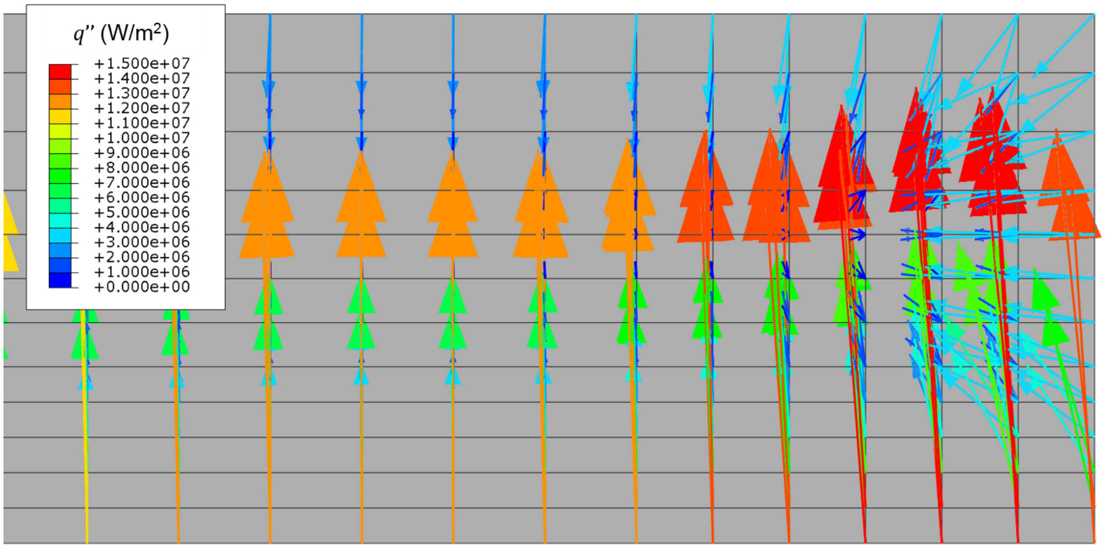

Figure 89: Heat Flux Vectors, Slipper Leading Edge, $t = 5.20$ seconds.

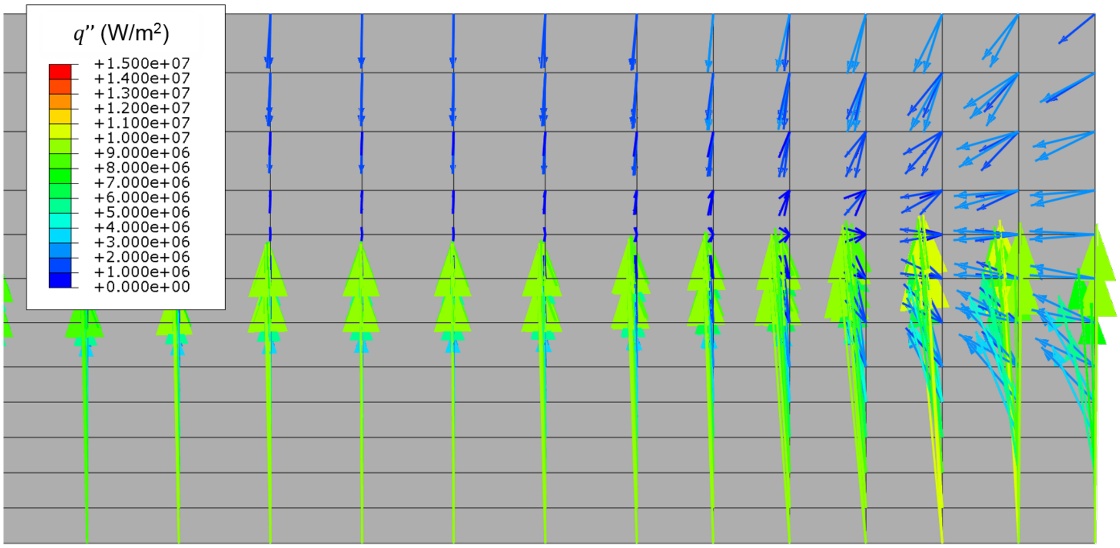

Figure 90: Heat Flux Vectors, Slipper Leading Edge, $t = 5.60$ seconds.

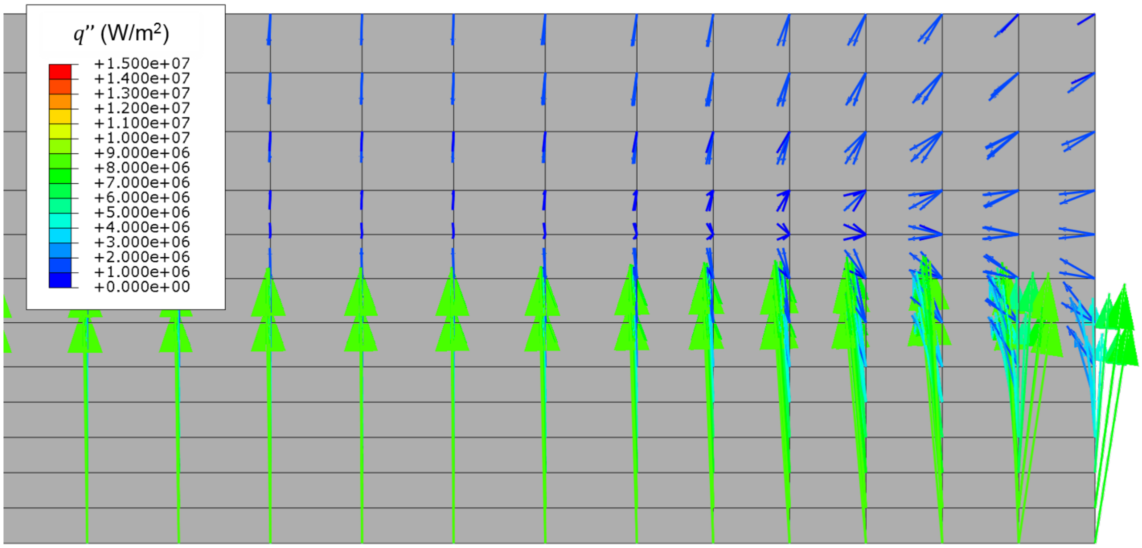

Figure 91: Heat Flux Vectors, Slipper Leading Edge, $t = 6.00$ seconds.

Figures 92 and 93 show heat flux vector plots at $t = 7$ seconds and $t = 8.14$ seconds, respectively. At $t = 7$ seconds, the general distribution is similar to the distribution seen at $t = 6$ seconds (Fig. 91). The magnitudes of the vectors are generally smaller. The horizontal component of heat flux at the leading edge of the slipper is now much larger than it had been. Additionally, the horizontal component of the heat flux vector is directed outward from the slipper up to the slipper mid-height indicating convective cooling in this region. Above the midpoint of the leading edge, the heat flux vectors are almost too small to plot on this scale because there is minimal heat flow in this region of the slipper. At the top of the leading edge and along the the top surface near the leading edge, small outward-directed vectors indicate the heat flux from the film on the top surface near the front of the slipper has transitioned from heating to cooling the slipper. The largest heat fluxes are seen on the interior of the slipper, upwards from the bottom edge and away from the front. The maximum magnitude here is due to the continued propagation into the slipper of the large applied heat fluxes on the bottom. Heat fluxes on the bottom are smaller due to the convective aerodynamic cooling seen by the slowing slipper.

At the end of the run ($t = 8.14$ seconds, Fig. 93), the slipper has decelerated to the smallest velocity for which DADS data exists. At this point, the heat flux vectors are smaller over the entire slipper section presented than they had been previously. Convective cooling effects now dominate the front surface of the slipper and are larger in magnitude and cover a larger section of the top surface. For the first time, the vertical components of every heat flux vector is in the upward direction (heating on the bottom and cooling on the top). The large heat fluxes applied to the bottom surface continue to raise the temperature of the interior of the slipper.

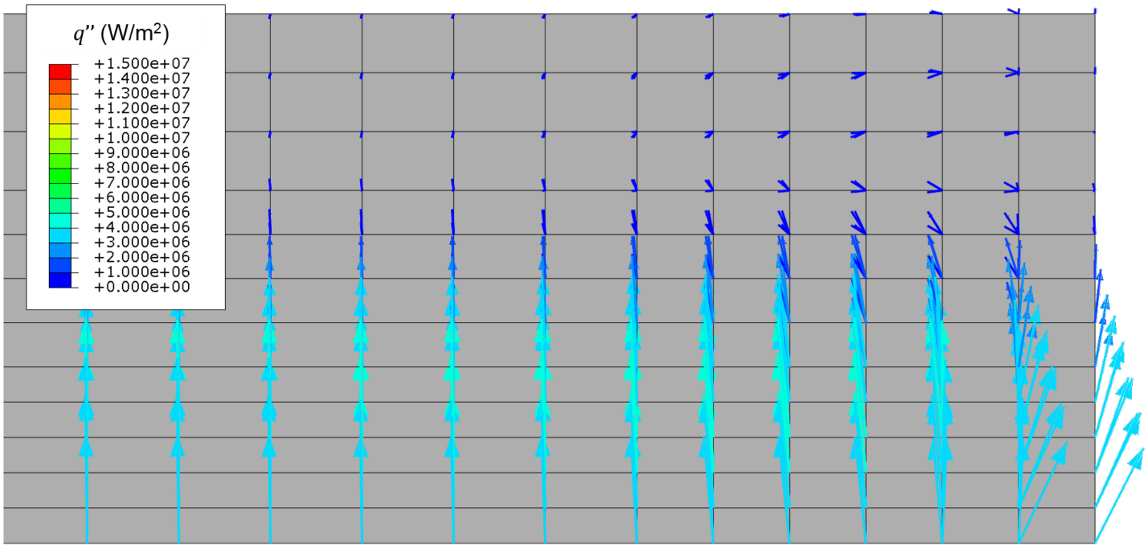

Figure 92: Heat Flux Vectors, Slipper Leading Edge, t = 7.00 seconds.

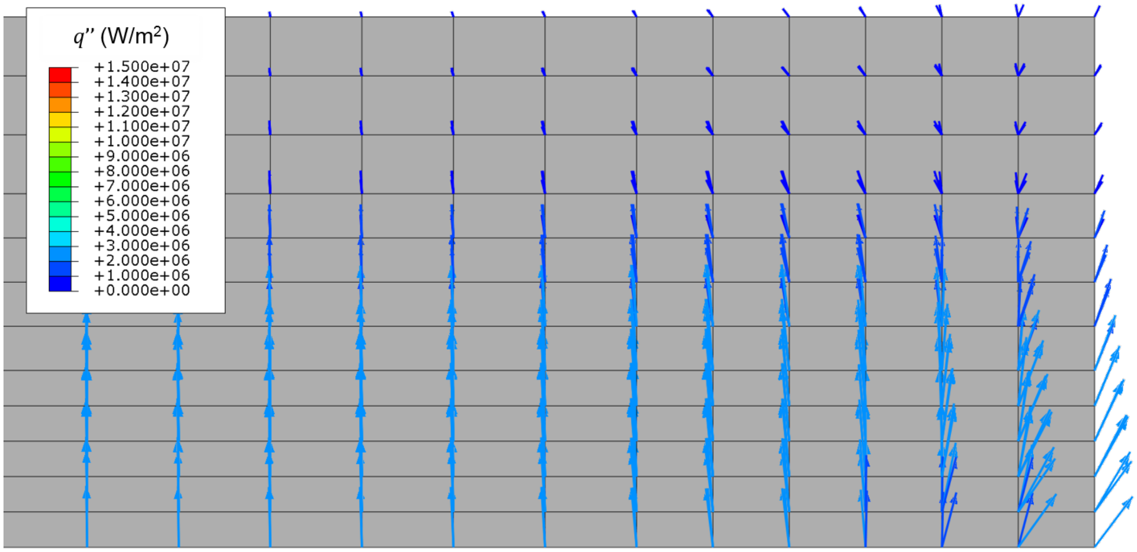

Figure 93: Heat Flux Vectors, Slipper Leading Edge, t = 8.14 seconds.

5.3.5 Melt Estimation

For lack of a better alternative, the size of the melt wear region is estimated by counting the elements in the melted area in the temperature distributions. The two maximum melt areas occur at t = 5.38 and 5.64 seconds. Figures 94 shows the melted region at 5.38 seconds as a representative example.

The maximum temperature contour value was set at the VascoMax 300 melt temperature. Regions where temperatures exceed the melt temperature are grey in color.

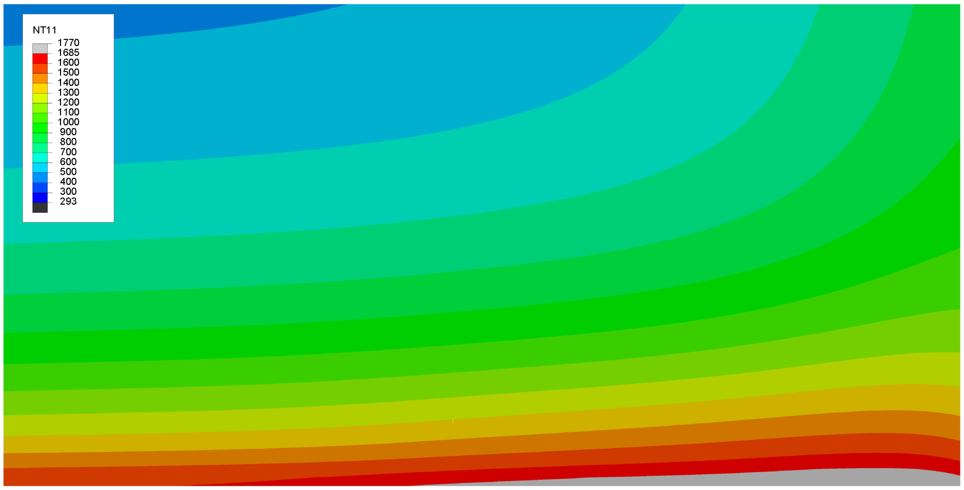

(a) Without Mesh

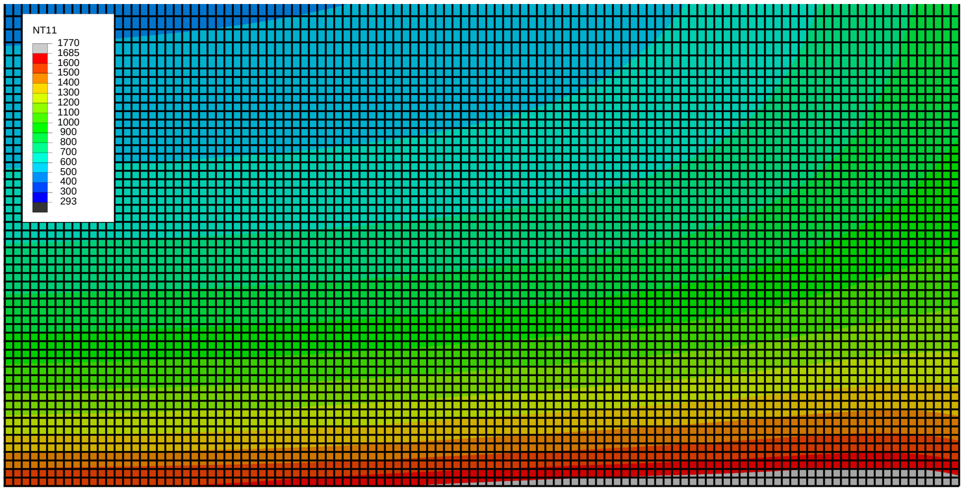

(b) With Mesh

Figure 94: Slipper Melt Region, t = 5.38 s.

Area of the melt region is estimated by using the mesh grid overlay to determine the size of the melted area. The melted area is then then multiplied by the width of the slipper to yield the estimated melt wear volume. Table 6, lists melt wear results for three models with different mesh sizes. Model 4 is not used for melt wear estimation due to the fact that the elements size is much larger than the melt region. The size of the estimated melt region is consistent over the three models examined.

Table 6: Melt Wear Estimation.

Model	Number of Elements	t = 5.38 s	t = 5.64s
1	41,584	83.4 mm^3	58.3 mm^3
2	25,600	90.8 mm^3	64.6 mm^3
3	17,920	85.3 mm^3	64.8 mm^3

Temperature distributions and melt regions are generally the same in the models listed in Table 6 regardless of the number of elements. The largest melt areas were seen in the temperature distributions at 5.38 and 5.64 seconds. There is overlap to these two areas but the smaller areas at 5.64 seconds are not subsets of the larger areas at 5.38 seconds. The actual total melt region is likely close to 100 mm^3.

5.4 Investigative Questions Answered

Aerodynamic heating had a significant effect on the temperature distribution in the slipper. Heating from the top surface encouraged the temperature increase initiated at the slipper / rail contact surface and generally made the majority of the slipper warmer than it would have been had aerodynamic heating not been taken into account. More interesting than that is the fact that the aerodynamic heating on the front surface was high enough to facilitate melt in the region at the front of the slipper when acting with the conductive heat on the bottom of the slipper. While the aerodynamic heating on the front of the slipper would not be sufficient to cause the slipper to melt, the presence of aerodynamic heating on the front certainly contributed to the heating and melt.

Refining the air properties to account for variation with temperature led to more credible results than could be created by using constant, reference temperature properties.

Variations due to the temperature increase and the normal shock produced reasonable input loads for the models. The fact that using these values eliminated melt wear at 100% surface contact is a positive aspect of the modeling. There should be no melt at a reference condition as melt wear does not necessarily occur in every test run

5.5 Summary

A sampling of results have been presented for the finite difference and finite element models. Due to the nature of the models, direct comparison of results is not possible. The finite difference model results were limited to calculated melt wear for the four partition functions at a fixed point for a range of contact percentages. Representative temperature and heat flux distributions have been presented and discussed for the finite element model. Melt wear estimations based on the displayed melted area were given.

6 Conclusions and Recommendations

6.1 Chapter Overview

The final chapter of the thesis reports conclusions and observations derived from the completion of this research.

6.2 Conclusions of Research

Countless factors influence wear in the slipper: contact time, contact area, speed, pressure, and heat flux partition are just a few. To say unequivocally that melt will or will not occur in a planned test run is fallacy. Results were presented here for models that predicted a small amount of wear, but changing the inputs to the model (such as loading, contact time, material properties, heat flux coefficients) could lead to significantly more melt wear or no melt at all.

Refinements made to the existing one-dimensional finite difference model improved the accuracy of the calculated bottom surface temperature. In past research [26], the temperature and heat transfer coefficient of the air in the gap between the slipper and the rail were assumed constant, $T = 1{,}000$ K and $h = 100$ W/(m^2-K), respectively. In reality, the temperature in the gap varies significantly (from 293 K to 1,400 K) over the course of the run. Increasing gap air temperature has the effect of increasing both the viscosity and thermal conductivity of the air in the gap which leads to great variation in the calculated heat transfer coefficient on the bottom surface of the slipper. Appropriate variation of the temperature and heat transfer coefficient, leads to more accurate calculation of convective heat flux into and out of the bottom surface of the slipper. When these changes are applied to the finite difference model, the calculated surface temperatures are lower and no melt occurs.

The heat flux partition functions employed in previous research [26] need to be revisited. The partition functions were selected because they yielded reasonable predictions of melt wear when applied to the finite difference model. [26] With the refined gap temperature and air properties, melt does not occur in slipper regardless of employed partition function. Under the assumption that some degree of melt necessarily occurs in the slipper, more heat from sliding friction must be applied to the surface of the slipper over the course of the run. An increase of applied heat flux could be modeled through a new or adapted partition function.

The finite difference model provides a good approximation for the temperature on the bottom of the slipper. Using the finite difference calculated surface temperature allowed for more accurate calculation of the film temperature on the bottom surface of the slipper and, therefore, more accurate heat flux loading and temperature distribution calculation by finite element model than could be applied without an externally calculated surface temperature. Unfortunately, the temperature distributions calculated by the two models are not the same. In the future, perhaps the differences could be resolved through implementation of an iterative finite element model that may or may not use the surface temperature calculated by the finite difference model as an initial value.

While the finite difference scheme does calculate reasonable temperatures on the bottom surface of the slipper, the scheme does not account for the heat effects on the other surfaces. The combination of the convective aerodynamic effects applied to the front, top, and bottom surfaces of the finite element model produced temperature distributions in the slipper that cannot be predicted by using the finite difference scheme.

Also, with respect to the finite difference model, the assumption that the slipper temperature remains constant above a predefined diffusivity depth is not realistic. As seen in the results obtained using the finite element model, heat flux due to both conduction and convection applied to the bottom of the slipper would propagate deeper into the slipper than the constant temperature diffusion depth allows. Additionally, convective aerodynamic heating on the top surface of the slipper further increases the internal slipper temperature above the ambient temperature.

Application of the convective aerodynamic effects to the two-dimensional finite element model allowed for determination of more complete temperature distribution in the slipper than the one-dimensional finite difference model permits. Temperature variation in the slipper is a result of heat flux loads and boundary conditions on the front, top, and bottom surfaces of the slipper. Further, variation of the the film condition along the top surface (by varying the heat transfer coefficient) and variation of the heat flux load on the bottom (taking into account the three heat flux regions described by Korkegi and Briggs [24]) yielded temperature distributions which vary realistically along the top and bottom surfaces.

Aerodynamic heating on the front and bottom surfaces of the slipper encourages melt. As seen in the Finite Element Results and Melt Estimation sections, slipper melt only occurs on the bottom of the slipper in the small region near the leading edge. The conductive heat flux due to sliding friction is applied uniformly across the bottom of the slipper, and while the conductive heat flux is the largest magnitude heat flux encountered by the slipper, the conductive heat flux alone is not strong enough to increase the slipper temperature beyond the melt temperature. The slipper temperature near the bottom of the leading edge, is increased beyond the conductive heat effect by the aerodynamic heating on the front and the largest magnitude convective heat flux seen on the bottom of the slipper. Again, the convective heat flux on the bottom of the slipper has a maximum value at the leading edge and a minimum value at the rear of slipper resulting from the transition from the boundary layer region at the front to the Couette region at the rear of the slipper.

The finite element model does not sufficiently model melt wear characteristics. The finite element model developed in Abaqus does not allow for element removal due to melt or heat flux load reapplication. Melted material is retained by the model when, in reality, the regions of the material which exceed the melt temperature should be removed from the slipper. Further, when the melted material is removed from the slipper, a new bottom surface area would be created in this region. This new surface would undergo conductive and convective heat flux similar to the loads and boundary conditions applied to the rest of the bottom surface. As developed, the melted region remains in the model, accepts the conductive and convective heat fluxes, and transfers the stored energy to the surrounding solid region of the slipper. Further, as the sled slows and the slipper cools due to convection, the melted region resolidifies and behaves as solid material for the remainder of the run. The melt behavior modeled in this research is not realistic and should be improved upon in future research efforts.

The stand-alone thermal model does not adequately describe the slipper / rail contact interaction. The primary goal of this research was to develop a model of the slipper that considered the effects of conductive and convective heat flux. In reality, mechanical wear would remove slipper material leading to non-uniform heat flux loads application across the slipper surface. Further, the increased slipper temperatures would lead to material softening and facilitate mechanical wear. In other words, thermal and mechanical effects are interdependent and should be both be considered in unified, thermomechanical models in future research efforts.

6.3 Significance of Research

Past slipper wear research focused primarily on mechanical wear and considered the thermal influence as secondary or disregarded it altogether. This research took a new and unique perspective and considered the aerodynamic heating and thermal effects. This analysis of the slipper problem may be applied to future slipper wear research as either a companion to a study in mechanical wear or a foundation to a deeper analysis of the thermal and aerodynamic effects on the slipper.

6.4 Recommendations for Action

Data collection in and around a real world slipper taken during a test run would create a better understanding of the conditions that actually occur in the region. Placing thermocouples within the slipper material to take measurements during the test run could be used to validate or refute the work done for this thesis. Further, real world temperature data could be used to identify the partition function relationship to enable better prediction of the rate of heating and temperature change in the slipper.

In order to reduce or eliminate the effects of aerodynamic heating on the slipper, aerodynamic shielding should be employed to keep the high temperature, high pressure air flow away from the gap. Shielding may be set in front of the slipper to absorb heat and direct air around the sled and away from the front surface and the gap.

6.5 Recommendations for Future Research

A number of assumptions were discussed in Chapter 1. Each simplifying assumption decreases the reliability of the predictions made here.

The airflow and geometric assumptions made to establish heat transfer coefficients are reasonable, but are perhaps not as accurate as they could be. The top and bottom surfaces will not convect heat precisely as a flat plate would. The front surface of the slipper is not a cylinder. Further, these surfaces cannot be decoupled as they have been. The flow around the corners of the front surface would disturb the flow on the upper and lower surfaces. This interaction would lead to decreased convective effects near the leading edges of the horizontal surfaces. A thorough examination of the flow geometry in order to establish precise values for the heat transfer coefficients would allow for improved modeling of the slipper and a better prediction of melt wear.

The gap between the slipper and the rail during bounce has been modeled here as a step function. The maximum gap height is assumed to be the space between the slipper and the rail whenever they are not in contact. When the slipper and the rail are closer together than the maximum gap height, the boundary layers from the slipper and the rail would merge closer to the front of the slipper than was considered here. This would lead to a greater amount of cooling across the bottom of the slipper. Modeling the maximum gap height ($D = 3.175$ mm) is the worst case scenario from the heating perspective because more heat is lost in the regions where the boundary layers have mixed. Development of a model to account for gap height variation would be worthwhile.

Placing a single, normal shock in front of the slipper is an oversimplification of the flow in the neighborhood of the slipper. Lofthouse's [27] CFD analysis of the flow around the forebody of the sled did not consider the flow through the gap. A detailed, localized CFD analysis could provide insight into the airflow around the slipper.

Further, a coupled CFD / finite element model to study the effects of the slipper heating the air flow and the reciprocal heating of the slipper from the air could be insightful. The 0.2 ms time steps considered in this research are long enough that, at the speeds the slipper is traveling, the air particles under the slipper at one time step would be well behind the slipper at the next time step. But, in reality, the interaction is not discretized and a continuous flow past the slipper would reheat the surface of the slipper. Thus the cooling effects were likely overpredicted by a small amount in this study.

Heat flux due to friction at the interface between the slipper and the rail is the largest thermal load acting on any face of the slipper. The magnitude of the heat flux conducted into the bottom surface of the slipper over the course of the run drives the heating and melt wear in the slipper. Determination of an appropriate heat flux partition function will increase accuracy of predictive melt wear models. Additional studies focusing on partition function determination are required.

The actual motion of the slipper will not be the simple up and down bouncing motion as it is modeled here. The actual slipper will undergo yawing, pitching, and rolling motions. This motion is dependent on the numerous forces acting on the slipper. As the finite difference results show, the occurrence of melt is highly dependent on the size of the contact area between the slipper and the rail. Establishment of reliable contact percentage values, would allow for better prediction of slipper wear.

6.6 Summary

The purpose of wear analysis is to identify the wear modes influencing an interaction and determine which of these is the primary wear driver. The ideal wear model will account for the effects of all wear modes with the primary wear driver given proper weight as the dominant factor. In the case of the high speed sliding contact between the slipper and the rail, wear is generated from a combination of thermal and mechanical wear.

The focus on thermal heating and its effects on the slipper in isolation while ignoring the effects of mechanical wear is not realistic. But the lessons learned and the theory applied should be incorporated into future slipper wear research, whether the focus is melt wear, mechanical wear, or both.

Appendix 1

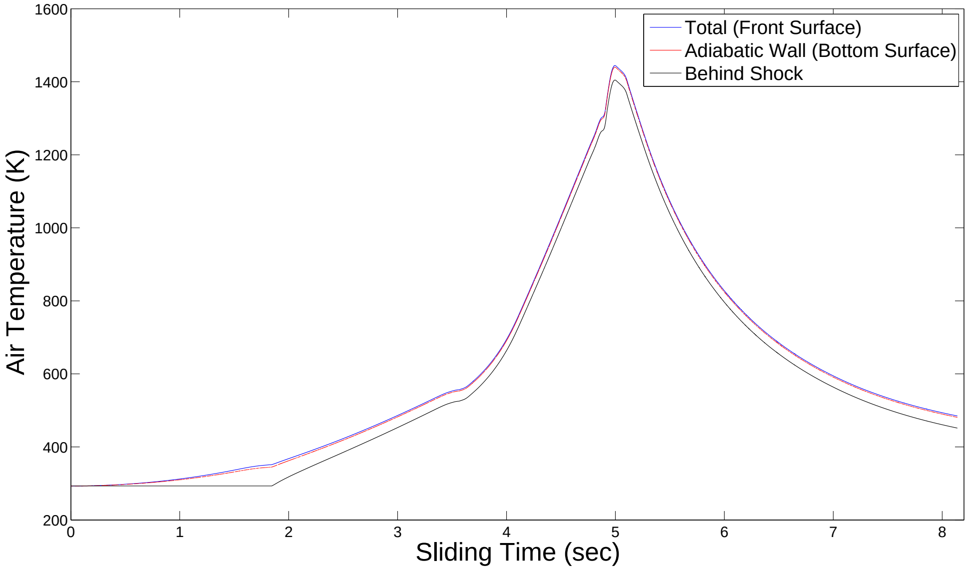

Figure 95: Post-Shock and Film Temperatures.

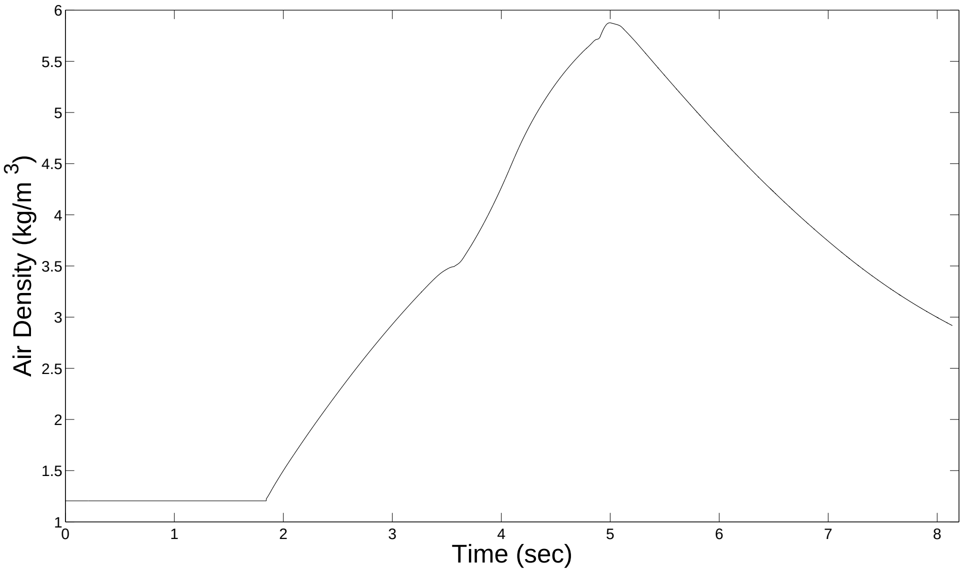

Figure 96: Air Density vs Time.

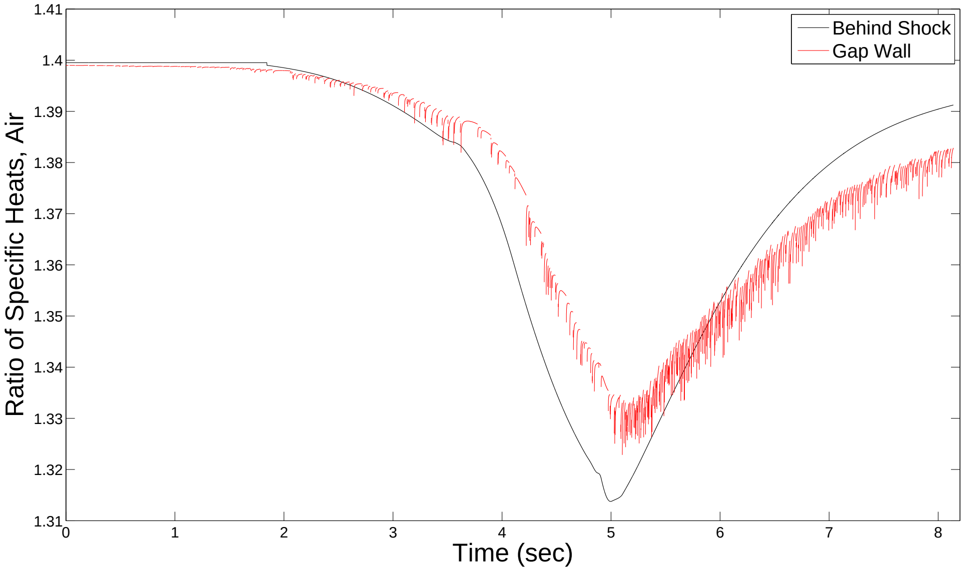

Figure 97: Ratio of Specific Heats, Air.

Appendix 2

MATLAB Code

```
% ONE-DIMENSIONAL SLIPPER TEMPERATURE GRADIENT ANALYSIS
% Original Finite Difference Code Written by Capt. Greg Cameron, MS-06.
% Adapted for DADS Analysis by LtCol Chad Hale, PhD-09.
% Modified by Stephen Meador, MS-10.
% Modified by Jacob Goldberg, PhD-10.
% Modified by Alexis Hurst, MS-11.
% Modified by Gracie Paek-Spidell, PhD-11.
% Modified by Kathleen Le, MS-13M.
% Modified by Christopher Alban, MS-14M.

tic
close all; clc;
% global Km Kr r z time Tmelt Tinit v_xi_t sigma thickness SlipPartition ...
    melt_wear cg_horiz
%%
% Load Data
dataDADS = load('DADS_Jan2008_alldata_refined');

time = DADS_Jan2008_noheader_alldata_refined(:,1);                  % (sec)
cg_horiz = DADS_Jan2008_noheader_alldata_refined(:,4)*.0254;        % horizontal ...
    distance (m)
vsled_horiz = DADS_Jan2008_noheader_alldata_refined(:,7)*.0254;     % horizontal ...
    velocity (m/s)
cgaccel_horiz = DADS_Jan2008_noheader_alldata_refined(:,10);        % horizontal ...
    acceleration (m/s^2)


%%
% Set Material Constants

% AIR CONSTANTS
cp_air = 1004;                                      % Specific heat, J/(kg K) for ...
    298K
gam_air = 1.3995;                                   % Ratio specific heats, Reference
R_air = 287.058;                                    % Specific gas constant, J/(kg*K)
```

```
k_air_ref = 0.0263;                                 % Thermal conductivity, ...
    Reference, W/m/K (at 300K)
p_air_ref = 101325;                                 % Pressure, Reference, ...
    kg/m/s^2 (at sea level)
mu_air_ref = 18.185e-6;                             % Dynamic Viscosity, ...
    Reference, kg/m/s (at 293 K)
rho_air_ref = 1.225;                                % Density, Reference, kg/m^3 ...
    (at sea level)
nu = 1.343e-5;                                      % kinematic viscosity, m^2/s ...
    (at 293K)
theta_air = 5500/1.8;                               % Thermal constant, K
Pr = 0.695;                                         % Prandtl number, dimensionless

Tinit = 293;                                        % Initial slipper, rail, and ...
    freestream temperature, K
soundSpeedAir = sqrt(gam_air*R_air*Tinit);          % Speed of sound, sea level, ...
    273K, m/s

% Slipper Constants
% Slipper Geometry
Sw = 4*0.0254;                                      % Width, m
Sl = 8*0.0254;                                      % Length, m (0.2032 m)
An = Sw * Sl;                                       % Area, m^2 ( = 32 sq in)
thickness = 14.7E-3;                                % Thickness, m (14.7 mm)
vol = An * thickness;                               % Volume, m^3

% Slipper Material Properties
rho_V300 = 8000;                                    % Density, kg/m^3
Cp_V300 = 858.3;                                    % Specific heat (J/kg K), at ...
    700K  (Le used 420)
Tmelt = 1685;                                       % V300 melt temperature (K)
L_VM300 = 272e3;                                    % Latent heat of fusion (J/kg)
Km = 30.807;                                        % Thermal conductivity, J/(m ...
    s K) = W/(m K), at 700K (Le used Km = 31)
alpha = Km/(rho_V300 * Cp_V300);                    % Thermal diffusivity, m^2/s

g = 9.81;                                           % acceleration due to ...
    gravity, m^2/s

vsled_horiz = abs(vsled_horiz);
Mach = vsled_horiz./soundSpeedAir;
```

```
Mach(1) = 1e-12;

% Temporal discretization
N = length(time);                                   % Number of time steps
dt = time(2)- time(1);                              % Time step duration

% Normal Shock Effect on Flow Properties
% Array Initialization
T2 = zeros(1,N);
gam2 = zeros(1,N);
M2 = zeros(1,N);
rho2 = zeros(1,N);
v2 = zeros(1,N);
vgapkb = zeros(1,N);

% Shock effect calculations
for ct = 1:N
    if Mach(ct) ≤ 1
        T2(ct) = Tinit;
        gam2(ct) = gam_air;
        M2(ct) = Mach(ct);
        rho2(ct) = (p_air_ref/R_air)*(T2(ct))^(-1);
        v2(ct) = vsled_horiz(ct);
        vgapkb(ct) = vsled_horiz(ct);
    elseif Mach(ct) > 1
        T2(ct) = Tinit*(1+(2*gam_air/(gam_air+1))*(Mach(ct)^2-1))* ...
            ((2+(gam_air-1)*Mach(ct)^2)/((gam_air+1)*Mach(ct)^2));
        M2(ct) = ...
            sqrt((1+((gam_air-1)/2)*Mach(ct)^2)/(gam_air*Mach(ct)^2-(gam_air-1)/2));
        rho2(ct) = rho_air_ref*(gam_air+1)*Mach(ct)^2/(2+(gam_air-1)*Mach(ct)^2);
        v2(ct) = vsled_horiz(ct)*(2+(gam_air-1)*Mach(ct)^2)/((gam_air+1)*Mach(ct)^2);
        vgapkb(ct) = ...
            vsled_horiz(ct)*(((gam_air-1)/(gam_air+1))^(1/2)*(1+2/(gam_air-1)*Mach(ct)^(-2))^(1/2));
        gam2(ct) = 1 + (gam_air - 1) / ( 1 + (gam_air-1) * ((theta_air/T2(ct))^2 ...
            * exp(theta_air/T2(ct)) /(exp(theta_air/T2(ct)) -1)^2));
    end
end

% % Calculation of velocity in gap boundary layer
% % Assumes air flow speed as determined by Korkegi and Briggs (Eq 2)
vgap = vgapkb;
```

```

% Reference distance x (along slipper length) for calculation of Reynolds Number
x = Sl*0.420448913383;                              % Percentage calculated by ...
    evaluating half integral size of h(x)
% x = 0.525*Sl;                                     % Boudary Layer Mergence Location


%%
% Original Code Written by Gracie Paek-Spidell, Ph.D Advanced Candadicy, PhD-11.
% Analytical solution to partion function
% Function code in separate .m file alpha2.m
% alp2=alpha2(r,z);

%%

slideCont = 1;                                      % percentage of slipper in ...
    contact while sliding (geometric)

% clear slideCont
% clear TotalMeltWear
% clear TotalMeltVol
% clear MaxHeatFlux
% slideCont(1) = 0.3;                               % WHEN USING THIS, END LOOP BELOW
% for int = 1:14


% Partition Function

% Exponential Function
SlipPartition = exp((-time.^2)*5)*.4+.1;

% Pavg = 2.275e6;
% % Pavg = 7.2669e4;                                  % Mean pressure load with zeros
% mu = 0.2;                                           % Mean coefficient of ...
    friction (Le used 0.2)
% k = 4.4866e-6;                                      % Same as alpha above, (Le ...
    used 4.5e-6)
% kappa = 30.807;                                     % Slipper thermal ...
    conductivity, same as Km above
% part_0 = .5;                                        % Inital partition, no units
% part_m = .1;                                        % Final partition, no units
```

```
% partition = (part_0 + part_m)/2;                    % Linear partition ...
    function, no units
%
% v0 = 714.2125;                                      % Mean sled velocity, m/s
% tm = pi/k*((Tmelt-Tinit)*kappa/(2*mu*partition*Pavg*v0))^2;
%
% percentcontact = 0.225;
% constant = 1/percentcontact;
% v0 = 0;
% accel = 305.956343;                                 % m/s^2
% lambda = 3*(Tmelt-Tinit)*kappa/(2*partition*Pavg*accel)*sqrt(pi/k)*1/mu;
% beta = 3*v0/accel;
% M = 4*beta^3/(27*lambda^2);
% s = (lambda/2)^(1/3)*((sqrt(1+M)+1)^(1/3)-(sqrt(1+M)-1)^1/3);
% %tm = s^2;
%
% for j = 1:size(time);
%     if time(j) < constant*tm;
% % Bilinear Partition Function
%       SlipPartition(j) = part_0+(part_m-part_0)*(time(j)/(constant*tm));
% % Power Partition Function
% %        SlipPartition(j) = part_0*(part_m/part_0)^(time(j)/(constant*tm));
% % Power Squared Partition Function
% %      SlipPartition(j) = part_0*(part_m/part_0)^((time(j)^2/(constant*tm)^2));
%     else time(j) > constant*tm;
%         SlipPartition(j) = part_m;
%     end
% end

%%
% Contact force between bottom of slipper/top of rail (N)
force_data= (DADS_Jan2008_noheader_alldata_refined(:,46) + ...
    DADS_Jan2008_noheader_alldata_refined(:,47))*4.448;

P = force_data./(An*slideCont);                     % Slipper/Rail Pressure (Pa)
% P = force_data./(An*slideCont(int));               % Slipper/Rail Pressure (Pa)
PV = (P*10^-6).*(vsled_horiz*1000);                 % Used to find Montgomery's ...
    COF (MPa*mm/s)

% Calculation of Montgomery's COF
COF = zeros(length(PV),1);
```

```
for index = 1:length(COF)
    if PV(index) < eps
        COF(index) = 0;
    elseif PV(index) < 4.45e8
        COF(index) = 0.2696*exp(-3.409e-7*PV(index))+0.3074*exp(-6.08e-9*PV(index));
    else
        COF(index) = 0.02;
    end
end

% Calculate Frictional Heating (Heat Flux)
HeatFlux = SlipPartition.*P.*vsled_horiz.*COF;      % (Watts/m^2), Varies with ...
    DADS velocity
HeatFluxTotal = P.*vsled_horiz.*COF;

% f = 6.4969e+004;
% g = 0.6720;
% FrictHeat = f*exp(g*time);
% HeatFlux = SlipPartition .* FrictHeat/An;
% HeatFlux = SlipPartition'.*P.*max(vsled_horiz)/2.*COF;      % (Watts/m^2), ...
    Linear acceleration
% HeatFlux = SlipPartition.*P.*max(vsled_horiz).*COF;         % (Watts/m^2), ...
    Constant max velocity

% % Calculate Temperature Profiles Using Finite Difference Method
% Spatial discretization
M = 100;                                            % Number of spatial steps ...
    (through slipper thickness)
dxi = 1/M;                                          % Spatial step size
xi = (0:dxi:1);                                     % Array
ystar = sqrt(alpha*time(end));                      % Diffusivity Length

% Conduction/Convection Switch Function
m = sign(force_data);                               % Switch function, varies ...
    with DADS force data
% m = ones(40701,1);                                % Switch function, constant ...
    contact

% Air Thermal Conductivity Polynomial Coefficients
p = ...
    [6.566773861675003e-12,-3.041917353372259e-08,8.301215399884204e-05,0.016244464406121];
```

```

% Value initialization
v_xi_t = zeros(length(xi),N);
sigma = zeros(1,N);
sigmadot = zeros(1,N);
g_t = zeros(length(xi),N);

% Array initialization
Tawb = zeros(1,N);
Tawb(1) = Tinit;
Tfab = zeros(size(time));
Tfab(1) = Tinit;
Ts = zeros(1,N);
Ts(1) = Tinit;
Tfb = zeros(1,N);
Tfb(1) = Tinit;
Trefb = zeros(1,N);
Trefb(1) = Tinit;
k_air = zeros(1,N);
k_air(1) = k_air_ref;
k_airp = zeros(1,N);
k_airp(1) = k_air_ref;
ReB(1) = abs(vgap(1)*x/nu);
h = zeros(1,N);
h(1) = 0.0296*k_air_ref*ReB(1)^(4/5)*Pr^(1/3)/x;
rho_air = zeros(1,N);
rho_air(1) = p_air_ref/R_air/Tinit;
mu_air = zeros(1,N);
mu_air(1) = mu_air_ref;
nu_air = zeros(1,N);
nu_air(1) = nu;
gamgap = zeros(1,N);
gamgap(1) = gam_air;
speedsoundgap = zeros(1,N);
speedsoundgap(1) = sqrt(gamgap(1)*R_air*Tfb(1));
Mgap = zeros(1,N);
Mgap(1) = vgap(1) / speedsoundgap(1);
ReB = zeros(1,N);

g_t(1,1:2) =(2*dt*alpha)/(ystar*dxi*Km*(Tmelt-Tinit))* ...
    (m(1:2).*(HeatFlux(1:2))+(1-m(1:2))*(Tawb(1)-Ts(1))*h(1));
```

```
d = [-1; 0; 1];

% Calculations based on explicit solution.
v_xi_t(:,2) = g_t(:,1);

% Finite Difference Node 2 Initial Values
Ts(2) = (Tmelt - Tinit)*v_xi_t(1,2) + Tinit;
Tfab(2) = (Ts(2) + T2(2))/2;
Tfb(2) = T2(2);
Tawb(2) = Tfb(2)*(1 + (gam_air-1)/2 * Pr^(1/3) * M2(2)^2);
Trefb(2) = T2(2) + 0.5*(Ts(2) - T2(2)) + 0.22*(Tawb(2) - T2(2));
gamgap(2) = 1 + (gam_air - 1) / ( 1 + (gam_air-1) * ((theta_air/Tfb(2))^2 * ...
    exp(theta_air/Tfb(2)) /(exp(theta_air/Tfb(2)) -1)^2));
speedsoundgap(2) = sqrt(gamgap(2)*R_air*T2(2));
Mgap(2) = vgap(2) / speedsoundgap(2);
k_air(2) = k_air_ref*(Trefb(2)/300)^0.9;
k_airp(2) = polyval(p,Trefb(2)-175);
mu_air(2) = mu_air_ref*(Trefb(2)/Tinit)^(3/2)*(Tinit+110)/(Trefb(2)+110);
nu_air(2) = mu_air(2)/rho2(2);
ReB(2) = abs(vgap(2)*x/nu_air(2));
h(2) = 0.0296*k_air(2)*ReB(2)^(4/5)*Pr^(1/3)/x;

r = waitbar(0,'Please wait...');
% Finite Difference Iteration Scheme
for tn = 2:N-1
    B1(:,1) = [(alpha*dt/(ystar^2*dxi^2) - ...
        dt/(2*ystar*dxi)*sigmadot(tn))*ones(length(xi)-1,1) ; 0];
    B1(:,2) = [1-dt*(2*alpha/(ystar*dxi)^2+(2*alpha/(ystar*dxi)^2- ...
        sigmadot(tn)/(2*ystar*dxi))*((2*dxi*ystar*(1-m(tn)))/Km)*h(tn))   ;...
        (1 - 2*alpha*dt/(ystar^2*dxi^2))*ones(length(xi)-1,1)] ;
    B1(:,3) = [0 ; 2*alpha*dt/(ystar^2*dxi^2) ; ...
        (alpha*dt/(ystar^2*dxi^2) + ...
            dt/(2*ystar*dxi)*sigmadot(tn))*ones(length(xi)-2,1)];
    B = spdiags(B1,d,length(xi),length(xi));
    clear B1
    v_xi_t(:,tn+1) = B * v_xi_t(:,tn) + g_t(:,tn);
    clear B

    I = find(v_xi_t(:,tn+1)>1);
    chck = 1;
    while ¬isempty(I)
```

```
        if chck == 1
            delsig = .01*interp1(v_xi_t(:,tn+1),xi,1,'linear');
            chck = 2;
        end
        sigma(tn) = sigma(tn) + ystar*delsig;
        sigmadot(tn) = (sigma(tn) - sigma(tn-1))/dt;
    B1(:,1) = [(alpha*dt/(ystar^2*dxi^2) - ...
        dt/(2*ystar*dxi)*sigmadot(tn))*ones(length(xi)-1,1); 0];
    B1(:,2) = [1-dt*(2*alpha/(ystar*dxi)^2+(2*alpha/(ystar*dxi)^2- ...
        sigmadot(tn)/(2*ystar*dxi))*((2*dxi*ystar*(1-m(tn)))/Km)*h(tn))   ;...
        (1 - 2*alpha*dt/(ystar^2*dxi^2))*ones(length(xi)-1,1)];
    B1(:,3) = [0; 2*alpha*dt/(ystar^2*dxi^2);...
        (alpha*dt/(ystar^2*dxi^2) + ...
            dt/(2*ystar*dxi)*sigmadot(tn))*ones(length(xi)-2,1)];
    B = spdiags(B1,d,length(xi),length(xi));
        clear B1
        g_t(1,tn) = ...
            dt/(Km*(Tinit-Tmelt))*(sigmadot(tn)-2*alpha/(ystar*dxi))*(m(tn).*(HeatFlux(tn) ...
            - rho_V300*L_VM300*sigmadot(tn))+(1-m(tn))*(Tawb(tn)-Ts(tn))*h(tn));
        v_xi_t(:,tn+1) = B*v_xi_t(:,tn) + g_t(:,tn);
        clear I B
        I = find(v_xi_t(:,tn+1)>1);
    end

     Ts(tn+1) = (Tmelt - Tinit)*v_xi_t(1,tn+1) + Tinit;
     Tfab(tn+1) = (Ts(tn+1) + T2(tn+1))/2;
     Tfb(tn+1) = T2(tn+1);
     gamgap(tn+1) = 1 + (gam_air - 1) / ( 1 + (gam_air-1) * ...
         ((theta_air/Tfb(tn+1))^2 * exp(theta_air/Tfb(tn+1)) ...
         /(exp(theta_air/Tfb(tn+1)) -1)^2));
     Tawb(tn+1) = Tfb(tn+1)*(1 + (gamgap(tn+1)-1)/2 * Pr^(1/3) * M2(tn+1)^2);
     Trefb(tn+1) = Tfb(tn+1) + 0.5*(Ts(tn+1) - Tfb(tn+1)) + 0.22*(Tawb(tn+1) - ...
         Tfb(tn+1));
     speedsoundgap(tn+1) = sqrt(gamgap(tn+1)*R_air*Tfb(tn+1));
     Mgap(tn+1) = vgap(tn+1) / speedsoundgap(tn+1);
     k_airp(tn+1) = polyval(p,Trefb(tn+1)-175);
     mu_air(tn+1) = ...
         mu_air_ref*(Trefb(tn+1)/Tinit)^(3/2)*(Tinit+110)/(Trefb(tn+1)+110);
     nu_air(tn+1) = mu_air(tn+1)/rho2(tn+1);
     ReB(tn+1) = abs(vgap(tn+1)*x/nu_air(tn+1));
     h(tn+1) = 0.0296*k_airp(tn+1)*ReB(tn+1)^(4/5)*Pr^(1/3)/x;
```

```

    sigma(tn+1:end) = sigma(tn);
    g_t(1,tn+1) = (2*dt*alpha)/(ystar*dxi*Km*(Tmelt-Tinit))* ...
        (m(tn+1).*(HeatFlux(tn+1))+(1-m(tn+1))*(Tawb(tn+1)-Ts(tn+1))*h(tn+1));

    waitbar((tn-1)/(N-2),r)
end
close(r);

% Melt Result Calculation
T = (Tmelt - Tinit)*v_xi_t + Tinit;
melt_wear=(sigma/thickness*100);

% Display Total Melt Wear Results
WearVol = vol*10^9*(sigma/thickness);
TotalMeltWear = melt_wear(end)
TotalMeltVol = WearVol(end)
MaxHeatFlux = max(HeatFlux)

% % % % Close vary slide Cont Loop
% TotalMeltWear(int) = melt_wear(end)
% TotalMeltVol(int) = WearVol(end)
% MaxHeatFlux(int) = max(HeatFlux)
% slideCont(int+1) = slideCont(int) + 0.025;
% int
% end

% Calculation of flow parameters.
Nu_gap = x*h./k_airp;
St_gap = Nu_gap./ReB./Pr;
cR = h./vgap./rho2./St_gap;
cR2 = Pr.*k_airp./mu_air;
cpw = cp_air* (1 + ((gam_air - 1)/gam_air) * ((theta_air./Trefb).^2 .* ...
    exp(theta_air./Trefb) ./(exp(theta_air./Trefb) -1).^2));
cpc = cp_air* (1 + ((gam_air - 1)/gam_air) * ((theta_air./((Ts+T2)/2)).^2 .* ...
    exp(theta_air./((Ts+T2)/2)) ./(exp(theta_air./((Ts+T2)/2))-1).^2));
gam = 1 + (gam_air - 1) ./ ( 1 + (gam_air-1) * ((theta_air./Trefb).^2 .* ...
    exp(theta_air./Trefb) ./(exp(theta_air./Trefb) -1).^2));

% Calculation of Couette enthalpies.
hw = cpw.*Ts;
```

```
hc = cpc.*(Ts+T2)/2;

Cf = 0.074*ReB.^(-1/5);
mu_e = mu_air_ref.*((Ts+T2)/Tinit).^(3/2)*(Tinit+110)./((Ts+T2)+110);
ReR = abs((vsled_horiz'-vgap)*x.*rho2./mu_e);

% Array initialization
HeatLossBottom = zeros(size(time));
HeatFluxBottomkb = zeros(size(time));
gam = zeros(size(time));
delB = zeros(size(time));
delR = zeros(size(time));

vgap = (1-m).*vgap';
Mgap = (1-m).*Mgap';
h = (1-m).*h';
Tawb = (1-m).*Tawb';
Trefb = (1-m).*Trefb';
for c = 1:size(time)
      HeatLossBottom(c) = (1-m(c))*(Tawb(c)-Ts(c))*h(c);
      HeatFluxBottomkb(c) = ...
          (1-m(c))*(Cf(c)/2)*rho2(c)*vgapkb(c)*(vsled_horiz(c)^2)/2;
      gam(c) = (1-m(c))*(1 + (gam_air - 1) / ( 1 + (gam_air-1) * ...
          ((theta_air/Trefb(c))^2 .* exp(theta_air/Trefb(c)) ...
          ./(exp(theta_air/Trefb(c)) -1).^2)));
      if ReB(c) > 1e5
          delB(c) = (1-m(c))*0.37*(x)/(ReB(c))^(1/5);
      else
          delB(c) = 0;
      end
      if ReR(c) > 1e5
          delR(c) = (1-m(c))*0.37*(x)/(ReR(c))^(1/5);
      else
          delR(c) = 0;
      end
end
vgap(vgap==0)=NaN;
Tawb(Tawb==0)=NaN;
Trefb(Trefb==0)=NaN;
Mgap(Mgap==0)=NaN;
h(h==0)=NaN;
```

```
gam(gam==0)=NaN;
delB(delB==0)=NaN;
delR(delR==0)=NaN;
delM = delB + delR;

Cfc = 0.0018;
H = 0.003175/2;                      % half gap height, m ( = 1/8" / 2)
kseq = 0.00003;                      % equivalent sand roughness, m

ReC = vsled_horiz'*H./nu_air;
Tauw = rho2.*nu_air*vsled_horiz/2;
uT = sqrt(Tauw./rho2);
ksplus = kseq*uT./nu_air;
ReTau = uT * H ./nu_air;
Dtheta = 3.3007 + 1.827 - 0.87 * (8 + 2.1);

qckb = zeros(size(time));
qckb2 = zeros(size(time));
qckb3 = zeros(size(time));
qckb4 = zeros(size(time));

for c = 1:size(time)
    qckb(c) = (1-m(c))*0.5*Cfc*rho2(c)*(vsled_horiz(c)/2)^3;
    qckb2(c) = (1-m(c))*Cfc*rho2(c)*vsled_horiz(c)*cp_air*((Ts(c)+Tinit)/2-Ts(c))/2;
    qckb3(c) = (1-m(c))*Cfc*rho2(c)*vsled_horiz(c)*(hc(c)-hw(c))/2;
    qckb4(c) = (1-m(c))*Cfc*rho2(c)*vsled_horiz(c)^3/2;
end
qcm = (HeatLossBottom+qckb2)/2;

% % Top
Taw = T2.*(1 + (gam2-1)/2 * Pr^(1/3) .* M2.^2);
T_ref = (T2 + Taw)/2;
k_ref = polyval(p,T_ref-175);
mu_ref = mu_air_ref*(T_ref/Tinit).^(3/2)*(Tinit+110)./(T_ref+110);
nu_ref = mu_ref./rho2;
vtop = v2;
ReT = abs(vtop.*x.*(nu_ref).^(-1));
delT = zeros(size(time));
for c = 1:size(time)
      if ReT(c) > 1e5
          delT(c) = 0.37*(x)/(ReT(c))^(1/5);
```

```
      else
          delT(c) = 0;
      end
end
ht = 0.0296*k_ref.*ReT.^(4/5)*Pr^(1/3)/x;
delT(delT==0)=NaN;

% % Front
D = thickness;
Ttot = T2.*(1 + (gam2-1)/2 .* M2.^2);
T_film = (Ttot + T2)/2;
k_film = polyval(p,T_film-175);
mu_film = mu_air_ref*(T_film/Tinit).^(3/2)*(Tinit+110)./(T_film+110);
nu_film = mu_film./rho2;
vfront = v2;
ReD = abs(vfront.*D.*(nu_film).^(-1));
for c = 1:N
    hf(c) = m(c)*k_film(c)*sqrt(rho2(c)*vsled_horiz(c)/D/2/mu_film(c)) + (1- ...
        m(c))*k_film(c)*sqrt(rho2(c)*vsled_horiz(c)/D/mu_film(c));
end

ht = ht';
Taw = Taw';
hf = hf';
Ttot = Ttot';

% % % Write output loads / amplitudes to excel file for ABAQUS input
header = {'time','Conduction','BLConv','CouetteConv','Taw','Ttot','hf','ht'};
b=[time,HeatFlux,HeatLossBottom,qckb3,Taw,Ttot,hf,ht];
c = [header;num2cell(b)];
xlswrite('AbaqusLoads',c);
```

Bibliography

1. *18 Per Cent Nickel Maraging Steels: Engineering Properties.* Publication No. 4419, Nickel Development Institute, 1976.
2. *Abaqus Analysis User's Manual.* Dassault Systemes, Providence, RI, 2011.
3. Anderson, John D. Jr. *Fundamentals of Aerodynamics.* McGraw Hill, New York, 2011.
4. Anderson, John D. Jr. *Modern Compressible Flow With Historical Perspective.* McGraw Hill, New York, 2003.
5. Ashby, M. F. and S. C. Lim. "Wear-Mechanism Maps," *Scripta Metallurgica et Materialia*, 24(5):805-810, May 1990.
6. *ASM Ready Reference: Thermal Properties of Metals.* ASM International, Materials Park, OH, 2002.
7. Bayer, R. G. *Wear Analysis for Engineers* HNB Publishing, New York, NY, 2002.
8. Benson, T. "Specific Heat Capacity - Calorically Imperfect Gas," *nasa.gov.* Glenn Research Center, 29 July 2008.
9. Bowden, F. P. and D. Tabor. *Friction: An Introduction to Tribology.* Robert E. Krieger Publishing Company, Malabar, FL, 1982.
10. Buentello, R. G. *3D Finite Element Modeling of Sliding Wear AFIT-ENY-DS-13-D-06.* PhD Dissertation, Air Force Institute of Technology, Wright-Patterson AFB, OH, 2013.
11. Cameron, G. J. *An Evaluation of High Velocity Wear AFIT/GAE/ENY/07-M06.* Master's Thesis, Air Force Institute of Technology, Wright-Patterson AFB, OH, 2010.

12. Chauvin, L. T. and C. A. deMoraes. *Correlation of Supersonic Convective Heat-Transfer Coefficients from Measurements of the Skin Temperature of a Parabolic Body of Revolution.* NACA RM-10. 1951.

13. Cinnamon, J. D. *Analysis and Simulation of Hypervelocity Gouging Impacts AFIT/DS/ENY/06-01.* PhD Dissertation, Air Force Institute of Technology, Wright-Patterson AFB, OH, 2006.

14. Cook, R. D., D. S. Malkus, M. E. Plesha, and R. J. Witt. *Concepts and Applications of Finite Element Analysis.* John Wiley & Sons, Inc., 2002.

15. Eggers, A. J. Jr. *One-Dimensional Flows of an Imperfect Diatomic Gas.* NACA Report 959, National Advisory Committee for Aeronautics, 1959.

16. *Dry Air Properties.* engineeringtoolbox.com, data retrieved February 2014.

17. Incropera, F. P. and D. P. DeWitt. *Fundamentals of Heat and Mass Transfer.* John Wiley & Sons, New York, 1996.

18. Hale, C. S. *Consideration of Wear Rates at High Velocity AFIT/DS/ENY/10-08.* PhD Dissertation, Air Force Institute of Technology, Wright-Patterson AFB, OH, 2010.

19. Hall, A. M. and C. J. Slunder. *The Metallurgy, Behavior, and Application of the 18-Percent Nickel Maraging Steels*, NASA SP-5051, 1968.

20. Hu, H. and S. A. Argyropoulos. “Mathematical Modelling of Solidification and Melting: A Review,” *Modelling and Simulation in Material Science and Engineering.* 4(4):311-396, 1996.

21. Kays, W. M. and M. E. Crawford. *Convective Heat and Mass Transfer.* McGraw Hill, New York, 1980.

22. Kirillin, V.A., V.V. Sychev, and A. E. Sheindlin. *Engineering Thermodynamics.* Trans. S. Semyonv. Moscow, 1981.

23. Korkegi, R. H. and R. A. Briggs. *Compressible Turbulent Plane Couette Flow.* Technical Report ARL 670223, Aerospace Research Laboratory, 1967.

24. Korkegi, R. H. and R. A. Briggs. "The Hypersonic Slipper Bearing - A Test Track Problem." *Journal of Spacecraft and Rockets*, 6(2):210-212, February 1969.

25. Laird, D. J. *The Investigation of Hypervelocity Gouging AFIT/DS/ENY/02-01.* PhD Dissertation, Air Force Institute of Technology, Wright-Patterson AFB, OH, 2002.

26. Le, K. J. *A Study of the Thermal Environment Developed by a Traveling Slipper at High Velocity AFIT-ENY-13-M-20.* Master's Thesis, Air Force Institute of Technology, Wright-Patterson AFB, OH, 2013.

27. Lofthouse, A. J. *Computational Aerodynamic Analysis of the Flow Field about a Hypervelocity Test Sled AFIT/GAW/ENY/02-07.* Master's Thesis, Air Force Institute of Technology, Wright-Patterson AFB, OH, 2007.

28. Meador, S. P. *Consideration of Wear at High Velocities AFIT/GAW/ENY/10-M16.* Master's Thesis, Air Force Institute of Technology, Wright-Patterson AFB, OH, 2010.

29. Montgomery, R.S. "Friction and Wear at High Sliding Speeds," *Wear*, 36(3):275-298, March 1976.

30. Paek-Spidell, G. Y. *Analysis of Heat Partitioning During Sliding Contact at High Speed and Pressure AFIT-ENC-DS-14-M-02.* PhD Disseratation, Air Force Institute of Technology, Wright-Patterson AFB, OH, 2014.

31. Potter, M.C. and C. W. Sommerton. *Schaum's Outline of Thermodynamics for Engineers.* McGraw-Hill, New York, NY, 2006.

32. Reddy, J. N. and D. K. Gartling. *The Finite Element Method in Heat Transfer and Fluid Dynamics.* CRC Press, Boca Raton, FL, 2010.

33. Rutledge, J. L. *Pulsed Film Cooling on a Turbine Blade Leading Edge AFIT/DS/ENY/09-S03.* PhD Dissertation, Wright-Patterson AFB, OH, Air Force Institute of Technology, 2009.

34. Schlichting, H. and K. Gersten. *Boundary Layer Theory.* Springer, Berlin, 2000.

35. Welty, J. R., C. E. Wicks, and R. E. Wilson, *Fundamentals of Momentum, Heat, and Mass Transfer.* John Wiley & Sons, New York, 1984.

36. Wolfson, M. R. *Wear, Solid Lubrication, and Bearing Material Investigation for High-Speed Track Applications.* Technical Report AFMDC-TR-60-7, Test Track Division, Missile Development Center, Holloman AFB, New Mexico, 1960.

37. Wuertemberger, L. B. *Predicting the Wear of High Speed Rocket Sleds AFIT-ENY-12-D-02.* Master's Thesis, Air Force Institute of Technology, Wright-Patterson AFB, OH, 2012.

REPORT DOCUMENTATION PAGE

Form Approved
OMB No. 0704-0188

1. REPORT DATE *(DD-MM-YYYY)*
17-03-2014

2. REPORT TYPE
Master's Thesis

3. DATES COVERED *(From - To)*
Aug 2012 - Mar 2014

4. TITLE AND SUBTITLE
Thermal and Melt Wear Characterization of Materials in Sliding Contact at High Speed

5a. CONTRACT NUMBER

5b. GRANT NUMBER

5c. PROGRAM ELEMENT NUMBER

6. AUTHOR(S)
Alban, Christopher J, Capt, USAF

5d. PROJECT NUMBER

5e. TASK NUMBER

5f. WORK UNIT NUMBER

7. PERFORMING ORGANIZATION NAME(S) AND ADDRESS(ES)
Air Force Institute of Technology
Graduate School of Engineering and Management (AFIT/EN)
2950 Hobson Way
Wright-Patterson AFB OH 45433-7765

8. PERFORMING ORGANIZATION REPORT NUMBER
AFIT-ENY-14-M-04

9. SPONSORING/MONITORING AGENCY NAME(S) AND ADDRESS(ES)
Air Force Office of Scientific Research
Dr. Michael Kendra
875 Randolph Street, Suite 325, Room 3112
Arlington, VA 22203
michael.kendra@us.af.mil

10. SPONSOR/MONITOR'S ACRONYM(S)
AFOSR

11. SPONSOR/MONITOR'S REPORT NUMBER(S)

12. DISTRIBUTION/AVAILABILITY STATEMENT
DISTRIBUTION STATEMENT A: APPROVED FOR PUBLIC RELEASE; DISTRIBUTION UNLIMITED.

13. SUPPLEMENTARY NOTES
This material is declared a work of the U.S. Government and is not subject to copyright protection in the United States.

14. ABSTRACT

The Holloman High Speed Test Track is used to evaluate hypersonic aircraft materiel in a near-operational environment. The four-stage pusher rocket sled is capable of accelerating a test apparatus to hypersonic speeds in a matter of seconds. The sled must contend with tremendous thermal, mechanical, and aerodynamic loading during each run. The effects of the combination of forces acting on the sled are most acute at the interface between the rail and the wraparound slipper that holds the sled to the rail. Frictional heating due to sliding contact between the slipper and the rail coupled with mechanical wear can lead to significant material degradation in the slipper. Aerodynamic heating can exacerbate deleterious wear effects. This work considers the application of thermal and aerodynamic loading on the slipper. A two-dimensional finite element model is employed to depict temperature distribution and estimate melt wear over the course of a test run. The thermal load cases considered allow a new perspective on the slipper wear phenomena and should serve as a building block in future research endeavors.

15. SUBJECT TERMS
Heat Transfer, Aerodynamics, Finite Elements, Melt Wear, Holloman High Speed Test Track.

16. SECURITY CLASSIFICATION OF:			17. LIMITATION OF ABSTRACT	18. NUMBER OF PAGES	19a. NAME OF RESPONSIBLE PERSON
a. REPORT	b. ABSTRACT	c. THIS PAGE			Dr. Anthony N. Palazotto, AFIT/ENY
U	U	U	UU	179	19b. TELEPHONE NUMBER *(Include area code)* (937) 255-3636 x4599 anthony.palazotto@afit.edu

Reset